UNIMORE – University of Modena and Reggio Emilia

PhD Program in Physics and Nanosciences

XXXIII Cycle

Growth, morphology, and electronic response of organic field effect transistors in the solid state and in electrolyte

Sofia Drakopoulou

Coordinator

Prof. Stefano Frabboni

Supervisor

Prof. Fabio Biscarini

Co-Supervisor

Prof. Andrea Alessandrini

Academic Year: 2021

Supervisor: Prof. Fabio Biscarini,

Life sciences Department

University of Modena and Reggio Emilia,

Via Campi 103, 41125 Modena (Italy)

Tel. +390592058587

e-mail: fabio.biscarini@unimore.it

Co-Supervisor: Prof. Andrea Alessandrini

Department of Physics, Informatics and Mathematics,

University of Modena and Reggio Emilia,

Via Campi 213/A, 41125 Modena, Italy

Tel: +390592055297

mail: andrea.alessandrini@unimore.it

Abstract:

Organic electronic devices, such as light emitting diodes (OLEDs), field effect transistors (OFETs) and solar cells (OPVs) have reached a technological maturity and, in the case of OLEDs and OPVs, industrial production. Significant advancements in chemical synthesis, materials processing, and device engineering have boosted the device performance and reliability. However, several concepts regarding the mechanism of the device operations are still unresolved, especially in OFETs. Charge transport in the organic semiconductors involves different interfaces of the materials and one of the most important questions that people try to address is how the morphology of the device affects the mechanism of charge transport across the device. Indeed, morphology, molecular and energy disorder, and surface defects can easily influence their performance. There is a compelling quest for understanding the mechanical aspects of the organic thin film nucleation and growth on real test patterns in order to understand the morphology.

The main goal of this thesis was to understand the correlation between different growth modes, morphology, and the electrical response of OFETs in solid state operation as well as in an electrolytic environment. Pentacene is the workhorse organic semiconductor that we used throughout this thesis. The motivation is understanding the physics of the pentacene transistors as a function of the semiconductor channel thickness, and it was the core of the EC-Marie Curie project SPM 2.0 that supported my research work.

As a new important finding out of this thesis, we discovered and assessed a new anomalous growth of Pentacene thin films vs increase of the thickness, viz. the mass of organic semiconductor in the OFET channel. In this novel growth mode, there is a breakdown to the usually observed growth mode upon rapid roughening, where a layer-by-layer growth at the early stages suddenly evolves into a self-affine mode characterized by growing islands made of terrace stacks. We observed this mode at the lower deposition temperatures, but we discovered that at a precise range of deposition temperature and rate, viz. 80°C and 0.1 A/s, this growth mode is not observed, instead an iteration of wetting/dewetting transition occurs as thickness increases. Its peculiar features consist of the fact that the morphology of the islands as stacks of monomolecular terraces, is retained. However, the morphological parameters, such as correlation lengths and roughness, that we extract from

atomic force microscopy (AFM) images exhibit anomalous oscillations with period increasing with thickness. In order to explain the trend of the parameters, we devised an empirical equation that encompasses both self-affine 3D growth and the oscillations typical of wetting/dewetting transition as in the spinodal dewetting phenomena. We then analyzed the electrical characteristics of the OFET operated as solid-state device as well as electrolyte gated devices. The correlation of the transistor parameters with the morphology were analyzed. Experiments using bimodal AFM allowed us to investigate the mechanical properties of conductive and semiconductive thin films. The latter activity was carried out at CSIC-ICMM in Madrid during the secondment at the laboratory of Professor Ricardo Garcia.

Prefazione:

I dispositivi elettronici organici, come i diodi a emissione di luminosa (OLED), i transistor ad effetto di campo (OFET) e le celle solari (OPV) hanno raggiunto una maturità tecnologica e, nel caso di OLED e OPV, anche la produzione industriale. I progressi significativi nella sintesi chimica, nella lavorazione dei materiali e nell'ingegneria dei dispositivi ne hanno migliorato le prestazioni e l'affidabilità. Tuttavia, diverse domande riguardanti il meccanismo di funzionamento dei dispositivi sono ancora irrisolte, specialmente negli OFET. Il trasporto di carica nei semiconduttori organici coinvolge diverse interfacce dei materiali e una delle domande principali che i ricercatori stanno cercando di risolvere, è come la morfologia del dispositivo influenzi il meccanismo di trasporto della carica attraverso il dispositivo. Infatti, la morfologia, il disordine molecolare, energetico e i difetti superficiali possono facilmente influenzare le prestazioni dei semiconduttori. C'è una ricerca impellente atta alla comprensione degli aspetti meccanici della nucleazione e della crescita dei film sottili organici su test pattern reali nell'ottica di comprenderne la morfologia.

L'obiettivo principale di questo lavoro è stata la comprensione della correlazione tra i diversi modi di crescita, la morfologia e la risposta elettrica degli OFET in stato solido e in un ambiente elettrolitico. Per questa tesi abbiamo utilizzato come semiconduttore organico il pentacene. La motivazione di questa scelta ricade nella volontà di comprendere la fisica dei transistor a base di pentacene, in funzione dello spessore del canale del semiconduttore. Quest'ultimo, infatti, è stato il nucleo del progetto Marie Curie Sklodowska SPM 2.0, che ha supportato il mio lavoro di ricerca. Il risultato principale di questa tesi è stato aver individuato caratterizzato una nuova crescita anomala dei film sottili di pentacene rispetto all'aumento dello spessore, vale a dire, la massa nel canale del semiconduttore organico. In questa nuova modalità di crescita, vi è una variazione rispetto alla modalità di crescita solitamente osservata in caso di rapido incremento della rugosità, in cui una crescita strato su strato nelle fasi iniziali, si evolve improvvisamente in un modo auto affine caratterizzato da isole in crescita costituite da blocchi a terrazze. Abbiamo osservato questa crescita a temperature di deposizione più basse, ma abbiamo scoperto che in un intervallo preciso di temperatura e velocità di deposizione, vale a dire, 80 ° C e 0,1 A / s, questo modo di crescita

non avviene. Abbiamo infatti osservato che invece si verifica un’iterazione della transizione di wetting/dewetting all'aumentare dello spessore. Le sue caratteristiche peculiari consistono nel fatto che la morfologia delle isole come terrazze monomolecolari, viene mantenuta. Tuttavia, i parametri morfologici, come le lunghezze di correlazione e la rugosità, che estraiamo dalle immagini della microscopia a forza atomica (AFM), mostrano oscillazioni anomale con periodo che aumenta con lo spessore. Per spiegare l'andamento dei parametri, abbiamo ideato un'equazione empirica, che comprende sia la crescita 3D auto affine sia le oscillazioni tipiche della transizione di wetting/dewetting, come nei fenomeni dello spinodal dewetting. Abbiamo quindi analizzato le caratteristiche elettriche dell'OFET operante allo stato solido e in ambiente elettrolitico. È stata quindi analizzata la correlazione dei parametri del transistor con la morfologia. Gli esperimenti che sono stati condotti utilizzando la AFM bimodale, ci hanno permesso di studiare le proprietà meccaniche di film sottili di conduttori e semiconduttori. Quest'ultima attività è stata svolta presso il CSIC-ICMM di Madrid durante il mio periodo di studio presso il laboratorio del Prof. Ricardo Garcia.

Keywords

Organic Field-Effect transistor

Scanning Probe Microscopies

Organic Bioelectronics

Organic electronics

Thin film growth

Morphology

Ἰθάκη

“Σὰ βγεῖς στὸν πηγαιμὸ γιὰ τὴν Ἰθάκη,

νὰ εὔχεσαι νἆναι μακρὺς ὁ δρόμος,

γεμάτος περιπέτειες,

γεμάτος γνώσεις.”

Κωνσταντίνος Καβάφης

Contents

Chapter 1

Organic thin films and their applications in organic electronics

"*This chapter is an introduction to organic electronics. The basic concepts of organic semiconductors, the mechanism of charge transport, as well as their thin film applications in Field Effect Transistors operating both in solid state and in electrolyte are presented. Moreover, the technology and the mechanisms of nucleation and growth of organic thin films are introduced and overviewed from literature.*"

1.1 Organic electronics

In the past three decades, organic electronics has moved from basic research to consumer's applications on the market with an impact in our daily life. The first report on electronic properties was the demonstration in 1986 of the first organic field-effect transistor (OFET) [1]. At the same time, the first organic light emitting diode (OLEDs) [2] was demonstrated. These breakthroughs were enabled by the use of vacuum-sublimed thin films of molecular semiconductors in place of bulk molecular crystals, which were extensively studied for setting the physical-chemical grounds of charge and excitation transport in organic solid state but were not technologically viable. A few years later the demonstration of polymer light emitting diodes (PLEDs) and the design and synthesis of soluble organic semiconductors opened the avenue to printable (opto) electronic devices. [3,4] This was a leap from the extensively studied (doped) conductive polymers, like polyacetylene (that lead to the Nobel prize in Chemistry in year 2000 to Heeger, Mc Diarmid and Shirakawa [5]) that was however of no technological impact being completely insoluble and hardly processable, to libraries of materials designed for processing, printing as well as for tuning the relevant properties in LEDs or photovoltaic cells or transistors.

Organic electronics devices exhibit performance comparable to that of amorphous silicon electronics, which makes it attractive for many low power-low cost consumer's electronics applications. Among the advantages, organic electronics exploits a variety of organic materials that can be deposited as thin films on a wide range of substrates, planar and curved, rigid or flexible, and patterned by using scalable non-conventional processing techniques, such as inkjet printing and roll-to-roll manufacturing [6–8]. These technologies use low energy and resources, being based on additive manufacturing, conversely to top-down approaches of silicon technology. The fabrication technology being high-throughput or continuous enables a large number of applications, including flat panel displays [9], organic LEDs [10], photovoltaic cells [3], large-area electronics [11] and sensors [12] .

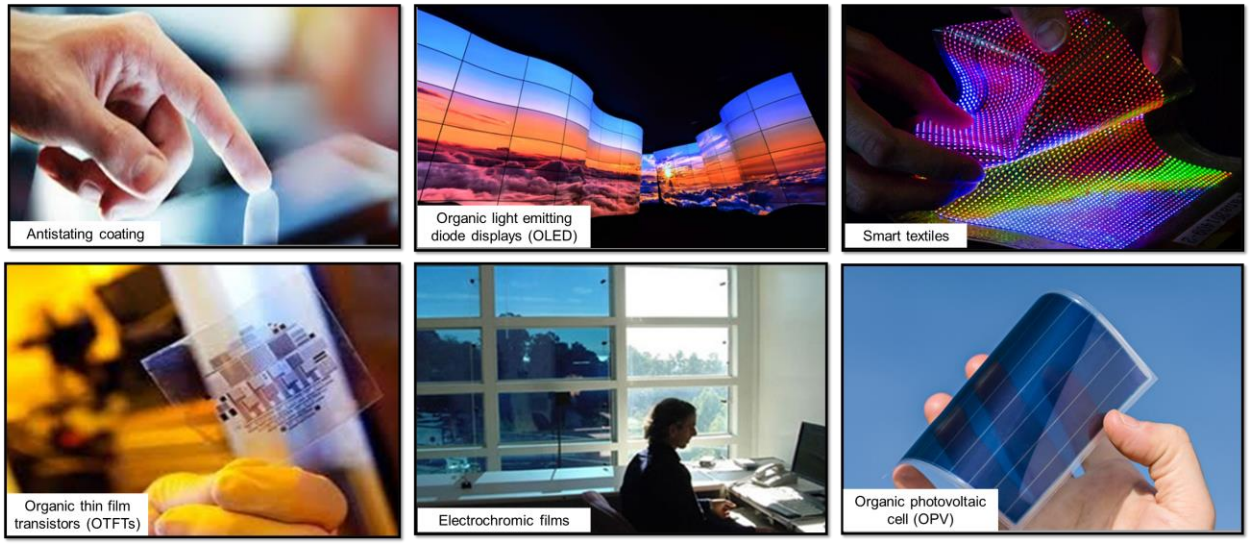

FIG. 1.1. Applications of organic electronics

A strong effort in materials design aimed to optimize the performance of organic electronics devices has been going on for the last couple of decades. This led to the advent of OLED displays, albeit a whole organic active matrix AM-OLED display is hampered by the still low stability of organic transistors (the active matrix components) and the sensitivity of the devices to air, moisture, and light exposure.

Charge transport is one of the universal aspects of the physics of the organic devices. It occurs across different interfaces of the materials constituting the device architecture. Here, we address one of the most important questions: how the morphology of the semiconductor thin film affects the mechanism of charge transport across the device, and hence the device response.

1.2 Organic bioelectronics

The emerging field of organic bioelectronics bridges organic electronics with the world of the living matter. Standard organic electronics devices show instability in water. The evolution of fabrication technologies to flexible substrates led to the production of devices that conformally

adhere to the shape of human body or to an organ upon implantation [13], else by integration on textiles [14] or upon contact with the skin [15].

For the detection of biomolecules or of biological events, sensors need to be operated in an aqueous environment. In 2010 the first demonstration of an organic transistor operated in water was attained [16]. The integration of moieties for specific molecular recognition led to the development of *label-free* biosensors [17] and transducers in signals in-vitro [18,19] and in -vivo [20,21]. A lot of applications of bioelectronics such as electronic skin, pressure sensors [22] as well as in-vivo implants for monitoring the central nervous system [23] were demonstrated. Fig. 1.2 shows some of the pioneer applications of bioelectronics.

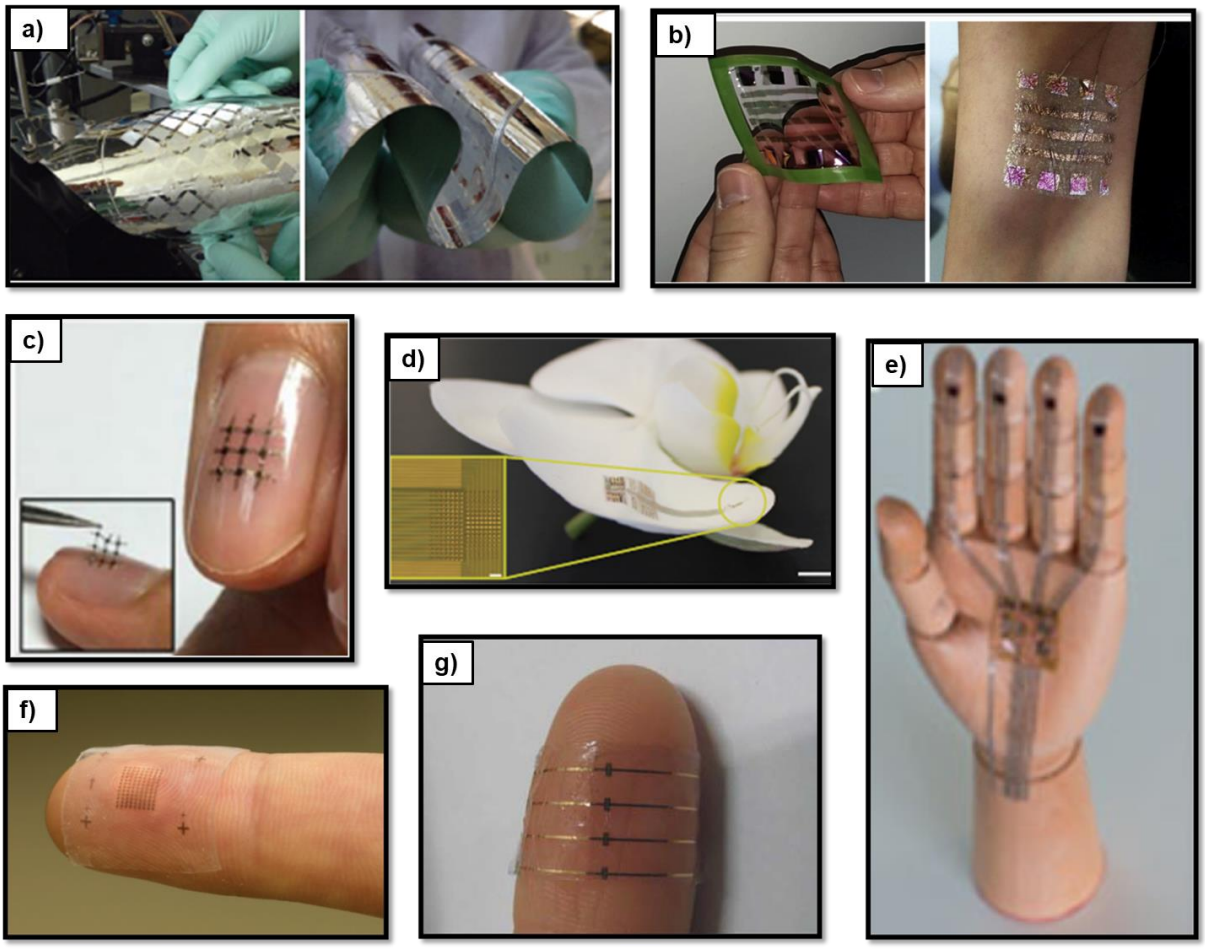

FIG. 1.2. Application of organic bioelectronics. a) Highly sensitive flexible pressure sensors b) Ultra-conformable organic field-Effect Transistors and circuits for epidermal electronic applications c) Organic devices on a highly flexible stretchable, and patchable freestanding substrate d) Organic electrochemical transistor (OECT) for recording electrophysiological signals on the surface of the brain e) A skin-inspired organic digital mechanoreceptor f) Intrinsically stretchable transistor array as a core platform for functional skin electronics g) Electrocorticography recording with a bioresorbable OECT. [22–27]

1.3 Organic semiconductors

Electrical conduction in organic materials was reported for the first time in the 1950's and early 1960's, when photoconductivity and electroluminescence were detected in organic crystals of pi-conjugated oligoacenes like naphthalene and anthracene [28–30]. Although crystals showed high charge carrier mobility, their processability and the high voltages required limited real applications. In the 1960's molecularly doped polymers consisting of small organic pigments dispersed in an insulating polymer matrix were developed for xerographic applications [31]. Conjugated materials exhibit alternating single (σ-bond) and double bonds (one σ- and π-bonds) between carbon atoms, or between carbon and heteroatoms like N, O, S, Se (to name a few suitable elements). The σ-bond is generated from the linear combination of atomic orbitals with axial symmetry, e.g., s-, p-, d-orbitals, or their hybrid orbitals, and is localized between two neighbor atoms. A σ-bond requires that bonding σ-orbitals be populated and antibonding σ*-orbitals are not. The π-orbitals result from the lateral superposition of p_z orbitals of neighboring carbon atoms or heteroatoms (Fig. 1.3a). In Fig. 1.3b the energy levels of the simplest π-system (two-atom) are shown. The lower energy **π**-orbital is bonding and is populated by two electrons. The higher energy **π**-orbital is anti-bonding and is empty. Because the number of electrons in **π**-bonding orbitals exceeds that in **π***-antibonding orbitals, a **π**-bond is formed. For an increasing number of C-atoms, the number of **π**-orbitals increases accordingly, with only half-of them (bonding orbitals) filled. We term Highest Occupied Molecular Orbitals - HOMOs the populated **π**-orbitals closer to the Fermi level, and Lowest Unoccupied Molecular Orbitals - LUMOs the empty **π**-orbitals closer

to the Fermi level. The Fermi level lies in between HOMO and LUMO. The gap becomes smaller with the increasing number of C-atoms.

The alternance of single and double bonds yields delocalization of the **π**-orbitals across the whole molecular length, thus creating an electron density above and below the nodal plane. A prototype example is polyacetylene, which consists of a single chain of alternating single- and double-bonds (Fig. 3c). For a large number of C-atoms in the chain, Hückel theory predicts that the π-orbitals are dispersed across a band whose width is proportional to the matrix element of the Hamiltonian (also termed *overlap*). Considering a chain of C atoms with one p_z orbital each (as basis set), the overlap is the interaction between adjacent p-orbitals. Hence, the larger the overlap is, the larger the energy dispersion of the molecular orbitals will be. Therefore, when the number of C atoms is large, a density of states (DOS) spreads in a π-band around the Fermi level, is created (Fig. 1.3d). The π-band is half-filled with electrons, which implies that only the lower energy half-band (valence band) is fully populated, while the high-energy half band (conduction band) is empty. Introducing electron correlation and phonon electron coupling in the Hamiltonian yields a band gap separating the half-bands as in a semiconductor (Fig. 1.3c), which leads to the term organic semiconductors. The band gap is determined from either optical, optoelectronic, or electronic spectroscopies, and spans the range of 1–4 eV, which comprises the whole range from infrared to ultraviolet region. We refer to the valence and conduction bands as HOMO- LUMO- bands, respectively. Fermi level lies in the gap.

In ideal chain molecules the delocalization lengthscale would span the whole length of the chain. However, in real life topological (e.g., cis-trans transitions, conformational defects) and chemical defects (also due to parasitic dopants), limit the actual delocalization lengthscales. It is estimated that in chain semiconductors delocalizations span no more than several monomeric units (in the range 6-10 units equivalent to a conjugation length scale of a few nm). This inherent limitation of macromolecular chains makes then conjugated molecules with precisely defined size and structure, and above all chemical composition, attractive because their π-electrons are delocalized across comparable lengthscales (defined by the molecular size). Hence, two “schools of thought” in organic semiconductor materials emerged during the years, one based on polymers/macromolecules, and the other on “small molecules”.

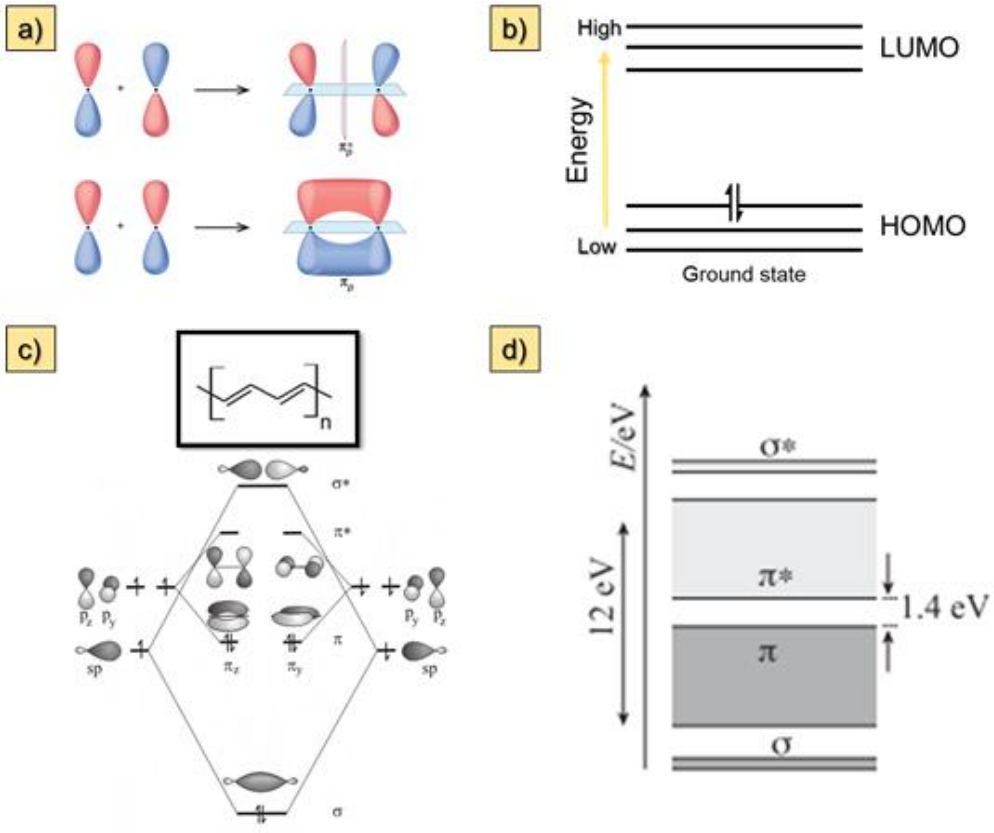

FIG. 1.3. a) Side-by-side overlap of each two p orbitals results in the formation of two π molecular orbitals. Combining the out-of-phase orbitals results in an antibonding molecular orbital and combining the in-phase orbitals results in a bonding orbital; b) energy levels of a simple π-system; c) Simple energy level diagram of acetylene; d) Band structure of polyacetylene, showing the σ e σ∗ bands, which result from the combination of the sp^2 hybrids, and the π and π∗ resulting from the combination of the p_z of each carbon atom.

To understand the difference, it is useful to make the analogy with the band structure described above. In the case of molecular semiconductors, each molecule exhibits a discrete π-system consisting of a number of π-orbitals equal to the number of conjugated atoms. Once the molecules are packed in the solid state, either in a crystal or in a thin film, the intermolecular (non-covalent) interaction between them yields a broadening of each energy level. The stronger is the non-

covalent interaction (quadrupole and van der Waals pi-stacking interactions are dominant intermolecular interactions in these systems), the broader the spread of each level will be. Because the strength of non-covalent interactions is typically of the order of 0.1 eV, in molecular semiconductors the bandwidth is narrower than in chain macromolecules. It turns out that the HOMO-band (derived from HOMO orbitals) and the LUMO-band (derived from LUMO orbitals) are narrow, their band gap being smaller than the HOMO-LUMO gap of the molecule. This is illustrated in the series of oligoacenes depicted in Fig. 1.4. The optical band gaps as well as the HOMO and LUMO levels are reported. The advantage is, however, that a precise chemical design, also supported by computations and modelling of the interactions, allows one to finely tune the relevant properties as band gap and bandwidth.

Narrow bandwidth implies also that the delocalization of the π-electrons, which are fully or largely delocalized across each single molecule, is instead limited typically to a few neighboring molecules across the material. Here, structural packing defects and the control of molecular architecture at length scales ranging from a few molecules to microns become important in establishing the actual intermolecular delocalization. This aspect, that motivates largely this thesis, will be deepened in a next section. The “quasi-localization” of electrons on molecular scales has an important consequence on the mechanism of charge and excitation transport, and on the nature of the charge or energy carriers that become large both in size and effective mass.

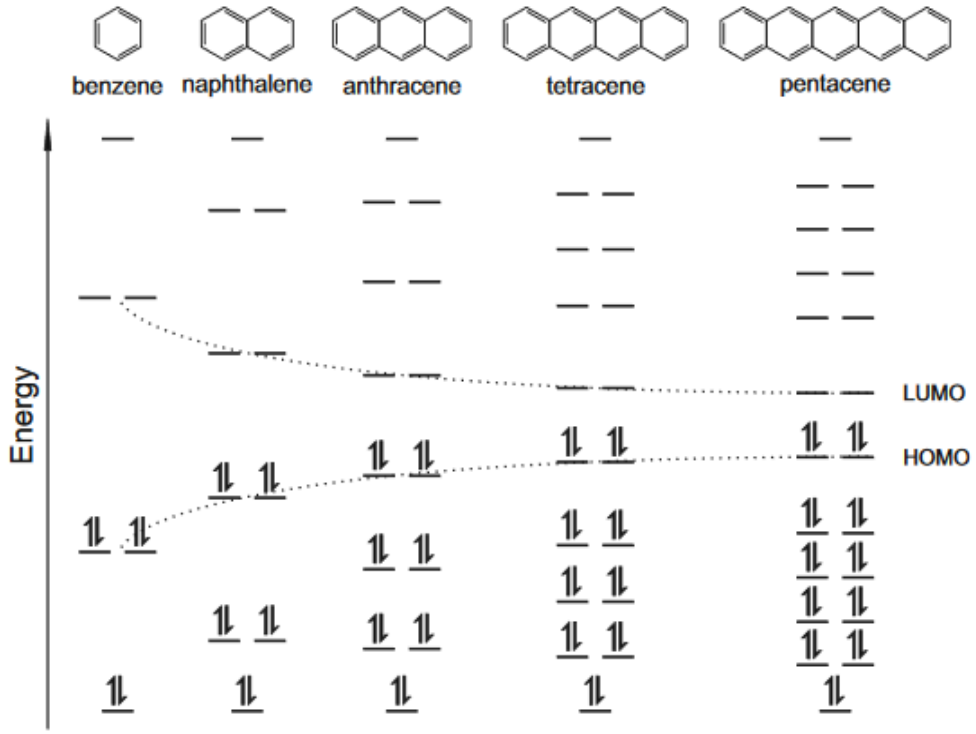

FIG. 1.4. Energy diagrams of the acene family (benzene, naphthalene, anthracene, tetracene, and pentacene) [32]

Organic semiconductors, either molecules or polymers, become either positively or negatively charged upon removing/adding an electron from the HOMO or to the LUMO band. This process is termed doping and can be achieved in two ways: i) a chemical reaction that oxidizes/reduces the semiconductor (e.g., using halogens or metals of groups I-III), else ii) capacitive coupling through a dielectric thin film that upon bias between the channel (acting as one of the plates of the capacitor) and an electrode. Doped organic semiconductors become (more) conductive, even by several orders of magnitude, reaching conductivities in the order of 1000 S/cm. We are mostly interested in electrostatic doping which is indeed at the active layer of the organic field effect transistor. The former process is largely used in production of organic conductive thin film (as the channel is open at low voltages due to doping). The stability of the charged semiconductor enables the longer lifetime of the charged state. Hence, the charge settles on a localized state (e.g., a molecule) and then can move to across the channel. We classify the organic semiconductors as p-

type if the transported charge carriers are holes, else n-type if they are electrons. Organic semiconductors are in principle ambipolar charge carriers, but the majority carrier depends not only on the HOMO and LUMO energy levels (stable n-type semiconductors in ambient require LUMO located more than 4 eV below the vacuum level to avoid charge transfer/oxidation to oxygen and water [33]), but also on the device architecture and the energy level alignment at the interface with the injection/extraction contacts.

1.4 Organic Field Effect Transistors

The field-effect transistor (FET) was envisioned by Lilienfeld already in 1930 [34] a and later demonstrated and studied by Shockley and Pearson in 1948 [35,36], but the applications started only in the ‘60s [37]. The most popular FET is the metal-oxide-semiconductor FET (MOSFET), also known as the metal-insulator-semiconductor FET, in which the gate electrode is electrically insulated from the conducting channel by an oxide layer. The basic idea of a field effect transistor is to modulate the current that flows between two ohmic contacts, termed source and drain, upon application of a voltage to a third contact, termed the gate electrode. Charge carriers can be accumulated or depleted in the semiconductor close to the semiconductor/insulator interface. In fact, this device can be considered as a capacitor, where one plate is the conductive channel in the semiconducting layer and the other is the gate electrode. In the Shockley-Bardeen-Brattain first transistor the semiconductor channel was made on a germanium crystal (Fig. 1.5).

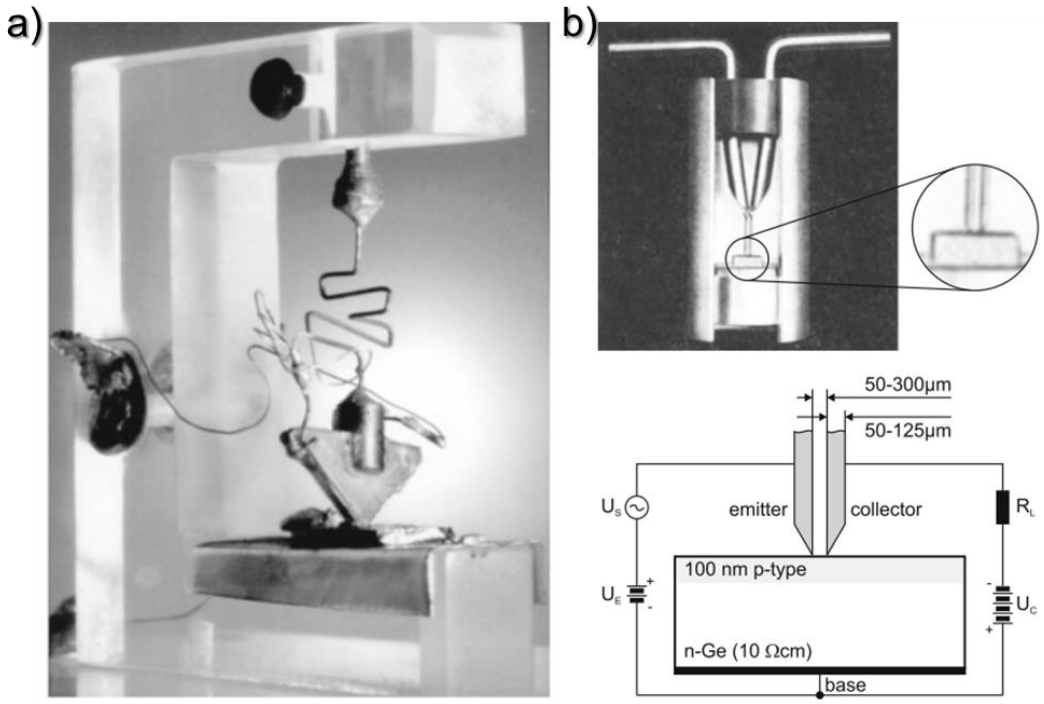

FIG. 1.5. (a) The first transistor, 1947 (length of side of wedge: 32mm). (b) Cutaway model of a 1948-point contact transistor based on n-type bulk Ge and common base circuit diagram. The surface region of the Ge is p-type due to surface states and represents an inversion layer. The two wires are made from phosphor bronze. Adapted from [36]

The organic field effect transistor (OFET) is the central device of this thesis. In OFETs, the channel where charge carriers are generated and transported is made of an organic semiconductor thin film. The contacts and the dielectric layer that couples gate and channel might be organic, inorganic, or hybrid. Materials used for electrodes include metals like Au (with Ti or Cr adhesive primer), Ag, Ni, Pt, Ca, perovskites ($LaSrMnO_3$), conductive polymers like PEDOT:PSS; for dielectric layers SiO_2 is the most common, but also Al_2O_3, high-k dielectrics, polyolefins, perfluorinated polymers, etc. [38–41] Source and drain Au electrodes are in contact with the organic semiconductor film at a distance one from the other equal to the channel length L and W the channel width (Fig.1.6). The gate is separated from the semiconductor film by the insulating layer made of a dielectric SiO_2 thin film. In our test patterns similar to the one depicted in Fig. 1.6 the gate consists of n-type doped-

Si. The lateral extension of S and D is termed the channel width W. Source and drain are isolated from the gate through the dielectric, thus forming a metal-insulator-semiconductor (MIS) junction.

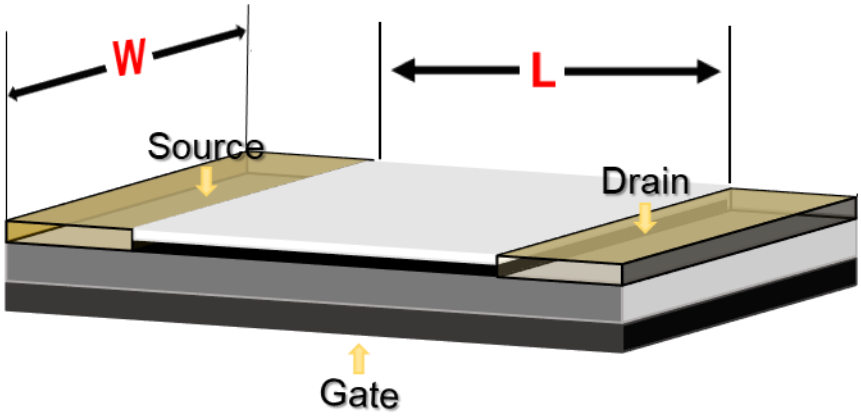

FIG. 1.6 schematic view of a bottom gate/bottom electrodes transistor.

1.4.1 Device configurations

The position of the three electrodes with respect to the semiconductive material defines the different architectures of the organic transistors such as bottom gate/bottom electrodes (Fig. 1.7a) and top gate/bottom electrodes (Fig. 1.7b) which were the architecture used in this thesis; other architectures like bottom gate/top electrodes or top gate/top electrodes have not been used during my thesis work. Bottom electrodes as in Fig 1.7a and 1.7b are the most used architecture since test patterns by photolithography on wafers can be made at home or commercially purchased. Bottom gate/bottom electrodes Fig.1.7a is the most widely adopted architecture, albeit several processing problems due to shadowing induced by topographic relieves of the test pattern on the organic semiconductor channel may affect charge injection.

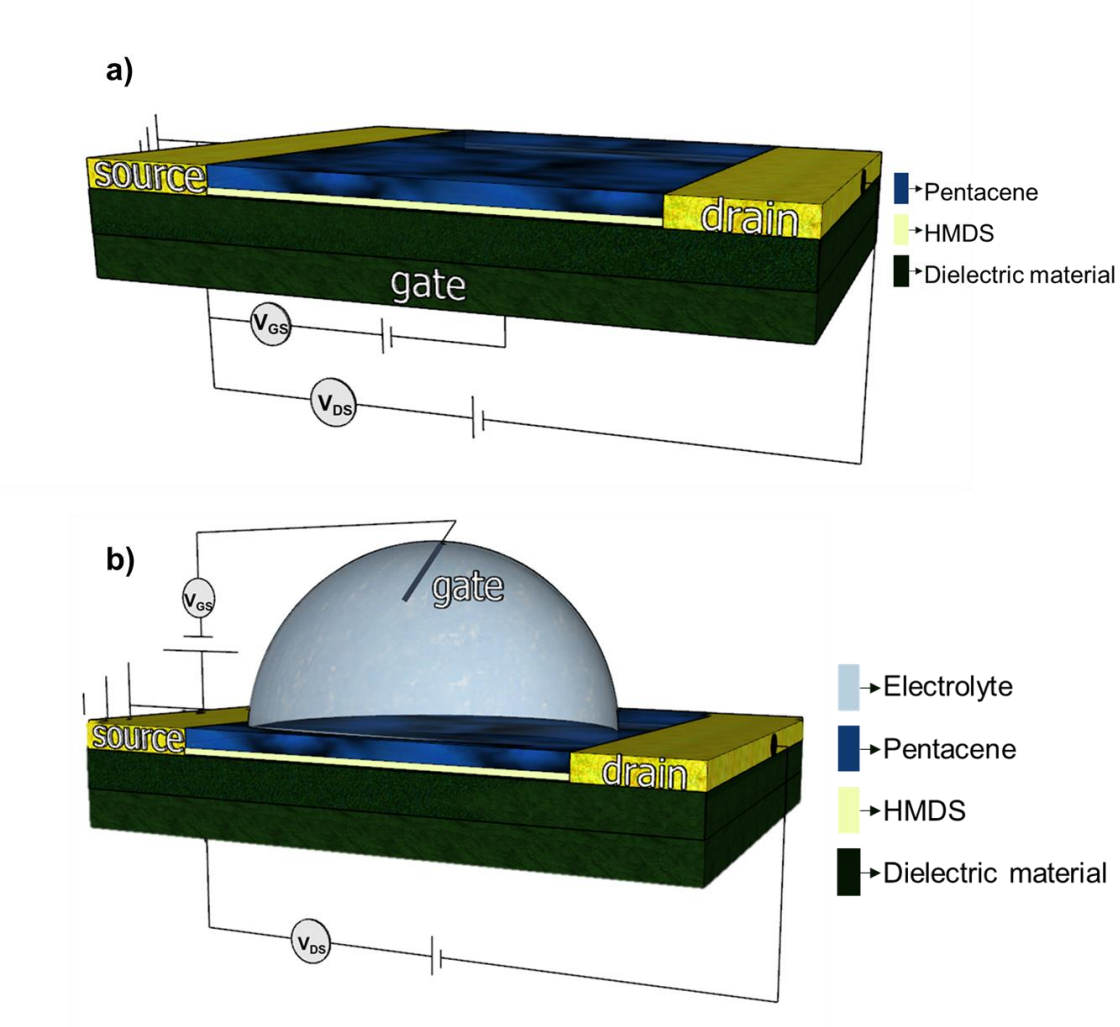

FIG. 1.7 Architectures of organic thin film transistors a) bottom gate/bottom electrodes b) top gate/bottom electrodes.

In organic bioelectronics, the most common architecture for electrolyte gated transistor (EGOT often called EGOFET) can be assimilated to top (electrolyte) gate/bottom electrodes, sometimes also operated as a dual gate transistor with top electrolyte gate and bottom solid state. A typical EGOT architecture is shown in Fig. 1.7. The EGOT operates with no thin film dielectric film, because the electrical double layer forming at the semiconductor-electrolyte interface effectively acts as a capacitor. The gate controls the potential of the electrolyte, and consequently the potential drop across the electrolyte. The electrolyte is typically a buffer solution, else a biological fluid, but can also be a synthetic or natural hydrogel [42,43]. Since the electrical double layer is very thin

(0.1-1 nm depending on the ionic strength) and the dielectric constant of aqueous electrolytes is high (pure water $\boldsymbol{\varepsilon}$ = 79, for an electrolyte even higher [44,45]), the interfacial capacitance per unit area is orders of magnitude larger than the one of dielectric layers (on the order of tens of nF/cm^2). This implies that the EGOT is operated at much lower gate voltages with respect to the solid state OFET, although water-hole interactions may lower the polaron mobility or trap polarons (greater effective mass).

1.4.2 Basic operations

A transistor works as an amplifier in which small potential differences are applied between gate and source electrodes and gate and source electrodes while source electrode is normally grounded. The potential difference between the source and the gate is the gate voltage V_{GS} while the potential difference between the source and drain is referred to as source-drain voltage V_{DS}. We illustrate here the operations of a unipolar transistor. The source injects charges in the channel: these are electrons when a positive gate is applied, while they are holes when a negative gate is applied. [5] In Fig. 1.8 cross sections of the operation regimes of an OFET are illustrated: a negative gate voltage is applied; it induces accumulation of positive charge carriers (holes) at the semiconductor/dielectric interface. For n-type material, it would be a positive gate voltage inducing the accumulation of electrons. The number of charges accumulated is proportional to the gate voltage applied and as well to the capacitance of the dielectric. However not all these charges are mobile and contribute to the source-drain current of the FET. Initially, deep traps have to be filled before the additional charges become mobile for charge transport. Therefore, the concept of threshold voltage V_{th} comes in as the minimum gate voltage required for the formation a conducting channel, as V_{th} has to be overcome in order to accumulate mobile carriers. Therefore, the effective gate voltage is (V_{GS}-V_{th}). When no drain voltage is applied the charge carrier concentration in the channel of the semiconductor is homogeneous across for $|V_{GS}-V_{th}|>0$ V. When a small potential V_{DS} is applied such that $|V_{DS}|<<|V_{GS}-V_{th}|$, a constant longitudinal electric field displaces the charge carriers across the channel. This is termed the *linear regime* because the current increases with increasing $|V_{DS}|$ as in an ohmic junction (depleted of charge carriers at the

channel/drain interface) and even for further increasing $|V_{DS}|$ carrier velocity remains constant as the pinch off which is the V_{DS} at which there is no longer potential difference between the gate electrode and the part of the channel the drain electrode, moves towards the source thus making the current to saturate to a plateau (maximum current). This mode of operation of the OFET where $|V_{DS}|>|V_{GS}-V_{th}|$ is termed *saturation regime.*

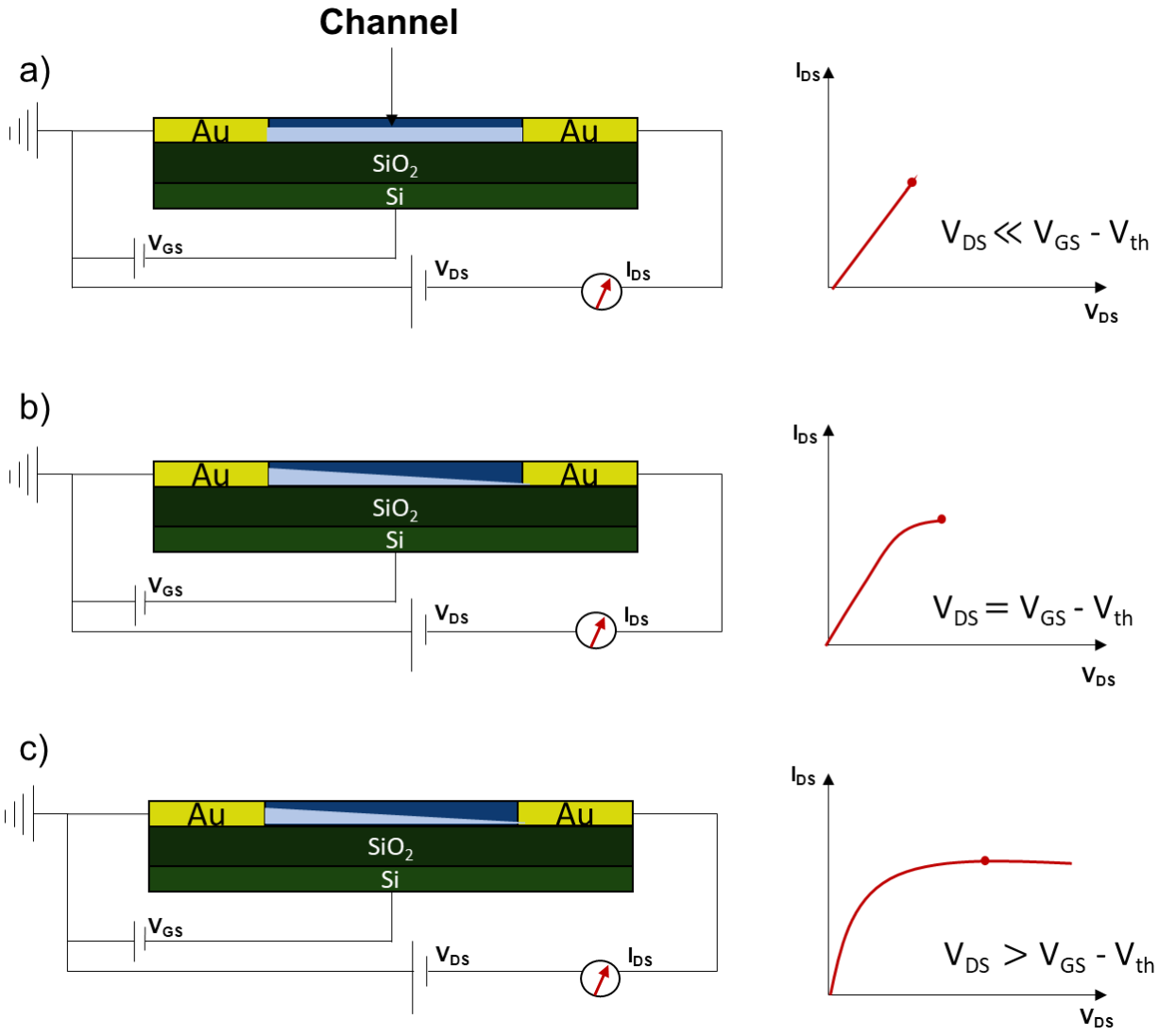

FIG. 1.8 Cross section of operating regimes of an OFET: ***a)*** *linear regime,* ***b)*** *at the pinch off and* ***c)*** *saturation regime.*

1.5 Charge transport in organic semiconductors

A large variety of organic semiconductors of both kinds, small molecules and polymers it possible to be designed due to the presence of π-conjugated electron. In the semiconductor channel, the charge carriers are generated upon application of a gate bias, thus accumulated in charged states (polarons) in the organic semiconductor thanks to the transversal electric field penetrating the channel at the dielectric/semiconductor interface. As we introduced in Section 1.2, large polarizable π-systems yield quadrupole and Van der Waals interactions [46] which, despite of the fact that are larger than thermal energy thus making the solid state aggregate stable, are weaker than the covalent bonds in inorganic semiconductors like Si. This effective perturbation causes modest delocalization of the electron wave function. Thus, the charged polaron remains effectively localized within a molecule in a Wannier state but can be transferred from molecule to molecule because of the weak interaction between Wannier states. In the absence of a longitudinal bias, the motion of the charge carrier is symmetrical in any direction allowed (Brownian motion) around the position where the charge carrier sits at time t=0 s. Thus, the carriers explore the semiconductor space around their positions but do not carry a net current. When a driving force is turned on, the charge carriers can be accelerated and moved along the direction of the longitudinal electric field. In terms of charge mobility, values ranging from one to tens cm^2/Vs were measured in highly pure molecular crystals, and the lower end of these range were attained in thin film OFETs with molecular materials like pentacene, rubrene, 2,7-dioctyl[1]benzothieno[3,2-*b*][1]benzothiophene (C8-BTBT-C8) [16,47,48]. In contrast, in inorganic crystalline semiconductors the charge carriers move in highly delocalized orbitals (Bloch states) forming wide energy bands. Charge carrier mobility is high and is decreased by temperature-dependent lattice vibrations that scatter the carriers.

In the case of organic thin films, the amount of structural and energy disorder is greater than in single crystals. High-vacuum sublimed oligomers often give rise to polycrystalline films, while solution processed polymers often yield highly disordered or amorphous film. As a consequence, thin films normally exhibit lower performance with respect to single crystals devices. The charge mobility depends strongly on the chemical purity, as well as on the multiscale organization that results into morphology. It turns out that the effect of temperature in organic thin films is more

complex, as the temperature is detrimental to highly ordered crystals as it destroys band transport, but it could instead enhance charge transport in disordered films. Hence, conjugated materials display a wide range of charge carrier mobility with a temperature dependence that is not monotonically decreasing [49,50].

Band Transport

Band transport refers to the mechanism occurring in crystalline solids, generally metal and semiconductors. This transport is associated with energy bands originated by interacting atoms bound together. The population of a state whose energy level E is given by the Fermi-Dirac equation (eq.1):

$$f(E) = \frac{1}{1+exp\frac{E-E_F}{kT}} \quad (1)$$

where k is the Boltzmann constant, T is the absolute temperature and E_F the Fermi energy. We distinguish two cases: i) the valence band (highest occupied band) is filled, while the conduction band (the lowest occupied band) is completely empty. The two bands are separated by an energy gap, the larger it is the more localized the orbitals are. Large gaps are typical of insulators. In metals there is no gap, and the continuous band is half filled and half empty. Semiconductors bands are similar to insulators but the energy gap between the top of the valence band and the bottom of the conduction band can be overcome by electrons at finite temperature. This causes the smoothing of the Fermi Dirac distribution near the Fermi level, with populated states at the top of the valence band that are emptied and an equivalent number of filled states at the bottom of the conduction band.

The charge transport in delocalized bands can easily be described with the Drude model, upon the assumption that the carriers are free to move under the influence of an applied electric field (free electron gas). Dissipation forces due to the collisions lead to a steady state mean velocity. A

statistical equation describes the drift velocity v_x of the carriers in the direction of the electric field F_x as shown in eq. 2

$$\langle v_x \rangle = \frac{q\tau}{m^*} F_x = \mu F_x \tag{2}$$

where q is the element charge, m^* is the effective mass, τ is the relaxation time and μ is the mobility. The mean free path λ which is the mean distance between two collisions has to be much larger than the de Broglie wavelength of the charge carrier in order for this model to be valid. The mean path is given as

$$\lambda = v_{th}\tau \tag{3}$$

where $v_{th} = \sqrt{\frac{3kT}{m^*}}$ is the electron thermal velocity. The mobility can also be described from a combination of eq. 2 and eq. 3 as

$$\mu = \frac{q\lambda}{m^* v_{th}} \tag{4}$$

The temperature dependence of mobility relies on the nature of scattering centers, and it is found following an inverse power-law vs T with exponent n>0:

$$\mu(T) \propto T^{-n} \tag{5}$$

where *n* is positive number, and so from eq. 5 is shown that the mobility increases with the decrease of the temperature.

Polarons

The charge carriers in organic semiconductors are quasi-particles termed polarons. Their motion cannot be assimilated to band transport because the polarization which accompanies the charge carrier during its motion makes this motion incoherent (compared to transport along Bloch states which retains the crystal coherence). Indeed, a charge carrier located at a molecular site polarizes its surrounding region by coupling the electric field of the charge with the electric dipoles induced in the neighbor molecules. This electrostatic coupling lowers the energy of the polaron and makes the energy difference between the polaron state and the neutral state lesser than in the absence of polarization. The time that the charge sits on the molecule as well as the time that the charge needs to be polarized are termed as τ_{res} and τ_{el}, respectively. As a result, the charge starts traveling as a carrier dressed in the polarization cloud. In Fig. 1.9 is shown the polaron formation in a conjugated organic solid. The polarization affects a volume substantially larger than the molecule, thus making the effective mass larger because the transport of the charge carrier from one site to another must be accompanied by undressing and re-dressing the polaron. According to eq. 4, charge carrier mobility of an organic material is strongly dependent on the local coupling, but also on the electronic and phononic bandwidth and phonon energy.

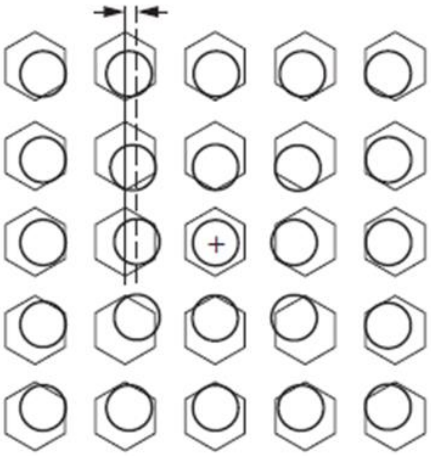

FIG. 1.9 shows a schematic representation of the polaron formation when a positive charge is placed on a molecule in a conjugated organic solid. The hexagons describe the center of mass of the molecules and the circles the delocalized π-electron density. [51]

Hopping Transport

In disordered organic semiconductors like polymers the charge transport is dominated by localized states. Charge carriers are transported by thermally assisted hopping between localized states and are scattered at every step, so the carrier does not retain (completely or partially) memory of its previous hop. This motion is termed incoherent. Hopping is assisted by phonons and the mobility generally increases with the temperature. Mott suggested that in systems where the hopping transport occurs across a constant density of states (DOS), the hopping over long distances and hopping to higher energies are both to be considered. In this case, the dependence of the conductivity vs temperature can be expressed [52]:

$$\propto exp\left[-\left(\frac{T_0}{T}\right)^{\frac{1}{4}}\right] \qquad (6)$$

Even though there has been a lot of effort on this argument many basic aspects related to the physics of organic semiconductor thin film remain unclear. In field effect transistors, when a gate voltage is applied, the charge is accumulated at the semiconductor-dielectric interface. The lower states of the organic semiconductor are filled from the accumulation charge carriers and any further charges will occupy states at higher energies. This means that this additional charge needs less activation energy to hop between sites. Vissenberg and Matters [53] developed a model to describe the temperature and carrier density dependency of the mobility in amorphous organic field effect transistors. Their approach expresses the number density of charge carriers as:

$$N(E) = \frac{N_t}{k_B T_0} exp\left(\frac{E}{k_B T_0}\right) \qquad (-\infty < E \leq 0) \qquad (7)$$

where N_t is the number of states per unit volume, k_B is the Boltzmann's constant, and T_0 is a parameter that indicates the width of the exponential distribution.

The field-effect mobility is calculated from the following expression:

$$\mu = \frac{\sigma_0}{e}\left(\frac{\pi\left(\frac{T_0}{T}\right)^3}{(2a)^3 B_c \Gamma\left(\frac{1-T}{T_0}\right)\Gamma\left(\frac{1+T}{T_0}\right)}\right)^{T_0/T} \times \left[\frac{(C_i V_G)^2}{2k_B T_0 \varepsilon_S}\right]^{T_0/T-1} \qquad (8)$$

where B_c is a numerically derived constant and for 3D amorphous systems is 2.8 [54], σ_0 is a conductivity pre-factor, e the elementary charge, T_0 is a characteristic parameter describing the width of the exponential DOS, k_B is Boltzmann's constant, V_G is the gate voltage, ε_s dielectric constant, C_i the capacitance per unit area, and α an effective overlap parameter and $\Gamma(a) = \int_0^\infty dx\, exp(-x)x^{a-1}$.

Therefore, the mobility for hopping transport exhibits an Arrhenius behavior

$$\mu_{FE} \propto exp\left[\frac{-E_a}{kT}\right] \quad (9)$$

where E_α is the activation energy dependent on V_G. When the gate voltage is increasing (negative), E_α decreases. This results in the accumulation of the charge carriers that fill the lower-lying states and the additional charge carriers induced in the system will occupy sites with a higher energy with the advantage that less energy will be required for the activated jumps to neighboring sites.

The multiple trapping and release mechanism

Another model that was used to describe the low mobility in amorphous organic materials is the multiple trapping and release model (MTR) [51]. This model assumes an exponential distribution of gap states. The injected charges or the charges which are already inside the semiconductor are trapped into localized states with a probability close to one and their release is controlled by a thermally activated process (Fig. 1.10). The drift mobility μ_D is given by:

$$\mu_D = \mu_0 a\, exp\left(-\frac{E_T}{k_B T}\right) \quad (10)$$

where μ_0 is the mobility at the band edge, α is the ratio between the effective density of states at the transport band edge and the density of traps and E_T is the energy of the trap state.

FIG. 1.10. Principle of charge transport limited by multiple trapping and thermal release. [51]

An important outcome of this model is that the mobility is gate voltage dependent. When a voltage is applied to the gate, a potential V_s is formed at the semiconductor-dielectric interface. This provokes the shift of the Fermi level towards the band edge, thus partly filling the distribution of localized states (Fig. 1.11). Thus, any additional charge carriers have their energy closer to the band edge which makes its thermal release easier, implying a mobility increase. The effective mobility is given by

$$\mu_{eff} = \mu_0 \frac{N_c}{N_t} \left(\frac{C_i (V_G - V_{th})}{q N_t} \right)^{\frac{T_0}{T-1}} \qquad (11)$$

where N_c is the effective density of states at the transport band edge.

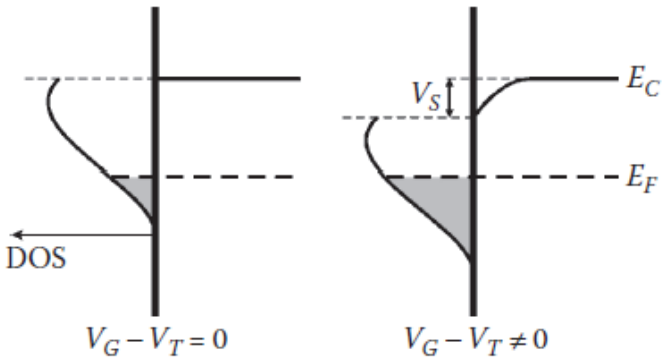

FIG. 1.11. Gate voltage dependent mobility induced by an energy distributed density of traps according to the MTR mechanism. [51]

1.6 Growth of thin films

Thin film growth is controlled by the interplay of thermodynamics, which determines the different energy barriers, and kinetics as the system is usually kept out of equilibrium conditions during the thin film deposition process. The general modes in film growth are understood within the thermodynamic approach in terms of relative surface and interface energies. On the other hand, since film growth is a non-equilibrium kinetic process, the rate-limiting steps are more influential onto the resulting growth mode.

Surface growth is often correlated with the formation of a physical surface such as growing crystals and metals. This is a large area thin film growth and consists of different application such as crystal growth [55], biological growth [56], and metal growth [57].

Models based on stochastic continuum growths equations are often able to predict the scaling exponents with an analytical way and they can be described through the form

$$\frac{\partial h(\boldsymbol{x},t)}{\partial t} = \Phi(h, \boldsymbol{x}, t) + \eta(\boldsymbol{x}, t) \qquad (12)$$

In which $h(x,t)$ is the height position x and the time t, $\Phi(h,x,t)$ is the function that reflects the modelled growth process, $\eta(x,t)$ is the noise term and more specifically the random fluctuations in the deposition of the particles.

The simplest growth model is when particles are randomly generated at a position and deposited in a random place of size L, occupying the position immediately above the surface at the site. This is called a random deposition model (RD). The columns of a generated RD surface have no correlation with each other and thus each column grows independently. It is then unlikely that the surface reaches the saturation. More specifically, α and z exponents could not be identified.

An experimental growth process is appropriately described by a theoretical model (or a combination of one or more different models) when it provides indications to control the surface roughness. Simple models were studied in order to understand the growth dynamics of pentacene thin films. A simple model that can describe the growth oscillations is the discrete growth

model [58] where the rate for a jump from layer *n+1* to *n* is proportional to the uncovered fraction of the layer *n+1* and the available space in layer *n*:

$$\frac{d\theta_n}{d\left({}^{t}/_{\tau}\right)} = \left(\theta_{n_{-1}} - \theta_n\right) + k_n(\theta_{n+1} - \theta_{n+2})(\theta_{n+1} - \vartheta_n) - k_n(\theta_{n-2} - \theta_n - 1)(\theta_n - \theta_{n+1}) \quad (13)$$

where θ_n is the fractional coverage of the n^{th} layer, τ is the completion time for one monolayer and k_n is the effective rate for interlayer transport.

Studies on thermodynamics of nucleation for pentacene done by Verlaak et al. [59] as a function of substrate temperature and the growth rate. In Fig. 1.12 is represented the nucleation phase diagram. It can be noted that only films grown below the dotted line (2D nucleation) grow in a layer-by-layer mode. Since growth mode depends also on the surface roughness, transitions to 3D growth can occur with enhanced stacking of monolayer terraces before the completion of the underlying layers during the thin film growth. This phenomenon is frequently observed in pentacene thin films and can be attributed to the fact that there is a spatial dependence of the van der Waals interaction between impinging molecules and the growing islands with the increase of the deposited mass quantified by the film thickness.

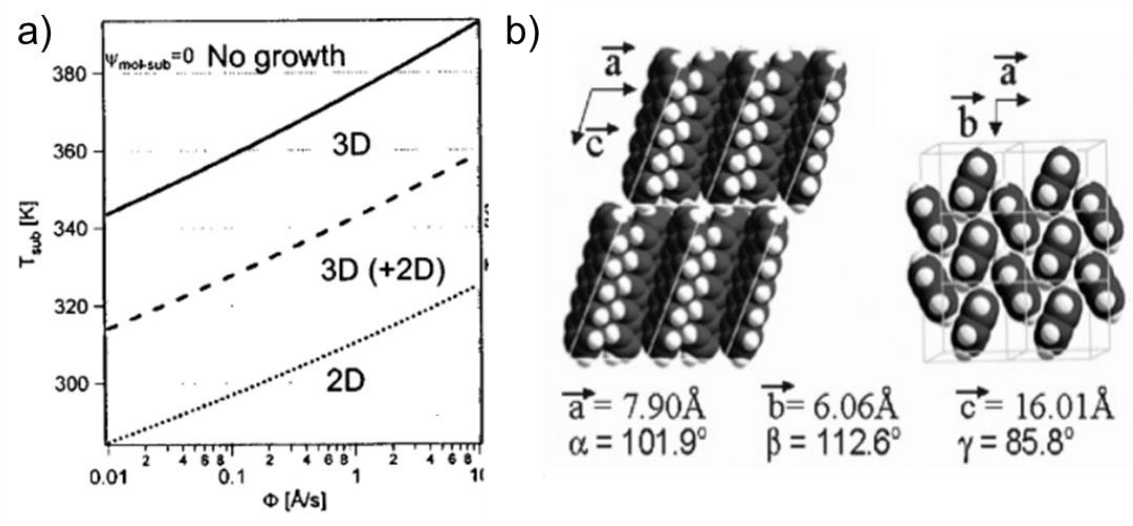

FIG. 1.12. a) Growth modes for pentacene assuming $\psi_{mol\text{-}sub} = 0$ (interaction strength between one molecule and the substrate being zero) [24]. Below the solid line, three-dimensional (3D) nucleation is possible. For growth conditions below the dashed line, two-dimensional (2D) nucleation is possible. 2D nucleation becomes more likely than 3D nucleation only below the dotted line. In a first approximation, only growth conditions below the dotted lines will give rise to continuous films [59] *(b) Bulk (Campbell's) crystalline structure of pentacene.* [60]

Another important factor is the self-diffusional barriers that also include the Schwoebel barrier. The latter is the energy barrier for molecules to diffuse across a terrace edge, which would lead to smoothening of the stacked structures and the completion of the underlying layers. The increase of the Schwoebel barrier *vs* thickness leads to rapid up-hill flow of pentacene molecules, thus effectively driving the transition from 2D to 3D.

The control of thin film growth plays an important role on the performances of OFET. Different studies have shown the correlation between the morphology and the electrical properties. [61,62] Thus, the charge transport is strongly correlated with the surface of the organic film which means that surface defects and roughness can essentially influence the charge motion. Due to the fact that the percolation channel for the charge carriers is in contact with the gate dielectric, early stages of the growth and thin film morphology plays an important role.

This is marked by a strong increase in research activity on the topographic structure of surfaces that influences a wide range of phenomena such as charge transport, interface formation and film growth. [63,64] Film growth is an non-equilibrium phenomenon: this means that equilibrium arguments and dynamic scaling are both needed to describe it. An intense theoretical activity has tried to describe, with different growth models, interfaces which are grown under non-equilibrium conditions and exhibit irregular geometries. [65–69] Thin films grown by organic molecular beam deposition (OMBD) such as pentacene typically grown to layer-by-layer, and after the first two-three monolayers there is a transition to island growth. [66] This kind of transition, that reminds

the Stranski-Krastanov 2D-3D transition, cannot be described with stress release by nucleation of disordered 3D aggregates.

1.8 Wetting/dewetting

The study of dewetting of single crystal films have driven the alternate view of looking at growth transitions using arguments of wetting/dewetting transitions. Thin films are generally formed under conditions for which atomic motion is limited and non-equilibrium structures can be attained. This happens especially for films formed by vapor deposition. In this case, the atoms arriving on the surface of the substrate move across the surface. Consequently, this can lead to continuous film formation that, however, owing to the instability caused by mismatched surface tensions, will spontaneously dewet to form islands. Other parameters which help to the rupture of the film are thermal shocks and vibrations which give to the atoms a sufficiently high mobility to break the film. [70] In wetting conditions, the spreading parameter (S) is positive and corresponds to a stable film. On the other hand, when spreading parameter is negative the film that forms could be metastable or unstable [71]. Three different mechanisms of dewetting can be observed (Fig 1.13): first, the film is ruptured and starts to shrink to yield a small nucleus that will evolve into holes (Fig. 1.13a). Second, spinodal dewetting in which the film is continuous up to a critical thickness then, in short time, it exhibits collective fluctuations of amplitude as large as thickness until the film breaks (Fig. 1.13b). Above this critical thickness dewetting will not occur and the cast film will remain continuous. The last mechanism is Ostwald ripening where larger islands, whose chemical potential is lower than the one of small islands, incorporate the neighbor small islands, leading to self-organized island patterns (Fig. 1.13c). [72]

According to spinodal dewetting theory, small and spontaneous deformations of the substrate can lead to an unstable film at a specific critical thickness which is given by:

$$h_c = \left(\frac{3K\Lambda^2}{64\gamma}\right)^{\frac{1}{4}} \qquad (14)$$

when K is a constant proportional to the Hamaker constant $A = 6\pi K$, γ surface tension and Λ is the wavelength of the fluctuation.

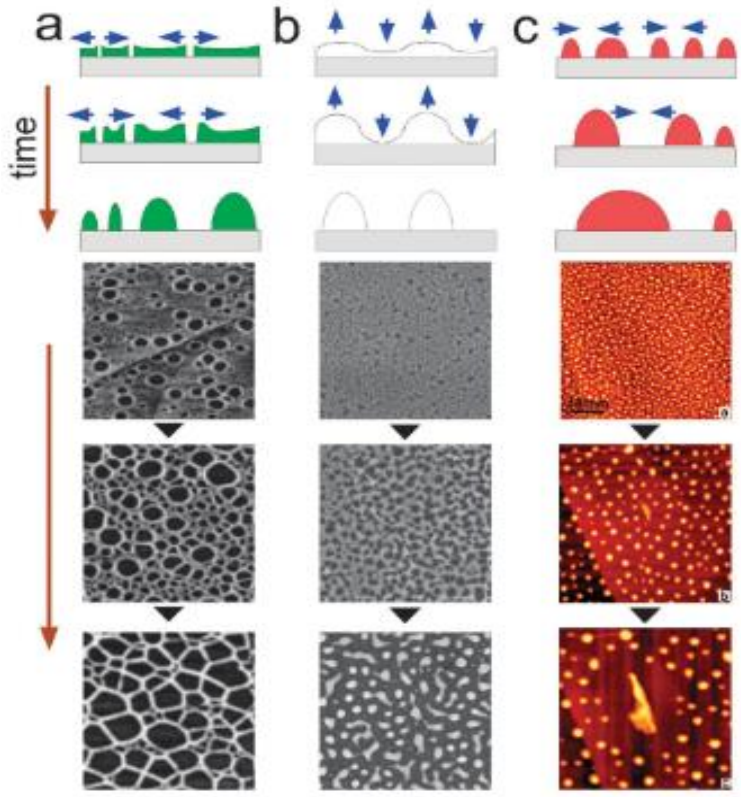

FIG. 1.13. Top rows: schematic representation; bottom rows: experimental examples of the time evolution of ruptured thin films. (a) Dewetting by nucleation, growth, and coalescence of holes. [73] *(b) spinodal dewetting;* [74] *(c) Evolution of a dewetted film by Ostwald ripening followed by crystallization.* [75]

Wetting/dewetting transitions are less consolidated in conjugated organic thin films, while they are often mentioned in the surface science community, especially in thin metal film growth. [76] Wetting/dewetting was originally applied to fluid layers, then extended to viscous and solid

amorphous films. Our group introduced wetting/dewetting transitions in the deposition of conjugated nanostructures in technological applications. [72] The peculiarity of organic thin films here is that films are solid and possess a high degree of crystal order both within each molecular plane and in the stacking of multiple molecular planes. The order parameter seems to be maintained with continuity across the roughening transition, [66,77,78] whereas transitions from thin film to bulk polymorphs [60,79] are observed at larger thicknesses. [80]

1.9 Scanning probe microscopies

Scanning Probe Microscopy techniques (SPM) are very important and very promising to understand the physics of the Organic Field Effect Transistors. In order to improve the performance of these devices non-destructive techniques that allow one to control and study the properties of the organic material at nanoscale level are demanded.

Atomic Force Microscopy (AFM) plays an important role in the investigation of the morphology of the organic materials. Previous studies have already shown that the morphology is strongly correlated with the electrical properties of the thin film [61,81]. With this technique it is able to study the growth dynamics of the semiconductive thin film [82]. Different studies of the thin film growth as well as in the investigation of the morphology using SPM and especially AFM will provide solutions to the comprehension and optimization of the Organic Field Effect Transistors. Despite the success of AFM, the technique confronts some limitations from the point of view of quantitative analysis and spatial resolution. In order to overcome these limitations, bimodal AFM, which is a technique that can provide fast, quantitative and high-resolution information of elastic properties of soft matter at the nanoscale level, shone. The working operation of this technique is based on the oscillation of the cantilever in two eigenmodes. A variety of applications have been referred for the use of Amplitude modulation - Frequency modulation AFM in materials and macromolecules like proteins [83], lipid layers [84], DNA [85,86], cells [87], self-assembled monolayers [88], 2D materials [89] and organic semiconductor devices [90].

AFM-based techniques have been developed to study different properties of the materials such as electrical, mechanical, chemical etc. Those techniques allow us to go beyond the macroscopic properties of the materials, providing information at the nanoscale level and also correlation of growth vs time [69,88,91]. Moreover, mechanically strained flexible organic electronics have also been studied using kelvin probe microscopy (KPM) in order to measure locally the effect of the strain deformation on the electronic properties [92]. The use of phase electrostatic force microscopy (PEFM) has also been studied in order to control the electrostatic potential of the OFET. [93,94] Studies on the interfacial capacitance and conductivity of EGOFETs, were performed thanks to the Scanning Dielectric Microscopy (in-liquid SDM) [95].

1.10 Aim of this thesis

The aim of this thesis is to understand the correlation between different growth modes, the resulting morphology, and the electrical response both in solid state OFETs and in EGOTs. More specifically, morphological changes that can assimilated to wetting/dewetting transition were observed during the thin film growth. When dewetting/3D layer nucleation occurs at the early stages of growth, film roughness exhibits oscillations superimposed to a self-affine power law scaling. The thickness periodicity of these roughness oscillations increases as thickness increases, while the amplitude varies more slowly but does not damp. This peculiar growth mode, where the abrupt transition from layer-by-layer to island growth is not apparent was not reported before and demonstrates a distinctive growth mode where wetting/dewetting transitions occur continuously and repeatedly. For analyzing this growth mode, a phenomenological expression for the surface roughness was developed that can describe the oscillations of the root mean square (rms) roughness at different frequency as film thickness increases. Apart from the roughness oscillations, correlation length ξ follows similar behavior as well as the main transistor parameters in the solid state, viz. transconductance and threshold voltage indicating that the growing islands are electrostatically coupled to the continuous channel formed underneath. Interestingly, the oscillations are less marked in EGOFETs thus suggesting that the ions are coupled not just to the basal plane, but to the same transport layer that must reside deeper than the (oscillating) surface.

The thesis is organized as follows: **Chapter 1** presents a brief introduction to the organic field effect transistors as well as in the semiconductive materials, highlighting the growth mechanisms of thin films and the wetting/dewetting phenomena. An explanation of Atomic Force Microscopy and its contribution in the surface analysis is then discussed. **Chapter 2** refers to the different materials and methods that we have used for the experimental study and the techniques that we used to measure and extract the relevant parameters. In **Chapter 3** the investigation and details of the new growth mode of pentacene thin films are presented. An anomalous type of growth is observed with the increase of the thickness. An empirical equation is provided, that can describe the evolution of the roughness versus thickness. In **Chapter 4** we focused on the correlation of the electrical properties of thin film transistors with the morphology. Experiments both in air and in an electrolytic environment occurred. A correlation of this anomalous growth of the pentacene thin films with the electrical parameters is discussed in this chapter. In **Chapter 5** we describe how Bimodal AFM works and how we used it to study the mechanical properties of the conductive and semiconductive materials. In particular, we touched the influence of the substrate on thin and soft polymer layers which is known as bottom effect artifact as well as to the swelling phenomenon of conducting polymer when a voltage is applied.

1.11 References

[1] A. Tsumura, H. Koezuka, and T. Ando, Appl. Phys. Lett. **49**, 1210 (1986).

[2] C. W. Tang and S. A. Vanslyke, Appl. Phys. Lett. **51**, 913 (1987).

[3] H. Conducting, E. Poly, K. Jen, G. G. Miller, and R. L. Elsenbaumer, **5**, 1346 (1986).

[4] A. Assadi, C. Svensson, M. Willander, and O. Inganäs, Appl. Phys. Lett. **53**, 195 (1988).

[5] H. Shirakawa, E. J. Louis, A. G. MacDiarmid, C. K. Chiang, and A. J. Heeger, J. Chem. Soc. Chem. Commun. 578 (1977).

[6] G. H. Gelinck, T. C. T. Geuns, and D. M. De Leeuw, Appl. Phys. Lett. **77**, 1487 (2000).

[7] M. Halik, H. Klauk, U. Zschieschang, G. Schmid, C. Dehm, M. Schütz, S. Maisch, F. Effenberger, M. Brunnbauer, and F. Stellacci, Nature **431**, 963 (2004).

[8] S. R. Forrest, Nature **428**, 911 (2004).

[9] G. H. Gelinck, H. E. A. Huitema, E. Van Veenendaal, E. Cantatore, L. Schrijnemakers, J. B. P. H. Van Der Putten, T. C. T. Geuns, M. Beenhakkers, J. B. Giesbers, B. H. Huisman, E. J. Meijer, E. M. Benito, F. J. Touwslager, A. W. Marsman, B. J. E. Van Rens, and D. M. De Leeuw, Nat. Mater. **3**, 106 (2004).

[10] J. H. Burroughes, D. D. C. Bradley, A. R. Brown, R. N. Marks, K. Mackay, R. H. Friend, P. L. Burns, and A. B. Holmes, Nature **347**, 539 (1990).

[11] W. Clemens, W. Fix, J. Ficker, A. Knobloch, and A. Ullmann, J. Mater. Res. **19**, 1963 (2004).

[12] M. Berto, C. Diacci, L. Theuer, M. Di Lauro, D. T. Simon, M. Berggren, F. Biscarini, V. Beni, and C. A. Bortolotti, Flex. Print. Electron. **3**, 024001 (2018).

[13] M. Kaltenbrunner, T. Sekitani, J. Reeder, T. Yokota, K. Kuribara, T. Tokuhara, M. Drack, R. Schwödiauer, I. Graz, S. Bauer-Gogonea, S. Bauer, and T. Someya, Nature **499**, 458 (2013).

[14] G. Mattana, P. Cosseddu, B. Fraboni, G. Malliaras, J. P. Hinestroza, and A. Bonfiglio, Org. Electron. **12**, 2033 (2011).

[15] A. Campana, T. Cramer, D. T. Simon, M. Berggren, and F. Biscarini, Adv. Mater. **26**, 3873 (2014).

[16] L. Kergoat, L. Herlogsson, D. Braga, B. Piro, M.-C. Pham, X. Crispin, M. Berggren, and G. Horowitz, Adv. Mater. **22**, 2565 (2010).

[17] L. Torsi, G. M. Farinola, F. Marinelli, M. C. Tanese, O. H. Omar, L. Valli, F. Babudri, F. Palmisano, P. G. Zambonin, and F. Naso, Nat. Mater. **7**, 412 (2008).

[18] K. M. Persson, R. Karlsson, K. Svennersten, S. Löffler, E. W. H. Jager, A. Richter-Dahlfors, P. Konradsson, and M. Berggren, Adv. Mater. **23**, 4403 (2011).

[19] T. Cramer, B. Chelli, M. Murgia, M. Barbalinardo, E. Bystrenova, D. M. de Leeuw, and F. Biscarini, Phys. Chem. Chem. Phys. **15**, 3897 (2013).

[20] J. Reeder, M. Kaltenbrunner, T. Ware, D. Arreaga-Salas, A. Avendano-Bolivar, T. Yokota, Y. Inoue, M. Sekino, W. Voit, T. Sekitani, and T. Someya, Adv. Mater. **26**, 4967 (2014).

[21] D. Khodagholy, T. Doublet, P. Quilichini, M. Gurfinkel, P. Leleux, A. Ghestem, E. Ismailova, T. Hervé, S. Sanaur, C. Bernard, and G. Malliaras, Nat. Commun. **4**, 1575 (2013).

[22] S. C. B. Mannsfeld, B. C. K. Tee, R. M. Stoltenberg, C. V. H.-H. Chen, S. Barman, B. V. O. Muir, A. N. Sokolov, C. Reese, and Z. Bao, Nat. Mater. **9**, 859 (2010).

[23] D. Khodagholy, J. N. Gelinas, T. Thesen, W. Doyle, O. Devinsky, G. Malliaras, and G. Buzsáki, Nat. Neurosci. **18**, 310 (2015).

[24] S. Lai, A. Zucca, P. Cosseddu, F. Greco, V. Mattoli, and A. Bonfiglio, Org. Electron. Physics, Mater. Appl. **46**, 60 (2017).

[25] S. Wang, J. Xu, W. Wang, G. J. N. Wang, R. Rastak, F. Molina-Lopez, J. W. Chung, S. Niu, V. R. Feig, J. Lopez, T. Lei, S. K. Kwon, Y. Kim, A. M. Foudeh, A. Ehrlich, A. Gasperini, Y. Yun, B. Murmann, J. B. H. Tok, and Z. Bao, Nature **555**, 83 (2018).

[26] X. Strakosas, M. Bongo, and R. M. Owens, J. Appl. Polym. Sci. (2015).

[27] J.-H. Kim, M. J. Han, and S. Seo, J. Polym. Sci. Part B Polym. Phys. **53**, 453 (2015).

[28] R. G. Kepler, Phys. Rev. **119**, 1226 (1960).

[29] M. Pope, H. P. Kallmann, and P. Magnante, J. Chem. Phys. **38**, 2042 (1963).

[30] O. H. LeBlanc, J. Chem. Phys. **33**, 626 (1960).

[31] H. Hoegl, J. Phys. Chem. **69**, 755 (1965).

[32] Y. Y. Pan, J. Huang, Z. M. Wang, D. W. Yu, B. Yang, and Y. G. Ma, RSC Adv. **7**, 26697 (2017).

[33] A. Kahn, Mater. Horizons **3**, 7 (2016).

[34] J. E. Lilienfeld, 28 (1926).

[35] W. Shockley and G. L. Pearson, Phys. Rev. **74**, 232 (1948).

[36] J. Bardeen and W. H. Brattain, Bell Syst. Tech. J. **28**, 239 (1949).

[37] K. Dawon, U.S. Pat. 3102230 4 (1963).

[38] B. Fallahazad, K. Lee, G. Lian, S. Kim, C. M. Corbet, D. A. Ferrer, L. Colombo, and E. Tutuc, Appl. Phys. Lett. **100**, 093112 (2012).

[39] M. Zirkl, A. Haase, A. Fian, H. Schön, C. Sommer, G. Jakopic, G. Leising, B. Stadlober, I. Graz, N. Gaar, R. Schwödiauer, S. Bauer-Gogonea, and S. Bauer, Adv. Mater. **19**, 2241 (2007).

[40] S. Ritjareonwattu, Y. Yun, C. Pearson, and M. C. Petty, IEEE Sens. J. **12**, 1181 (2012).

[41] B. Stadlober, M. Zirkl, M. Beutl, G. Leising, S. Bauer-Gogonea, and S. Bauer, Appl. Phys. Lett. **86**, 242902 (2005).

[42] N. A. Choudhury, S. Sampath, and A. K. Shukla, Energy Environ. Sci. **2**, 55 (2009).

[43] M. Sensi, M. Berto, S. Gentile, M. Pinti, A. Conti, G. Pellacani, C. Salvarani, A. Cossarizza, C. A. Bortolotti, and F. Biscarini, Chem. Commun. (2021).

[44] F. Booth, J. Chem. Phys. **19**, 391 (1951).

[45] B. E. Conway, J. O. M. Bockris, and I. A. Ammar, Trans. Faraday Soc. **47**, 756 (1951).

[46] C. D. Dimitrakopoulos and P. R. L. Malenfant, Adv. Mater. **14**, 99 (2002).

[47] T. Cramer, A. Kyndiah, M. Murgia, F. Leonardi, S. Casalini, and F. Biscarini, Appl. Phys. Lett. **100**, (2012).

[48] M. Di Lauro, M. Berto, M. Giordani, S. Benaglia, G. Schweicher, D. Vuillaume, C. A. Bortolotti, Y. H. Geerts, and F. Biscarini, Adv. Electron. Mater. **3**, (2017).

[49] W. Warta and N. Karl, Phys. Rev. B **32**, 1172 (1985).

[50] O. D. Jurchescu, J. Baas, and T. T. M. Palstra, Appl. Phys. Lett. **84**, 3061 (2004).

[51] Z. Bao and J. Locklin, *Organic Field-Effect Transistors*, 1st Editio (CRC Press, 2018).

[52] N. F. M. and E. A. Davis., *Electronic Processes in Non-Crystalline Materials, 2nd Ed.* (Oxford : Clarendon Press, 2012).

[53] M. C. J. M. Vissenberg and M. Matters, Phys. Rev. B **57**, 12964 (1998).

[54] C. H. Seager and G. E. Pike, Phys. Rev. B **10**, 1435 (1974).

[55] A. C. Levi and M. Kotrla, J. Phys. Condens. Matter **9**, 299 (1997).

[56] D. Ambrosi, G. A. Ateshian, E. M. Arruda, S. C. Cowin, J. Dumais, A. Goriely, G. A. Holzapfel, J. D. Humphrey, R. Kemkemer, E. Kuhl, J. E. Olberding, L. A. Taber, and K. Garikipati, J. Mech. Phys. Solids **59**, 863 (2011).

[57] J. Shen, Z. Gai, and J. Kirschner, Surf. Sci. Rep. **52**, 163 (2004).

[58] P. I. Cohen, G. S. Petrich, P. R. Pukite, G. J. Whaley, and A. S. Arrott, Surf. Sci. **216**, 222 (1989).

[59] S. Verlaak, S. Steudel, P. Heremans, D. Janssen, and M. S. Deleuze, Phys. Rev. B **68**, 195409 (2003).

[60] R. B. Campbell, J. M. Robertson, and J. Trotter, Acta Crystallogr. **14**, 705 (1961).

[61] F. Dinelli, M. Murgia, P. Levy, M. Cavallini, F. Biscarini, and D. M. de Leeuw, Phys. Rev. Lett. **92**, 116802 (2004).

[62] F. Cicoira, C. Santato, F. Dinelli, M. Murgia, M. A. Loi, F. Biscarini, R. Zamboni, P. Heremans, and M. Muccini, Adv. Funct. Mater. **15**, 375 (2005).

[63] D. Knipp, R. A. Street, A. Völkel, and J. Ho, J. Appl. Phys. **93**, 347 (2003).

[64] F. Schreiber, Phys. Status Solidi **201**, 1037 (2004).

[65] A.-L. Barabási and H. E. Stanley, in *Fractal Concepts Surf. Growth* (Cambridge University Press, 1995), pp. 1–18.

[66] F. Biscarini, P. Samorí, O. Greco, and R. Zamboni, Phys. Rev. Lett. **78**, 2389 (1997).

[67] A. C. Mayer, A. Kazimirov, and G. Malliaras, Phys. Rev. Lett. **97**, 1 (2006).

[68] F. J. Meyer zu Heringdorf, M. C. Reuter, and R. M. Tromp, Nature **412**, 517 (2001).

[69] R. Ruiz, D. Choudhary, B. Nickel, T. Toccoli, K.-C. Chang, A. C. Mayer, P. Clancy, J. M. Blakely, R. L. Headrick, S. Iannotta, and G. Malliaras, Chem. Mater. **16**, 4497 (2004).

[70] J. A. Kitcherner, in edited by A. C. R. J.F. Danielli, K.G.A. Panhurst (1964), pp. 51–93.

[71] F. B. Wyart and J. Daillant, Can. J. Phys. **68**, 1084 (1990).

[72] D. Gentili, G. Foschi, F. Valle, M. Cavallini, and F. Biscarini, Chem. Soc. Rev. **41**, 4430 (2012).

[73] U. Thiele, M. Mertig, and W. Pompe, Phys. Rev. Lett. **80**, 2869 (1998).

[74] Y. Wu, J. D. Fowlkes, and P. D. Rack, J. Mater. Res. **26**, 277 (2011).

[75] F. Biscarini, M. Cavallini, R. Kshirsagar, G. Bottari, D. A. Leigh, S. Leon, and F. Zerbetto, Proc. Natl. Acad. Sci. **103**, 17650 (2006).

[76] S. Herminghaus, K. Jacobs, K. Mecke, J. Bischof, A. Fery, M. Ibn-Elhaj, and S. Schlagowski, Science (80-.). **282**, 916 (1998).

[77] X. N. Zhang, E. Barrena, D. G. de Oteyza, and H. Dosch, Surf. Sci. **601**, 2420 (2007).

[78] A. C. Dürr, F. Schreiber, K. A. Ritley, V. Kruppa, J. Krug, H. Dosch, and B. Struth, Phys. Rev. Lett. **90**, 4 (2003).

[79] D. Holmes, S. Kumaraswamy, A. J. Matzger, and K. P. C. Vollhardt, Chem. - A Eur. J. **5**, 3399 (1999).

[80] J. F. Moulin, F. Dinelli, M. Massi, C. Albonetti, R. Kshirsagar, and F. Biscarini, Nucl. Instruments Methods Phys. Res. Sect. B Beam Interact. with Mater. Atoms **246**, 122 (2006).

[81] A. Shehu, S. D. Quiroga, P. D'Angelo, C. Albonetti, F. Borgatti, M. Murgia, A. Scorzoni, P. Stoliar, and F. Biscarini, Phys. Rev. Lett. **104**, 1 (2010).

[82] S. Chiodini, A. Straub, S. Donati, C. Albonetti, F. Borgatti, P. Stoliar, M. Murgia, and F. Biscarini, J. Phys. Chem. C **124**, 14030 (2020).

[83] C. A. Amo, A. P. Perrino, A. F. Payam, and R. Garcia, ACS Nano **11**, 8650 (2017).

[84] W. Trewby, J. Faraudo, and K. Voïtchovsky, Nanoscale **11**, 4376 (2019).

[85] M. Kocun, A. Labuda, W. Meinhold, I. Revenko, and R. Proksch, ACS Nano **11**, 10097 (2017).

[86] C.-Y. Lai, S. Santos, and M. Chiesa, ACS Nano **10**, 6265 (2016).

[87] A. X. Cartagena-Rivera, W.-H. Wang, R. L. Geahlen, and A. Raman, Sci. Rep. **5**, 11692 (2015).

[88] E.-N. Athanasopoulou, N. Nianias, Q. K. Ong, and F. Stellacci, Nanoscale **10**, 23027 (2018).

[89] Y. Li, C. Yu, Y. Gan, P. Jiang, J. Yu, Y. Ou, D.-F. Zou, C. Huang, J. Wang, T. Jia, Q. Luo, X.-F. Yu, H. Zhao, C.-F. Gao, and J. Li, Npj Comput. Mater. **4**, 49 (2018).

[90] R. Giridharagopal, L. Q. Flagg, J. S. Harrison, M. E. Ziffer, J. Onorato, C. K. Luscombe, and D. S. Ginger, Nat. Mater. **16**, 1 (2017).

[91] F. Biscarini, 163 (2009).

[92] T. Cramer, L. Travaglini, S. Lai, L. Patruno, S. de Miranda, A. Bonfiglio, P. Cosseddu, and

B. Fraboni, Sci. Rep. **6**, 38203 (2016).

[93] P. Annibale, C. Albonetti, P. Stoliar, and F. Biscarini, J. Phys. Chem. A **111**, 12854 (2007).

[94] C. Albonetti, S. Chiodini, P. Annibale, P. Stoliar, R. V. Martinez, R. Garcia, and F. Biscarini, J. Microsc. **280**, 252 (2020).

[95] A. Kyndiah, M. Checa, F. Leonardi, R. Millan-Solsona, M. Di Muzio, S. Tanwar, L. Fumagalli, M. Mas-Torrent, and G. Gomila, Adv. Funct. Mater. **2008032**, 1 (2020).

Chapter 2

Experimental techniques materials and methods

"In this chapter, are reported all the materials and techniques used in this thesis. The substrates, the deposition methods of organic semiconductor films as well as all the characterization techniques are discussed in detail. Finally, the extraction of the parameters that were used are reported in an analytical way."

2.1 Introduction to the organic growth dynamics

During this thesis I focused on the growth of pentacene thin films by means of organic molecular beam deposition (OMBD) technique. The growth of organic molecule films is a non-equilibrium phenomenon, where the growth kinetics plays a crucial role. First, the molecules that arrive to the surface can interact in various ways with the substrate: in the simplest case, the molecule can be reflected into the vacuum. In Fig. 2.1 is shown a schematic potential energy diagram that represents the interactions of the molecule with the substrate. The r_c and r_p are the distances from the surface.

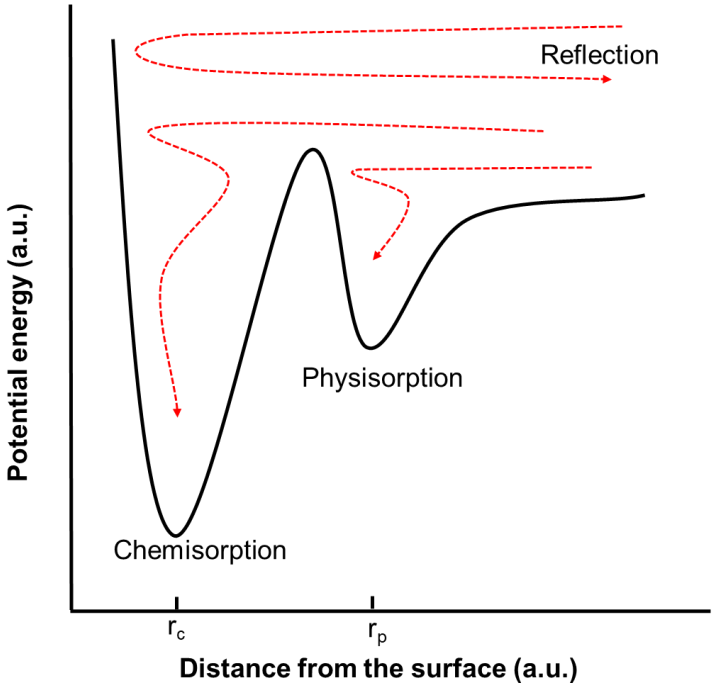

FIG. 2.1. shows a simplified potential energy curve as a function of the molecule-surface distance.

On the other hand, when a molecule moves with too low energy is reflected by an energy barrier to the first minimum. Since the molecules does not arrive to the surface, does not contribute to film formation on the substrate. However, under specific conditions the molecule might stick to the surface. The probability that this happen is called sticking probability. If the molecule sticks on the surface, it is absorbed. In general, molecules can adsorb in various ways: when there is only a weak Van der Waals interaction between the surface and the molecule, the latter is said

physiosorbed. When, on the other hand, the molecule interacts more strongly with the substrate, for example through covalent bonds, the molecule is said chemisorbed. It is rare that molecules have sufficient energy to go directly to a chemisorbed state. Sometimes, it is possible that the molecule overcomes the energy barrier between the bound state and the free state, or, in other words, the molecule could re-evaporate. This is detrimental to the film growth. More specific, when a pentacene molecule arrives on the silicon oxide surface physisorption is occurred. In general, when the molecules move across the surface is known as surface diffusion. Fig. 2.2 shows different kinetic processes relevant for the growth by OMBD, such us nucleation, surface diffusion, and desorption.

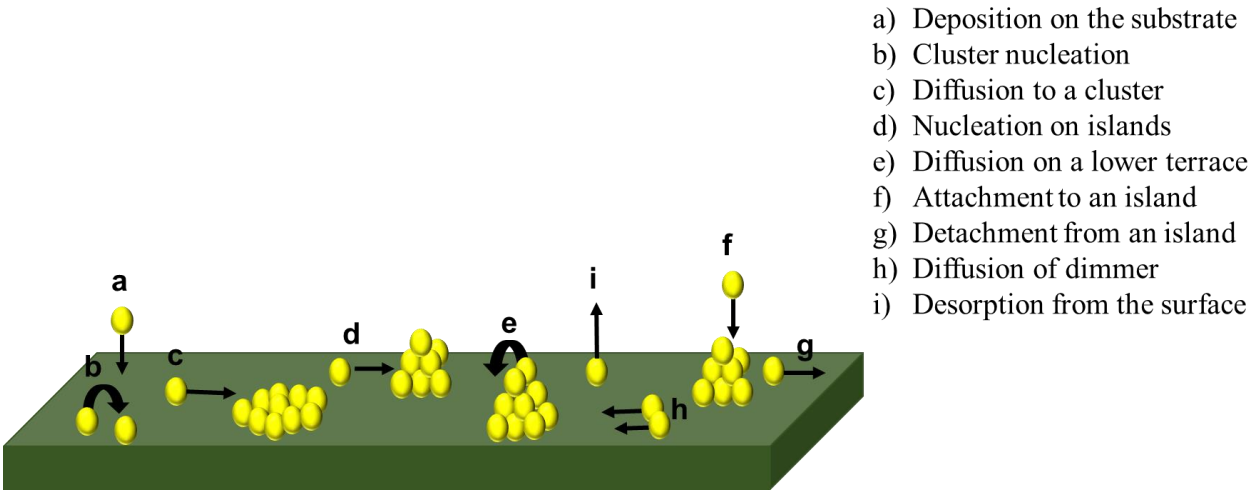

FIG. 2.2. Shows the different kinetic processes that can be occurred when a molecule arrives on the surface.

Classically, growth phenomena are classified according to three growth modes. The growth modes can be described using different arguments, such as epitaxy and the surface and interface energies. Two ancient Greek words *επί* (epi-placed or resting upon) and *τάξις* (taxis-arrangement) are the root of the modern word epitaxy, which describes the extended single-crystal film formation on top of a crystalline substrate. The dynamical behavior that the absorbed atoms can exhibit at the surface can be describe with the different modes: atoms can move around on the corresponding

surface; they can diffuse into the substrate or even desorb from the substrate. When two atoms meet, they form metastable nuclei, and this process is defined as nucleation. Nuclei can also separate, rotate, or diffuse through the surface. At a certain critical size, the nuclei become stable, and this is where actual crystal growth begins. Initial film growth is categorized into three different types of behaviors, called Volmer-Weber (VW), Stranski-Krastanov (SK), and Frank-van der Merwe (FM) [1]. (Fig. 2.3) In VW growth (Fig. 2.3a), three-dimensional (3D) nuclei start to form and later coalesce. In FM growth or layer-by-layer (LbL) growth (Fig. 2.3b) the film atoms are bound more strongly to the substrate than to each other. In this mode each layer must be fully completed before the next layer starts to grow. SK growth (Fig. 2.3c) is characterized by the layer-by-layer formation and after the 3D islands growth.

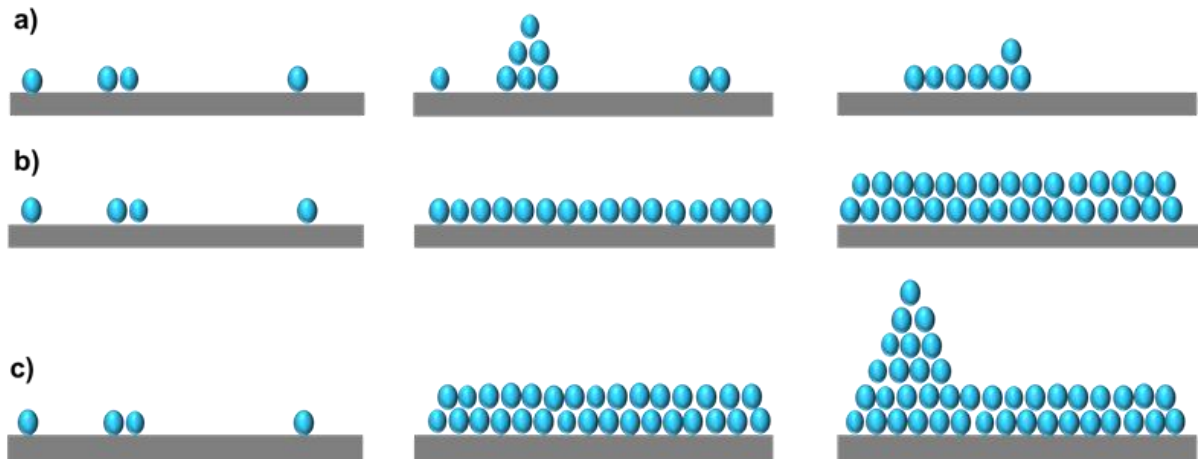

*FIG. 2.3. Shows the 3 different growth modes **a)** represents the to the VW growth **b)** shows the FM growth and **c)** illustrates the SK growth.*

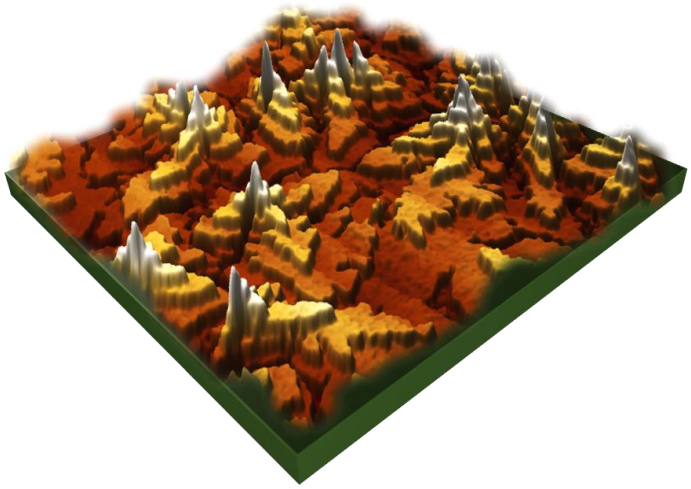

FIG. 2.4 represents 3D AFM images of 3nm pentacene thin film grown on SiO_2 substrates at 80°C.

2.1 Substrates and materials

2.1.1 Pentacene

The small molecule chosen for the experiments was pentacene, whose chemical structure is depicted in Fig. 2.5. It was discovered by Campbell in 1861 [2] and is one of the most promising organic semiconductors. [3–9] It consists of five condensed benzene rings, and it is a linear acene that has semiconductive characteristics thanks to the extended conjugation of its π-orbitals. The length of the pentacene molecule is around 1.45 nm. During the formation of the thin film two different phases of pentacene can take place. The bulk structure which is triclinic with two molecules in the unit cell and the thin film phase. [2] Both of these phases can coexist in the film and this coexistence is dependent on different parameters such as the surface, the film thickness and the temperature. [10] Usually, the thickness of the film is counted to monolayers which corresponds to 1.5 nm.

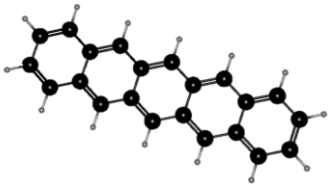

FIG. 2.5 Chemical structure of pentacene molecule

2.1.1 PEDOT: PSS

In chapter 5 (Section 5.3.2) the material that used for the experiments was Poly(3,4-ethylenedioxythiophene):poly(styrene-sulfonate) (PEDOT:PSS) is a conductive polyelectrolyte complex. PEDOT can be produced through polymerization of 3,4-ethylenedioxythiophene (EDOT) catalyzed by Fe (III) in the presence of excess peroxydisulfate, which oxidize the resulting conjugated polymer and renders it conductive. Electro-neutrality and water solubility are achieved by polymerizing EDOT in the presence of excess sodium poly(styrene-sulfonate)($Na^{+}PSS^{-}$): subsequently to a simple ionic exchange reaction the PSS poly-anion compensates the charge of the PEDOT poly-cation obtaining a neutral conductive material. [11] PEDOT:PSS (Fig. 2.6) has been used as a transparent stretchable electrode in a number of applications. [12–16] PEDOT:PSS is widely used as semiconductor in depletion-mode electrolyte gated architectures since it is possible to modulate its conductivity by driving cations at the interface between electrolyte and PEDOT: PSS. This capability of converting ionic currents in electronic ones led devices based on this principle like organic electrochemical transistors (OECTs) and organic electronic ion pumps (OEIP), to have great success as biological and chemical sensors. [17–21]

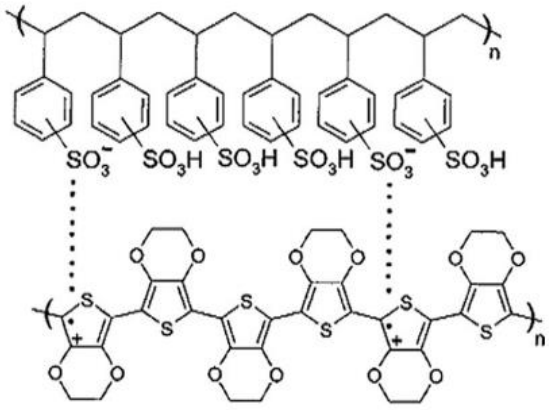

FIG. 2.6 Chemical structure of PEDOT:PSS

2.1.3 Test patterns

For this thesis two different kinds of substrates were used. The first test patterns (TPs) as shown in Fig. 2.7a were fabricated on a heavily doped Silicon wafer, 500 μm thick, with a resistivity of 0.01– 0.03 Ω*cm. 200 nm thick SiO_2 was thermally grown to make a dielectric layer. The capacitance of the dielectric is 17.25 nF/cm^2. Interdigitated Au electrodes (125 ± 25 nm thick) (Fig. 2.7c) were photolithographically patterned onto the SiO_2 using Chromium as adhesive layer (3–5 nm). On each test pattern, there are four transistors consisting of different channel length *L*=20 μm and 40 μm and channel width *W*=11200 μm and 22400 μm, respectively. The *W/L* ratio for all the four transistors is 560. FET1, FET2, FET3 and FET4 are the names assigned to the different transistors considering their geometry and position. The second type of device as shown in Fig. 2.7b was fabricated on quartz. Planar Au electrodes with thickness (50 ± 5 nm thick) were patterned through photolithography. Each pattern consists of four transistors of different channel length L=15 μm and 30 μm and W=150 μm and 300 μm, respectively. The *W/L* ratio for all the four transistors is 10. In Fig. 2.7d are represented the four devices assigned by F1, F2, F3 and F4.

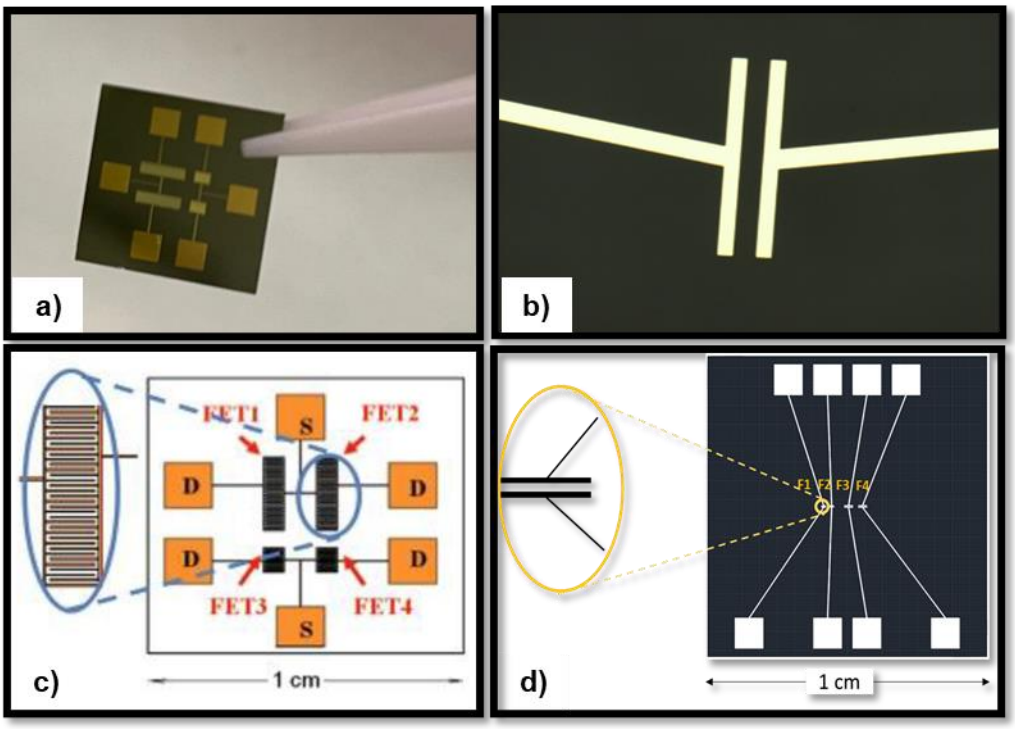

FIG. 2.7 illustrates the two kinds of the substates that have been used for this thesis experiments. a) and c) show SiO_2 wafer with the interdigitated electrodes b) and d) show quartz substrate with gold planar electrodes.

Before the deposition of the semiconductor, a standard protocol for the cleaning of the substrates was occurred. For the silicon substrates the procedure was as follow: first, the TPs were rinse with acetone in order to remove the photo resistive material then followed by drying it with nitrogen. Secondly, the TPs were dipped in hot piranha (H_2SO_4:H_2O_2, 1:1) for 15 mins at 150^{o}C in order to remove the organic contaminants. Then the TPs were rinsed with de-ionized (DI) water and dried with nitrogen. As last step, the TPs were dipped in HF (2%) solution for 5 seconds and rinsed with de-ionized water and dried with nitrogen. For the second type of device a different cleaning protocol was occurred. Firstly, the TPs were rinse with acetone in order to remove the photo resistive material and then the devices ere dipped in pure acetone for 15 min at 50^{o}C. As last step, the TPs were blown with dry nitrogen.

2.1.4 Surface modification

The performance of an OFET relies on the quality of the dielectric-semiconductor surface. It is often desirable to modify the dielectric layer with a surface treatment which has been shown to increase transistor mobilities. [23] The dielectric surface such as silicon oxide consists of terminated hydroxyl groups on the surface which acts as trap states that hinders the transport of charges. For this reason, we have modified the surface of the silicon oxide by a treatment with hexamethyldisiloxane (HMDS). Moreover, the HMDS layer on the silicon oxide makes the surface more hydrophobic and does not alter the morphology of the pentacene film growth.

The functionalization procedure of the silicon oxide surface with HMDS is done immediately after cleaning the substrate using the cleaning protocol discussed in Section 2.1.1. HMDS deposition was achieved by thermal evaporation of the molecule onto the substrate. Fig. 2.8 depicts the surface of silicon oxide before and after the functionalization with HMDS, respectively.

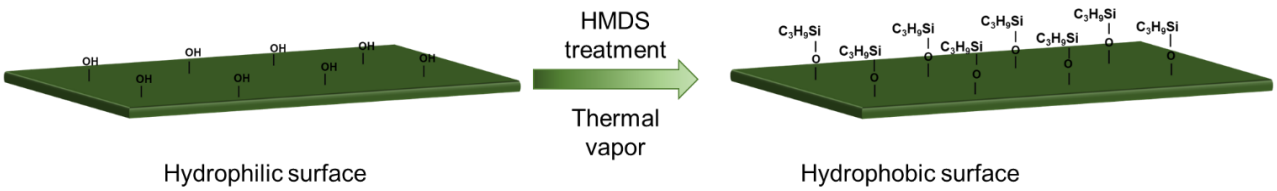

FIG. 2.8. Is shown the functionalization of the silicon dioxide substrate through thermal evaporation.

2.2 Semiconductor deposition

The most crucial part in the OFET fabrication is the deposition of the organic semiconductor. The deposition of small molecule organic semiconductor was done by high vacuum sublimation while, in the case of PEDOT: PSS, the deposition was performed by electropolymerization.

2.3 High vacuum sublimation of small organic semiconductor molecules

The growth of pentacene thin film is performed by sublimation in an experimental setup composed of high vacuum (HV) chamber, Knudsen cell, quartz crystal microbalance, shutter, and sample-holder (Fig. 2.9). The Knudsen cell is composed of quartz crucible, containing the organic semiconductor, and a heating Tungsten wire. The temperature of the crucible is increased by a proportional integral derivative (PID) controller. The particular geometry of each Knudsen cell and its position and orientation in the HV chamber determine the deposition rate measured near the sample at a certain temperature of the crucible. The substrate temperature is monitored through a thermocouple mounted on the sample-holder and can be also increased by using a second PID.

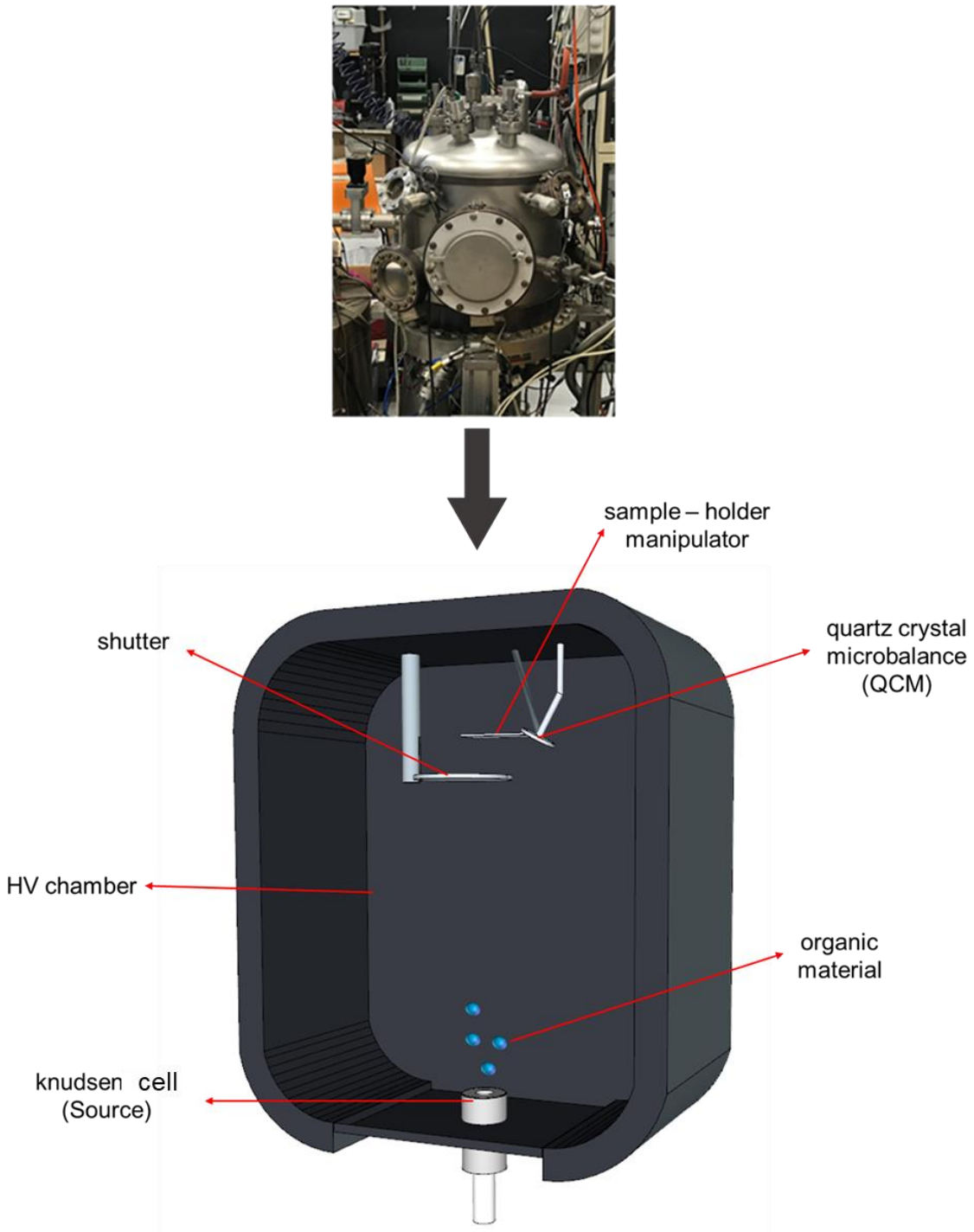

FIG. 2.9. A schematic figure which represents the OMBD technique. On the top, there is the high vacuum chamber and on the bottom analytical parts of the setup.

Procedure for the pentacene sublimation.

i. The TPs were placed in the sample holder.

ii. After that, the sample holder was entered inside the chamber and the shutter was closed.

iii. Purification of pentacene were occurred close to the sublimation temperature.

iv. The chamber was left for some hour in order to reach HV environment, in our case the sublimation vacuum was $6x10^{-6}$ mbar.

v. After the vacuum was reached, the stabilization of the deposition rate took place which can be controlled though the temperature.

vi. As last step was the removal of the shutter and the formation of the film. When the preferred thickness is reached the shutter close and the device is removed from the chamber.

Generally, the film growth in high vacuum assures that the minimal density of impurities and defects can affect the film. Of course, the degree of impurities which may deposited during the sublimation depends from the deposition rate and the quality of the vacuum. [24]

2.5 Electrodeposition

For the experiments occurred during my secondment in ICMM CSIC (Spain) I used quartz TPs. The deposition of the conductive material was done through electrodeposition as is represented in Fig. 2.10. In general, electrodeposition is a technique exploited in coating science. It is performed through the application of a constant current to a conductive material immersed into a solution containing the salt of the material to be deposited. In our case, the TP were covered by 50 μL of the solution containing EDOT in the presence of excess sodium poly(styrene-sulfonate)(Na^+PSS^-

). A current equal to 1 μA was applied for 10 s and the required film was obtained. The thickness of the film was measured with AFM and it was around 150 nm.

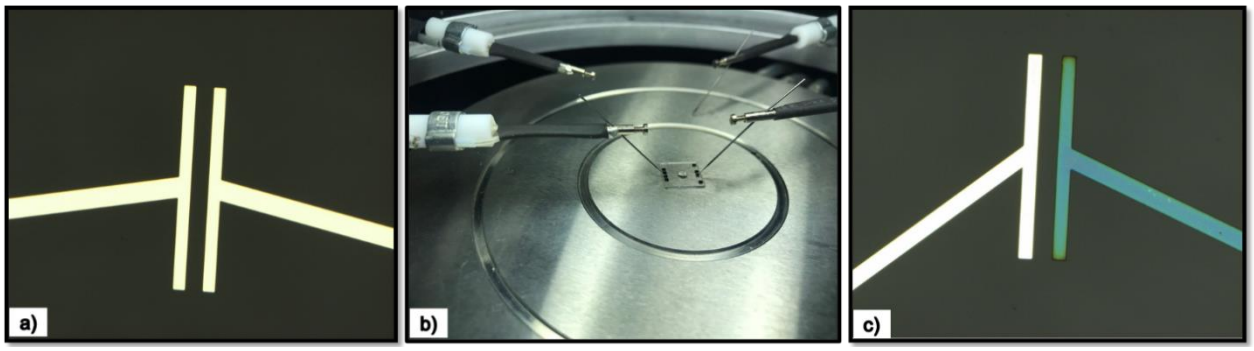

FIG. 2.10 a) Shows the quartz substrate with the two gold electrodes b) set up for electrodeposition of PEDOT: PSS c) microscope image after the material deposition.

2.6 Atomic force microscopy

Atomic Force Microscopy (AFM) is a powerful technique that allows to see and measure surface topographies at nanoscale level and it has been used for more than 25 years. [25] In AFM the measured quantity is the force between the tip and the sample that is measured. The AFM consists of a micro cantilever with a sharp tip that scans the surface. When the tip starts to scan the surface forces between the sample and the tip led to the deflection of the cantilever. This deflection is measured with a laser reflected from the top of the cantilever to a diode. A feedback circuit keeps a constant force between the tip and the sample. The corresponding changes to the z-position required to keep the distance tip-sample constant are the topography of the sample. In Fig. 2.11 is shown a schematic of an AFM.

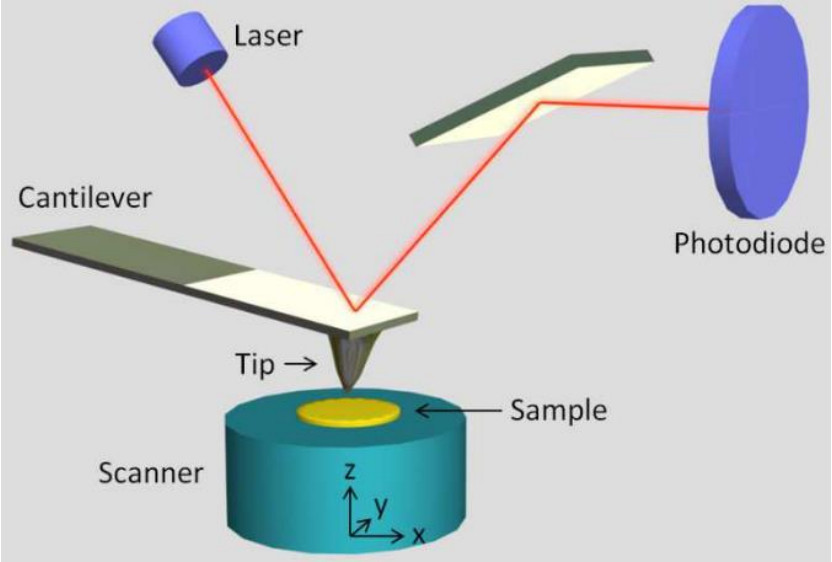

FIG. 2.11 Schematic illustration of the principles of AFM. The scanner is composed of three piezo components, which control the horizontal (x and y) and vertical (z) movement of the sample. Adapted from [26]

As we say before, the force between the tip and the sample can be measured in a static mode using the deflection of the cantilever likened to the deflection of a spring. Using the Hooke's law in which we have:

$$F = - kz \qquad (1)$$

where F is the force and z is the distance, we can easily determine the force if the stiffness of the cantilever spring *k* is known.

2.6.1 AFM operational modes

The interactions between the tip and the substrate can be described on the simplest features by referring to the Lennard-Jones potential acting between two atoms. The previous potential is described as a function of the distance by the eq.

$$U(r) = \left[-2\left(\frac{r_0}{r}\right)^6 + \left(\frac{r_0}{r}\right)^{12}\right] \qquad (2)$$

in which the first term describes the long-distance van-der-Waals attraction, and the second term describes the short-range repulsion due to the Pauli exclusion principle. The r_0 is the equilibrium distance between the atoms, where the energy is minimum while r, is the distance between the two atoms. In Fig. 2.12 is shown the different operating regimes of the AFM modes

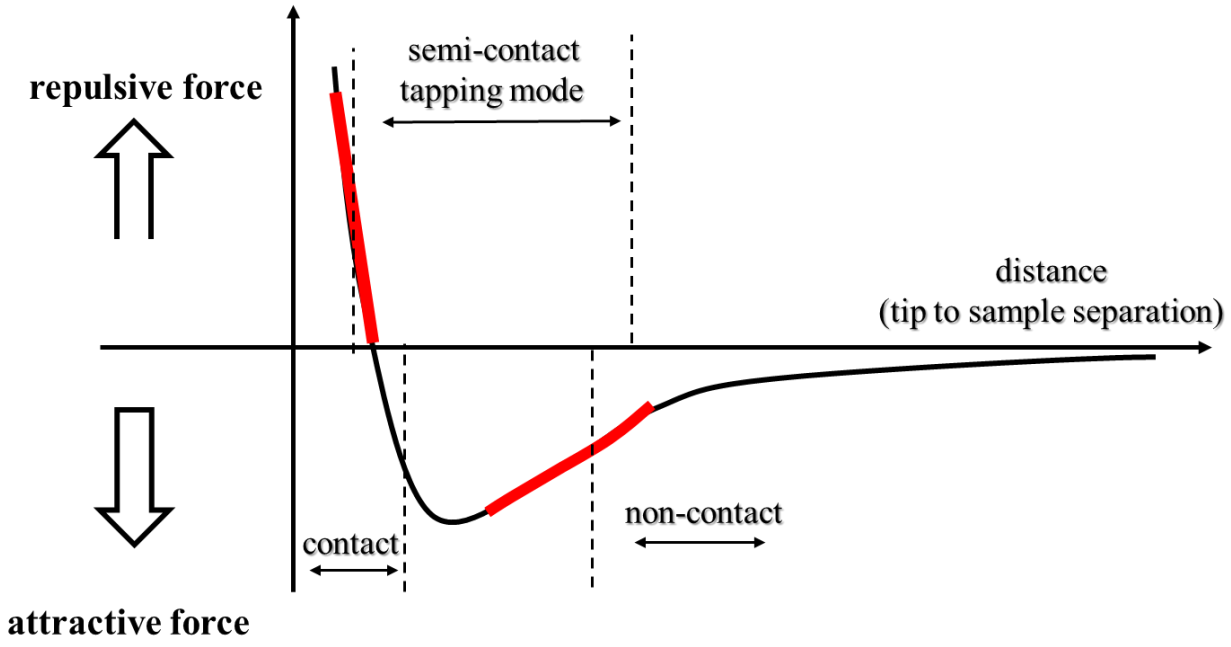

FIG. 2.12 Interatomic force vs. distance curve. Adapted from [27]

Among the different modes used in AFM, contact and tapping mode are the most relevant. Contact mode was the first mode developed for AFM: during this kind of experiments, the tip is close enough of the sample surface to be affected by a repulsive potential from the surface. If the substrate gets closer to the tip, the force applied on the cantilever will be higher and it will bend upward to compensate. If the substrate gets further from the tip, the force applied on the cantilever will decrease and it will relax in order to maintain the contact with the surface. This is the simplest mode, and the displacements of the laser are directly related to the topography of the substrate.

The disadvantage of this mode is that the force constantly applied on the substrate in can damage fragile samples such as polymers or biological samples.

To characterize fragile materials and to avoid tip contamination it is common to analyze the sample using the tapping mode or intermittent contact mode: in this mode the cantilever is oscillating near its resonance frequency. In this case the laser is constantly oscillating on the photodiode and it is the amplitude of the oscillation that are recorded. When the cantilever gets closer to the surface the repulsive wall damps the oscillations of the cantilever, when it gets further the oscillations increase. The variations of the amplitude of oscillation measured on the photodiode are representative of the topography of the substrate. Due to the short contact time and low forces applied on the sample it is possible to limit the destruction of soft samples and the contamination of the tip.

2.6.2 Bimodal AFM

After the dynamic mode which has a lot of advantages as well as variety of application due to the non-destructive nature of this mode, a new and innovative mode of AFM was investigated [28] The Bimodal AFM tries to overcome the conventional AFM limitations. With this multifrequency technique, quantitative and high spatial resolution results can be acquired. The principles idea of this method is based on the use of two driving forces for the excitation of the cantilever (Fig. 2.13). The excitation frequencies of the cantilever are tuned to match with, usually, the first and the second eigenmode of the cantilever. The output signals of the first mode (amplitude and frequency shift) are used to image the topography of the surface while, the output signals of the second mode (amplitude and frequency shift) are used to measure changes in the mechanical, [29] magnetic [30] and electrical properties. [31] Another advantage of this technique is that can be performed in air [29], in liquid [32] or in high vacuum [33] without influencing the acquired results.

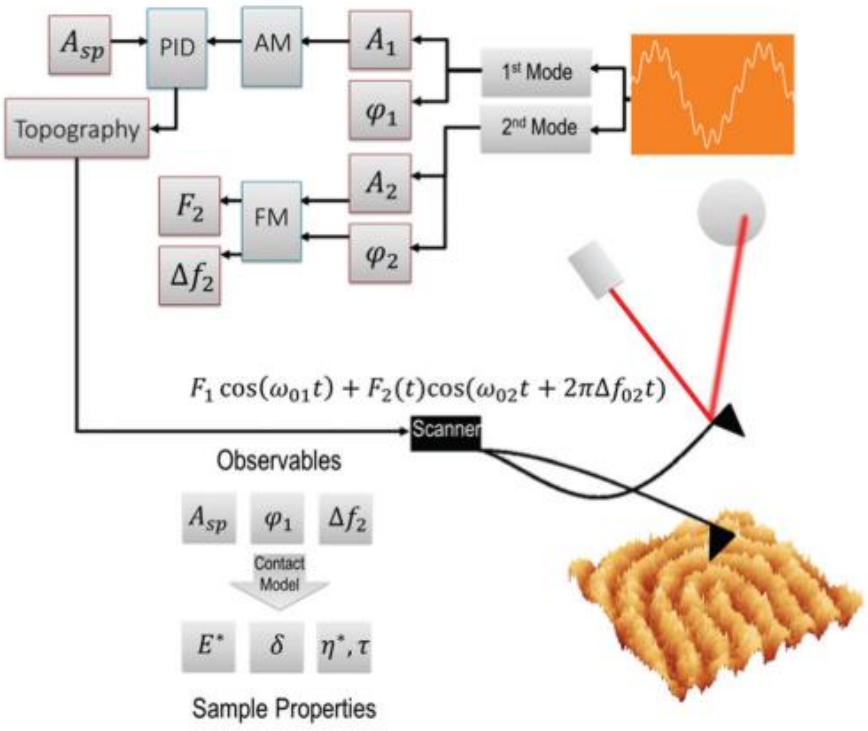

FIG. 2.13 Scheme of bimodal AM-FM for mapping viscoelastic properties. The microcantilever is driven simultaneously at the first two flexural resonances. Adapted from [34]

In order to acquire quantitative results from bimodal AFM, the relation virial V_i energy dissipation E_{diss} equations in the modes that are excited and, in our case, the first and the second. The analytical equation of the corresponding virial to the first eq. 2 and the second mode eq. 3 is written

$$V_1 = f_1 \int_0^{\frac{1}{f_1}} F_{ts}(t) z_1(t)\, dt = -(k_1 A_1 A_0 / 2Q_1) \cos \phi_1 \qquad (2)$$

and

$$V_2 = -k_2 A_2^2 \Delta f_2 / f_{02} \qquad (3)$$

Where F_{ts} is the tip sample interaction force, the k_i is the spring constant, A_0 is the set point amplitude of the first mode, A_1 and A_2 is the amplitude of the first and the second mode respectively, Q_1 is the quality factor of the cantilever, Δf_2 is the frequency shift of the second mode and f_{02} is the resonant frequency of the second mode. Combining these parameters, we can also calculate the maximum indentation through the equation which is shown in eq. 4

$$I^* = \frac{V_1}{V_2}\frac{A_2^2}{A_1} \tag{4}$$

Combined the two virials the Young's modulus can easily expressed through the eq. 5

$$E_{eff} = \sqrt{\frac{8A_1}{R_t}}\frac{V_2^2}{V_1}\frac{A_1}{A_2^4} \tag{5}$$

The extraction of the Young's modulus is a parameter which strongly depends on the shape of the cantilever. Previous studies have analytically described the model for commons axisymmetric AFM probes like paraboloid, cone, and cylinder. [35]

2.6.2 Cantilever Calibration

In order to ensure the accuracy of the nanomechanical data is important to have the accurate knowledge of the spring constant of the cantilever. There are different calibration models to calibrate the cantilever. [36–38] Usually, the spring constant of the cantilever is calibrated binging the tip in contact to a stiff sample, i.e., silicon, and recording its deflection. To avoid tip contamination and/ or broadening of the tip it is possible to use non-contact methods. To calibrate the first mode of the cantilever, the GetReal™ methods provided by Asylum Research, Oxford

Instruments [38]. For the calibration of the spring constant of the second mode, k_2, was obtained by assuming the stiffness-frequency power equation which gives

$$k_2 = k_1 \left(\frac{f_2}{f_1}\right)^{\zeta_2} \quad (6)$$

Where ζ corresponds to an experimental parameter and depends on the type of the cantilever. In literature there are studies that try to calculate this value for different shapes of cantilever. [38]

2.7 Surface analysis and extraction of growth parameters

As it was described in Chapter 3, morphological analysis took place for this thesis and its results were one of the important finding. The characterization and the quality control of the morphological parameters play an important role in the thin film science. Here, we are going to discuss in detail the extraction of the morphological parameters which are analyzed to the following Chapter. For all this analysis, we used Gwyddion and Origin Pro Software.

As it is known, when pentacene is grown on SiO_2 surfaces exhibits a self-affine morphology. [39–41] With the term self-affinity is defined that the morphology presents a similar behavior upon rescaling of their vertical or horizontal dimensions. The morphology of pentacene in SiO_2 looks like islands. [42] The dimensions, the type, and the steepness of the islands depend on different parameters such as the substrate the temperature and the rate of the deposition. [43,44] In Fig. 2.14 are shown the characteristics extracted directly from the topographic image. In cross section (red line) we can observe the commonly known “terraces” of pentacene. In the profile of the cross section (Fig. 2.14b) it is easily visible this growth in which every step corresponds to one layer. Another observable, which can easily extract and analyze is the height distribution (Fig. 2.14c). Taking into account the height analysis can help to understand the real height of the film. More specific, this distribution shows the maximum densities of the heights across the surface.

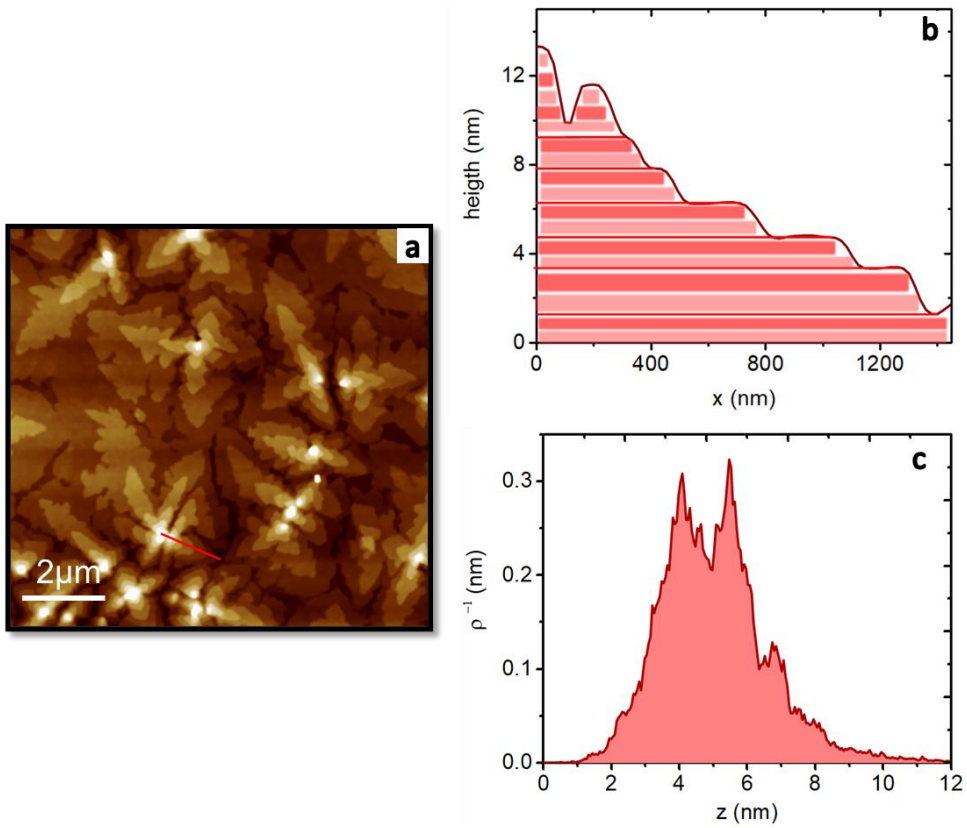

FIG. 2.14. a) topography of 7 nm pentacene thin film grown on SiO_2 at 80°C b) profile of the cross section (red line) c) height distribution of the pentacene thin film. White bar corresponds to 2 μm.

To acquire representative results, different topographic images from different samples and different areas from each sample need to be taken.

Another important parameter which has been studied during this thesis work is the correlation length (ξ). Correlation length corresponds to the typical distance over which the heights "know" each other- the characteristic distance in they are correlated. [42] The extraction of the correlation lengths was done through the Power Spectral Density (PSD), a mathematical tool that decomposes a surface into different spatial frequencies. Mathematically, the PSD if the Fourier transform of the autocorrelation function of the signal, which contained just the power and not the phase through different wavevectors. [45] The two-dimensional PSD of the Fourier Function of the topography h (x,y) it can be defined as

$$PSD(f_x, f_y) = \frac{1}{L^2}\left|\int_0^L \int_0^L e^{i2\pi f_x} e^{i2\pi f_y y}\left[h(x,y) - \bar{h}\right] dx\, dy\right|^2 \qquad (7)$$

where L is the image size, f_x and f_y are the frequencies along the axes x and y, and $\bar{h}$ is the mean height. The relevant spatial frequency range is between the inverse image size and the high/frequency limit $f_{max} = N/2L$ which corresponds to the Nyquist frequency and N is the number of the pixels per scan.

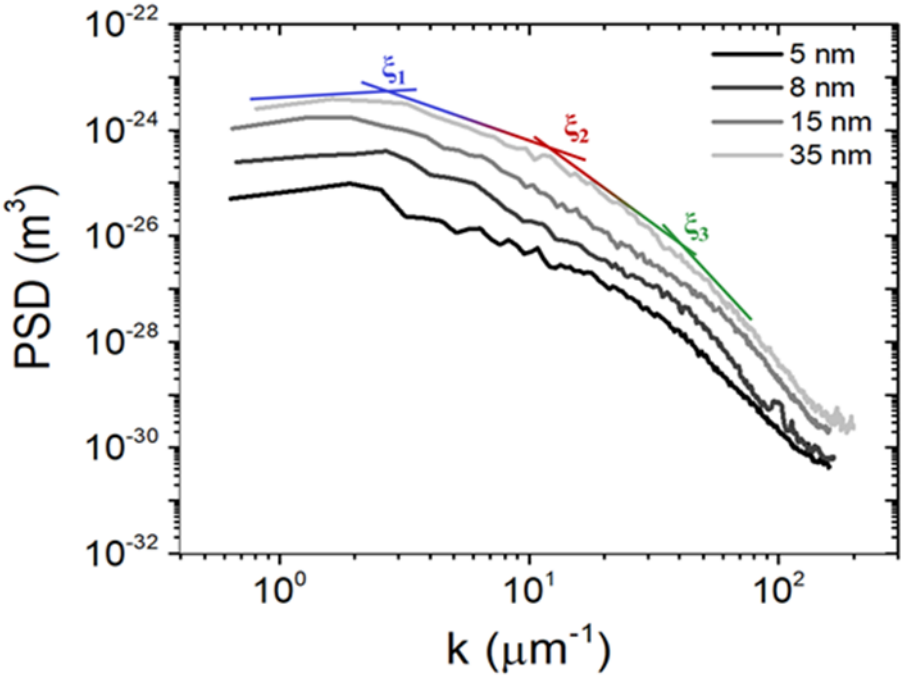

FIG. 2.15. Plot of the PSDs vs wave vector k for different thicknesses. ξ_1, ξ_2 and ξ_3 are the corresponding correlation lengths.

Fig. 2.15 a compares PSDs vs *k* at different thicknesses and explains the extraction procedure of the correlation lengths. Each PSD exhibits a plateau (white spectrum) at the lowest wavevectors, and a decaying portion that can be approximated by different linear segments in a double log plot.

In Fig 2.15 presents four different PSDs which corresponds to four different thickness of the pentacene film. As it is shown, three different changes on the slope show three different correlation length. Thus, each of these segments represents a power law decay of the PSD vs wavevector, each with a different exponent. The three correlation lengths can be identified from the intersections k_n (n=1, 2, 3) between two adjacent power law scaling segments. Once the intersection wavevector k_n has been quantified by equating the two linear fittings of the segments in the double-log scale, the corresponding correlation length is extracted as

$$\xi_n = \frac{2\pi}{k_n} \tag{8}$$

Another important morphological parameter extracted from AFM images is the roughness (σ): it is expressed as the standard deviation of the topographical height, and it is calculated from each AFM image as

$$\sigma = \left[\frac{1}{N}\sum_n [h_n - \langle h \rangle]^2\right]^{\frac{1}{2}} \tag{9}$$

where the sum runs on N x N pixels in the image, the h_n is the height at nth pixel and $\langle h \rangle$ is the mean. For general surfaces, the roughness increases as a power of time util a crossover time t_x, known as saturation time

$$w(L,t) \sim t^{\beta} \qquad [t \ll t_x] \tag{10}$$

The exponent β is called growth exponent with describes the time dependent dynamics of the roughening process. After the crossover time is reaches the roughness saturates w_{sat}. The saturation value increases with the increase of the system L and exhibits a power law behavior

$$w_{sat}(L) \sim L^{\alpha} \qquad [t \ll t_x] \tag{11}$$

Where α is called roughness exponent and is the second critical exponent that characterizes the roughness of the saturated interface. Moreover, the time in which the roughness is saturated also depends on a power law

$$t_x \sim L^z \tag{12}$$

Where *z* is called dynamic exponent and L is the system size. All the above parameters all helping tools in order to try to understand the evolution of the surface.

2.8 Electrical measurements set up

The electrical characterization of organic thin film transistors (OTFT) is a fundamental tool for investigating charge transport phenomena in organic materials. In Chapter 4, we will present and discuss the experiments and the electrical characterization both for OFETs and for EGOFETs. Here we are going to explain the electrical set up as well as the extraction of the electrical parameters. In Fig. 2.16 are depicted the connections during the measurements as well as the software measurement that allows the user to perform different types of electrical measurements such as current-voltage characteristics of a transistor, output characteristics, capacitive current measurement, pulse measurement, current as a function of time and voltage as a function of time.

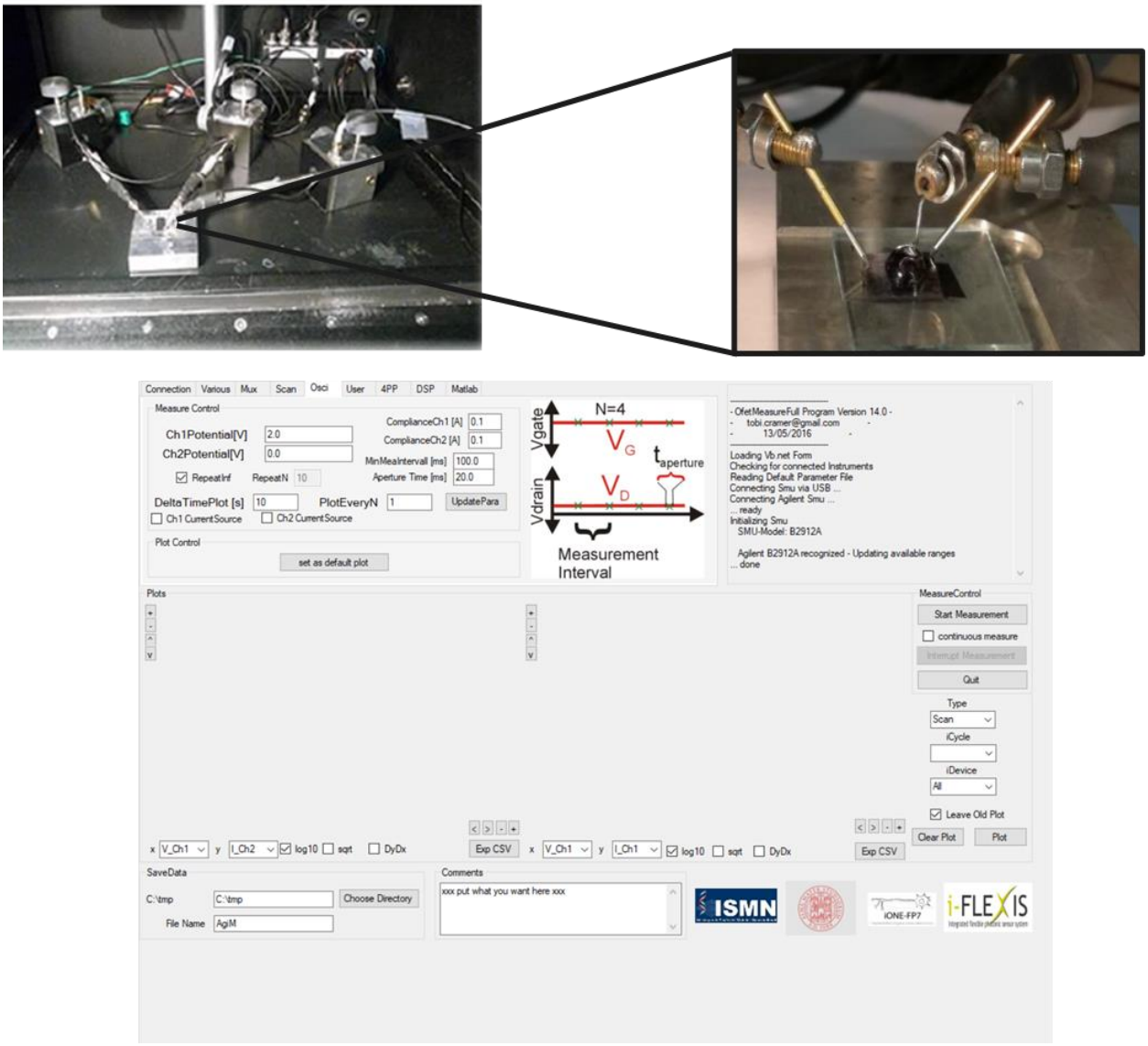

Fig. 2.16 Typical System Measurement Unit (SMU) for the electrical measurements. Software to control parameters and timing for the electrical measurement.

2.8.1 Electrical characterization and transport parameters extraction

The current-voltage characteristics, in linear and saturation regime, for the crystalline FETs can be described with the following equations:

In linear regime:

$$I_{DS} = \frac{w}{L} C_{ox} \mu \left[(V_{GS} - V_{th}) V_{DS} - \frac{V_{DS}^2}{2} \right] \qquad \text{when} \qquad V_{DS} < (V_{GS} - V_{th}) \qquad (13)$$

In saturation regime:

$$I_{DS} = \frac{w}{2L} C_{0x} \mu (V_{GS} - V_{th})^2 \qquad \text{when} \qquad V_{DS} \geq (V_{GS} - V_{th}) \qquad (14)$$

where C_{ox} is the capacitance of the dielectric per unit area (F/m^2), W and L are the width and length of the channel, respectively, μ is the charge carrier mobility, and V_{th} is the threshold voltage.

The drain source current I_{DS} depend on two independent voltages, the drain source voltage V_{DS} and the gate source voltage V_{GS}. For this reason, the current-voltage curves can be plotted in two different ways:

i) Transfer characteristics (Fig. 2.17 on the left)

ii) Output characteristics (Fig. 2.17 on the right)

In the first case, the drain source current is plotted as a function of the gate source voltage for a fixed drain source voltage and in the second case, a set of drain source current is plotted as a function of drain source voltage for a range of gate source biases. On typical graph with the characteristics is shown the Fig. 2.17.

The electrical characterization of an OFET is occurring by measuring the current that flows from the source to the drain (I_{DS}) when a voltage is applied to the gate (V_{GS}). For transfer characteristics, the source is normally grounded while a potential is applied to the drain. A plot of the current versus the gate voltage at a certain drain bias the *I-V* curve. There are two operation regimes depending on the potential applied to the drain, the linear regime and saturation regime.

Transconductance g_m is one of most critical and representative transistor parameters. More specifically, corresponds to the modulation of the drain current by the voltage between source and drain. It is given by

In linear regime:

$$g_m = \frac{w\mu C_i}{L} V_{DS} \tag{15}$$

In saturation regime:

$$g_m = \frac{W\mu C_i}{L} (V_{GS} - V_{th}) \tag{16}$$

when the W and L are the dimensions of the interdigitated electrodes, μ the mobility of the semiconductor, C_i the capacitance of the dielectric material and V_{DS}, and V_{GS}, the voltage between source and drain, source and gate, respectively. V_{th} is the threshold voltage.

The threshold voltage is defined as the gate voltage at which the device turns on, i.e., the onset of accumulation. The experimental V_{th} is the value in the transfer curve that divides the above-threshold regime (linear or saturation) from the sub-threshold regime. The value is obtained from the intersection of the linear fit in the plot (I_{DS} vs. V_{GS}) with the gate voltage axis as we can see in the Fig. 2.17.

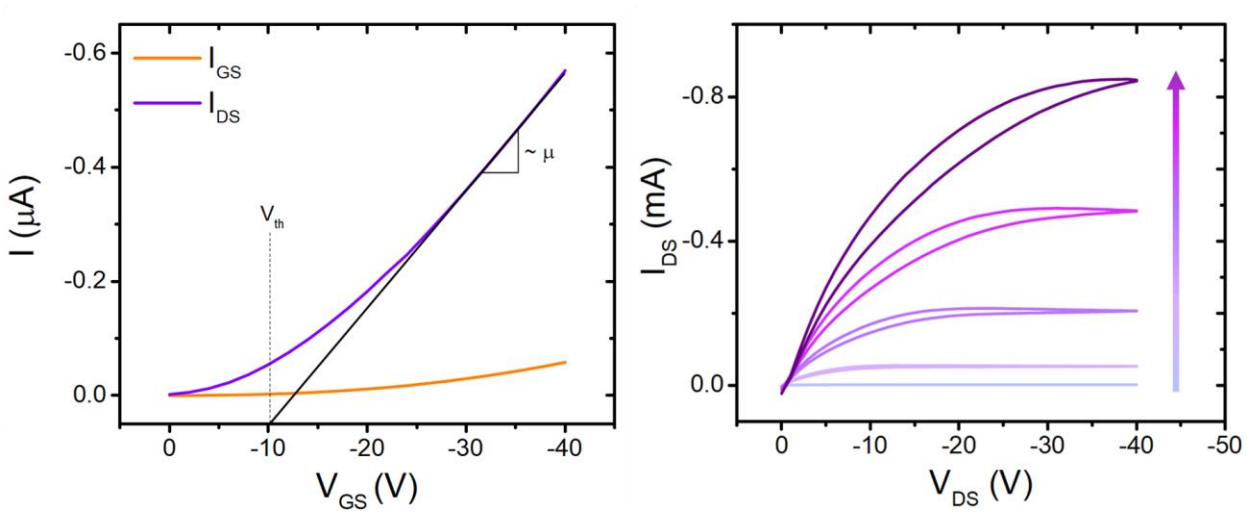

FIG. 2.17 Typical transfer characteristics obtained for pentacene based OFETs in linear regime (left). Typical output characteristics of pentacene OFET (right). The violet arrow corresponds to the increase of the gate voltage. The range of the V_{GS} is from 0 V to -40 V with a step of 10 V.

By analyzing the curve in Fig. 2.16 using eq. 13 for linear regime, we can extract the value of mobility of charge carriers μ and the threshold voltage V_{th}. Charge carrier mobility can be expressed in simple words as the speed of the majority of charge carriers (holes/electrons) transported in the semiconductor material. In p-type semiconductor like pentacene, the charge carriers are holes. The calculation of the mobility can be done by taking the slope of the linear part of I_{DS} vs V_{GS} when measured in linear regime. The output characteristics of an OFET is a measure of the source drain current as a function of the source drain voltage for different gate voltages. Fig. 2.17 (right) shows a typical output curve of an OFET.

Apart from the solid-state operation, measurements in electrolytic environment were performed. In Fig. 2.18 (left) a typical EGOFET transfer characteristic is shown. The extraction of the parameters was performed as analytical discussed before in the solid-state operation. On the right at Fig. 2.18 is presented an output characteristics of an EGOFET.

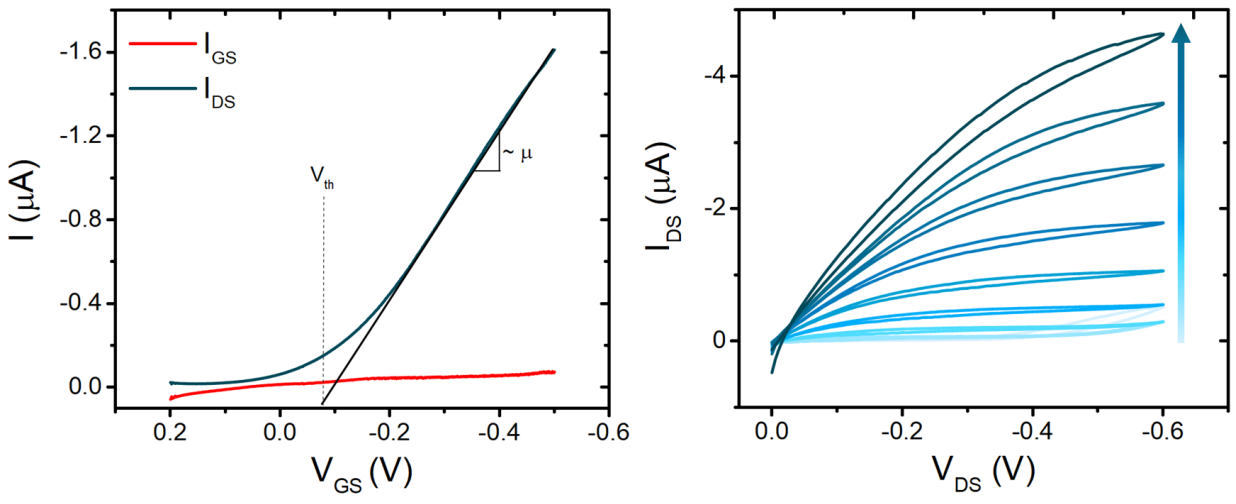

FIG. 2.18 Typical transfer characteristics obtained for pentacene based EGOFETs in linear regime (right). Typical output characteristics of pentacene EGOFET (left). The blue arrow corresponds to the increase of the gate voltage. The range of the V_{GS} is from 0.2 V to -0.6 with a step of 0.1.

The electrical parameters from solid state and from the electrolyte operation were extracted from 21 different thicknesses. In chapter 4 we are going to analyze in detail the influence of the thickness on the electrical properties.

2.9 References

[1] K. Oura, M. Katayama, A. V. Zotov, V. G. Lifshits, and A. A. Saranin, *Surface Science* (Springer Berlin Heidelberg, Berlin, Heidelberg, 2003).

[2] R. B. Campbell, J. M. Robertson, and J. Trotter, Acta Crystallogr. **14**, 705 (1961).

[3] K. Asadi, Y. Wu, F. Gholamrezaie, P. Rudolf, and P. W. M. Blom, Adv. Mater. **21**, 4109 (2009).

[4] H. U. Khan, M. E. Roberts, W. Knoll, and Z. Bao, Chem. Mater. **23**, 1946 (2011).

[5] A. A. Günther, J. Widmer, D. Kasemann, and K. Leo, Appl. Phys. Lett. **106**, 233301 (2015).

[6] T. Cramer, A. Kyndiah, M. Murgia, F. Leonardi, S. Casalini, and F. Biscarini, Appl. Phys. Lett. **100**, (2012).

[7] M. Berto, S. Casalini, M. Di Lauro, S. L. Marasso, M. Cocuzza, D. Perrone, M. Pinti, A. Cossarizza, C. F. Pirri, D. T. Simon, M. Berggren, F. Zerbetto, C. A. Bortolotti, and F. Biscarini, Anal. Chem. **88**, 12330 (2016).

[8] M. Göllner, M. Huth, and B. Nickel, Adv. Mater. **22**, 4350 (2010).

[9] L. Torsi, M. Magliulo, K. Manoli, and G. Palazzo, Chem. Soc. Rev. **42**, 8612 (2013).

[10] C. D. Dimitrakopoulos, A. R. Brown, and A. Pomp, J. Appl. Phys. **80**, 2501 (1996).

[11] F. Louwet, L. Groenendaal, J. Dhaen, J. Manca, J. Van Luppen, E. Verdonck, and L. Leenders, Synth. Met. **135**–**136**, 115 (2003).

[12] L. Basiricò, P. Cosseddu, B. Fraboni, and A. Bonfiglio, Thin Solid Films **520**, 1291 (2011).

[13] D. J. Lipomi, J. A. Lee, M. Vosgueritchian, B. C. K. Tee, J. A. Bolander, and Z. Bao, Chem. Mater. **24**, 373 (2012).

[14] D.-S. Leem, P. H. Wöbkenberg, J. Huang, T. D. Anthopoulos, D. D. C. Bradley, and J. C. DeMello, Org. Electron. **11**, 1307 (2010).

[15] P. Åsberg and O. Inganäs, Biosens. Bioelectron. **19**, 199 (2003).

[16] A. Blau, A. Murr, S. Wolff, E. Sernagor, P. Medini, G. Iurilli, C. Ziegler, and F. Benfenati, Biomaterials **32**, 1778 (2011).

[17] P. Lin and F. Yan, Adv. Mater. **24**, 34 (2012).

[18] N. Y. Shim, D. Bernards, D. Macaya, J. DeFranco, M. Nikolou, R. Owens, and G. Malliaras, Sensors **9**, 9896 (2009).

[19] H. Tang, P. Lin, H. L. W. Chan, and F. Yan, Biosens. Bioelectron. **26**, 4559 (2011).

[20] M. Sessolo, J. Rivnay, E. Bandiello, G. Malliaras, and H. J. Bolink, Adv. Mater. **26**, 4803 (2014).

[21] F. Cicoira, M. Sessolo, O. Yaghmazadeh, J. A. DeFranco, S. Y. Yang, and G. Malliaras, Adv. Mater. **22**, 1012 (2010).

[22] S. Rattan, P. Singhal, and A. L. Verma, Polym. Eng. Sci. **53**, 2045 (2013).

[23] R. Matsubara, Y. Sakai, T. Nomura, M. Sakai, K. Kudo, Y. Majima, D. Knipp, and M. Nakamura, J. Appl. Phys. **118**, (2015).

[24] S. R. Forrest, Chem. Rev. **97**, 1793 (1997).

[25] G. Binnig, C. F. Quate, and C. Gerber, Phys. Rev. Lett. **56**, 930 (1986).

[26] G. Zeng, Y. Duan, F. Besenbacher, and M. Dong, in *At. Force Microsc. Investig. into Biol. - From Cell to Protein* (InTech, 2012).

[27] R. Howland, L. Benatar, and C. H. S. P. M. T. Echniques, BMJ **2**, 490 (1892).

[28] R. García and E. T. Herruzo, Nat. Nanotechnol. **7**, 217 (2012).

[29] N. F. Martinez, S. Patil, J. R. Lozano, and R. García, Appl. Phys. Lett. **89**, (2006).

[30] J. W. Li, J. P. Cleveland, and R. Proksch, Appl. Phys. Lett. **94**, (2009).

[31] R. W. Stark, N. Naujoks, and A. Stemmer, Nanotechnology **18**, 065502 (2007).

[32] N. F. Martínez, J. R. Lozano, E. T. Herruzo, F. Garcia, C. Richter, T. Sulzbach, and R. García, Nanotechnology **19**, (2008).

[33] S. Kawai, T. Glatzel, S. Koch, B. Such, A. Baratoff, and E. Meyer, Phys. Rev. Lett. **103**, 1 (2009).

[34] S. Benaglia, C. A. Amo, and R. García, Nanoscale **11**, 15289 (2019).

[35] S. Benaglia, V. G. Gisbert, A. P. Perrino, C. A. Amo, and R. García, Nat. Protoc. **13**, 2890 (2018).

[36] J. E. Sader, I. Larson, P. Mulvaney, and L. R. White, Rev. Sci. Instrum. **66**, 3789 (1995).

[37] J. P. Cleveland, S. Manne, D. Bocek, and P. K. Hansma, Rev. Sci. Instrum. **64**, 403 (1993).

[38] A. Labuda, M. Kocun, M. Lysy, T. Walsh, J. Meinhold, T. Proksch, W. Meinhold, C. Anderson, and R. Proksch, Rev. Sci. Instrum. **87**, (2016).

[39] I. Tonazzini, E. Bystrenova, B. Chelli, P. Greco, P. Stoliar, A. Calò, A. N. Lazar, F. Borgatti, P. D'Angelo, C. Martini, and F. Biscarini, Biophys. J. **98**, 2804 (2010).

[40] A. Brillante, I. Bilotti, R. G. Della Valle, E. Venuti, A. Girlando, M. Masino, F. Liscio, S. Milita, C. Albonetti, P. D'angelo, A. Shehu, and F. Biscarini, Phys. Rev. B **85**, 195308 (2012).

[41] R. Ruiz, A. C. Mayer, G. Malliaras, B. Nickel, G. Scoles, A. Kazimirov, H. Kim, R. L. Headrick, and Z. Islam, Appl. Phys. Lett. **85**, 4926 (2004).

[42] A.-L. Barabási and H. E. Stanley, in *Fractal Concepts Surf. Growth* (Cambridge University Press, 1995), pp. 1–18.

[43] F. Biscarini, P. Samorí, A. Lauria, P. Ostoja, R. Zamboni, C. Taliani, P. Viville, R. Lazzaroni, and J. l. Brédas, Thin Solid Films **284**–**285**, 439 (1996).

[44] F. Dinelli, M. Murgia, P. Levy, M. Cavallini, F. Biscarini, and D. M. de Leeuw, Phys. Rev. Lett. **92**, 116802 (2004).

[45] A. Duparré, J. Ferre-Borrull, S. Gliech, G. Notni, J. Steinert, and J. M. Bennett, Appl. Opt. **41**, 154 (2002).

Chapter 3

A new growth mode of pentacene thin films

"In this chapter we study the morphology of high-vacuum sublimed pentacene thin films by means of Atomic Force Microscopy. A new experimental finding in thin film growth is reported: morphological parameters exhibit oscillations superimposed to the monotonic self-affine power law trend across the whole thickness range. The observed oscillatory behavior is different from the one commonly observed in the layer-by-layer mode before the transition to self-affine island occurs. Here the oscillations repeat themselves at all thicknesses. This result evidences the analogy between this new growth mode and wetting/dewetting transitions that repeat with an increasingly larger period as the film grows."

3.1 Introduction

The efficiency and performance of optoelectronic devices based on organic semiconductors (OSCs) thin films depend on the control of the thin film multiscale morphology. [1,2] The technological quest provides a motivation for understanding the mechanistic aspects of organic thin film nucleation and growth leading to morphology. Therefore, a precise control of the molecular orientation and the molecular packing of pentacene thin films is extremely important for thin film OFETs. [3] The multiscale structure of organic thin films is correlated with the one of the first monolayers. Thus, the interactions among the organic molecules and their interaction with the substrate surface determine to a large extent the emerging morphology. [4]

Among the techniques for thin film deposition, the sublimation of molecular semiconductors in ultra-high vacuum, also termed Organic Molecular Beam Deposition (OMBD), is prototypical for studying the interplay of kinetic and thermodynamic factors in a non-equilibrium growth process. [5] In OMBD a hot molecular flux impinges on a colder surface. [6] Because equilibrium conditions are not attained, the impinging molecules do not immediately thermalize on the surface, and there is a time for them to move on the surface and explore the surface potential landscape. Small variations of experimental parameters, such as deposited mass/thickness h, flow/deposition rate r, substrate temperature T during deposition, as well as chemical functionalization of the interfaces and the molecular structure of the semiconductor (that control diffusivity and surface energy), may lead to crossovers of the controlling mechanisms, thus leading to a variety of morphological features and instabilities that propagate across the whole thin film. [7–10]

It was observed already several years back that molecular thin films grown in OMBD exhibit a “universal” transition from layer-by-layer growth, typically on the thickness scale of one to three monolayers (a few nm), to island growth which manifests itself as the stacking of molecular layers. Such a transition, that resembles the Stranski-Krastanov 2D-3D transition, cannot be described with sole thermodynamic arguments in terms of stress release by nucleation of disordered 3D aggregates due to the lattice mismatch. Indeed, differently from epitaxy, the technological substrates of organic electronics are (usually) amorphous as silica, glass, or plastic foils. In

addition, the thin film deposition is a strongly out of equilibrium process, which undergoes kinetic control.

A distinctive property that allows one to experimentally monitor the layer-by-layer to island growth transition is *rms* roughness vs deposition time/mass/thickness of the thin film. Roughness is defined as the root-mean square fluctuation of the surface topography, and its scaling behavior with the time and spatial lengthscales is extracted from several techniques, like X-ray reflectivity, laser light scattering vs wavevector/ spatial frequency, contact angle measurements, AFM. Roughness is a robust descriptor of surface morphology: it quantifies the second moment of the height distribution. Its length- and time scaling behavior provides insights on the universality class of growth, thus hinting to the underlying mechanism controlling the morphology. In an ideal layer-by-layer growth, the rms roughness oscillates according to:

$$\sigma = \sqrt{\langle h^2 \rangle - \langle h \rangle^2} = h_0\{[2n(\Theta) - 1 - \Theta]\Theta\}^{1/2} \qquad (1)$$

Where h0 is the thickness of the forming layer in layer-by-layer growth (viz. could be 1.5 nm for a pentacene monolayer, else 3 nm for two stacked pentacene monolayers). The demonstration for the distribution of the roughness in an ideal layer-by-layer growth is detailed in section 2.7.

Wetting/dewetting transitions are invoked in the equilibrium and dynamic behavior of fluid films, also viscous ones, [11] but are less common in conjugated organic thin films. They are however translated in the surface science community, especially in thin metal film growth, as synonym of layer-by-layer to island growth, meaning the transition from a 2D to a 3D growth mode. [12] Wetting/dewetting was originally applied to fluid layers, then extended to viscous and solid amorphous films. The group at UNIMORE (formerly at CNR ISMN Bologna) proposed to exploit and characterize wetting/dewetting transitions to form conjugated nanostructures in technological applications. [13]

The peculiarity of organic thin films here is that films are solid and possess a high degree of crystal order both within each molecular plane and in the stacking of multiple molecular planes. The order

parameter seems to be maintained with continuity across the roughening transition, [6,14,15] whereas transitions from thin film to bulk polymorphs [16,17] are observed at larger thicknesses. [18]

In this chapter, a comparative study on the evolution of the roughness (σ) on pentacene thin films was carried out. Pentacene thin films of different thicknesses were obtained on SiO_2/Si substrates by high vacuum sublimation, with a control of thickness lesser than 0.5 monolayers (about 0.5 nm). Morphological characterization by Atomic Force Microscopy (AFM) was performed to analyze the film morphology. Spectral analysis allowed us to investigate the correlations of the features from the image through the surface. Fitting of experimental data with some new phenomenological function based on an ad-hoc designed wavelet allows us to establish a framework to interpret this peculiar new mode of growth and the film thickness.

3.2 Experimental part

This experiment was carried out in a home-designed and built ultra-high vacuum chamber described in the previous Chapter 2. (Section 2.3). [19] The test patterns were cleaned by following a standardized protocol as in details discussed in Section 2.1.1.

For the experiment on bare SiO_2, no chemical treatment was carried out after the cleaning procedure, while for the HMDS-treated substrate, just after cleaning the test patterns, the oxide surface was functionalized with hexamethyldisilazane (HMDS) by thermal evaporation. (Section 2.1.4)

Pentacene was deposited by high vacuum sublimation with a rate of 0.1 Å/s on the test pattern with transistor structures. The substrate temperature was kept at 80^o C. Twenty-one different thicknesses of pentacene thin films shown at Table 3.1 were prepared. For the analysis forty-two pentacene samples were prepared i.e., two samples for each thickness.

Table 3.1. Thickness of pentacene thin films at 80°C.

Nº	1	2	3	4	5	6	7	8	9	10	11	12	13	14	15	16	17	18	19	20	21
Thickness (nm)	3	4	5	6	6.5	7	7.5	8	8.5	9	10	11	12	13	15	17	19	20	25	30	35

Another batch of pentacene thin films was prepared through vacuum sublimation keeping the same rate of 0.1 Å/s. The substrate temperature was kept at 25-27^{o} C (room temperature). The different film thicknesses are represented to Table 3.2.

Table 3.2. Devices on pentacene thin films at 25°C.

Nº	1	2	3	4	5	6	7	8
Thickness (nm)	1	3	5	10	20	40	50	100

Morphological characterization was performed by Atomic Force Microscopy (AFM) on the pentacene films grown on SiO_2 was carried out ex situ. The AFM images were statistically analyzed in terms of scaling behavior of the surface root-mean-square (*rms*) roughness σ with respect to the length scale of the observation L. For this study two different samples for each thickness were prepared. For the morphological analysis four AFM topographic images from four different regions were taken from all the devices. The relevant properties were averaged over these two samples. Fig. 3.1 shows the topography images obtained by AFM at all the thicknesses that are relevant for this study.

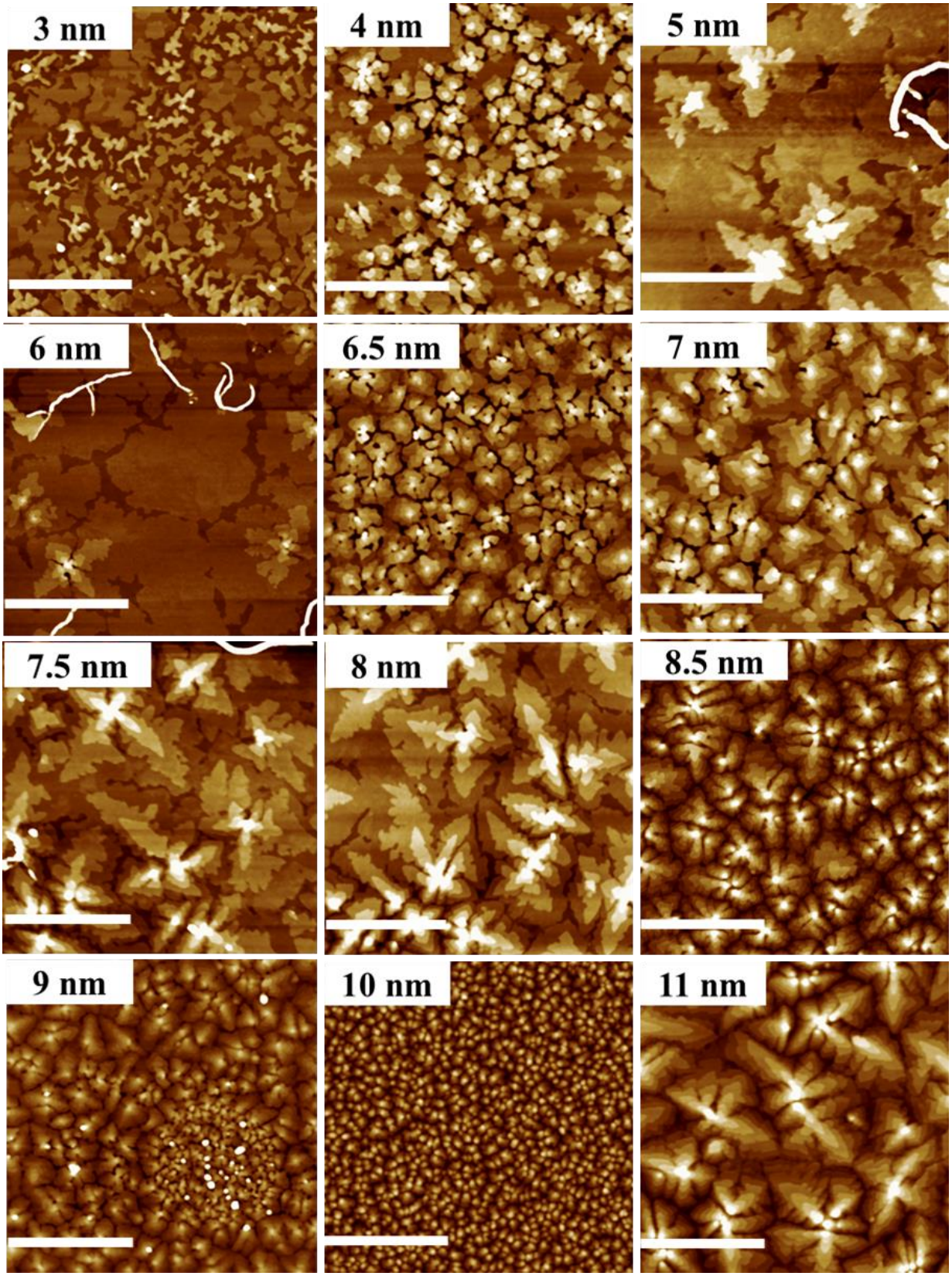
3 nm
4 nm
5 nm
6 nm
6.5 nm
7 nm
7.5 nm
8 nm
8.5 nm
9 nm
10 nm
11 nm

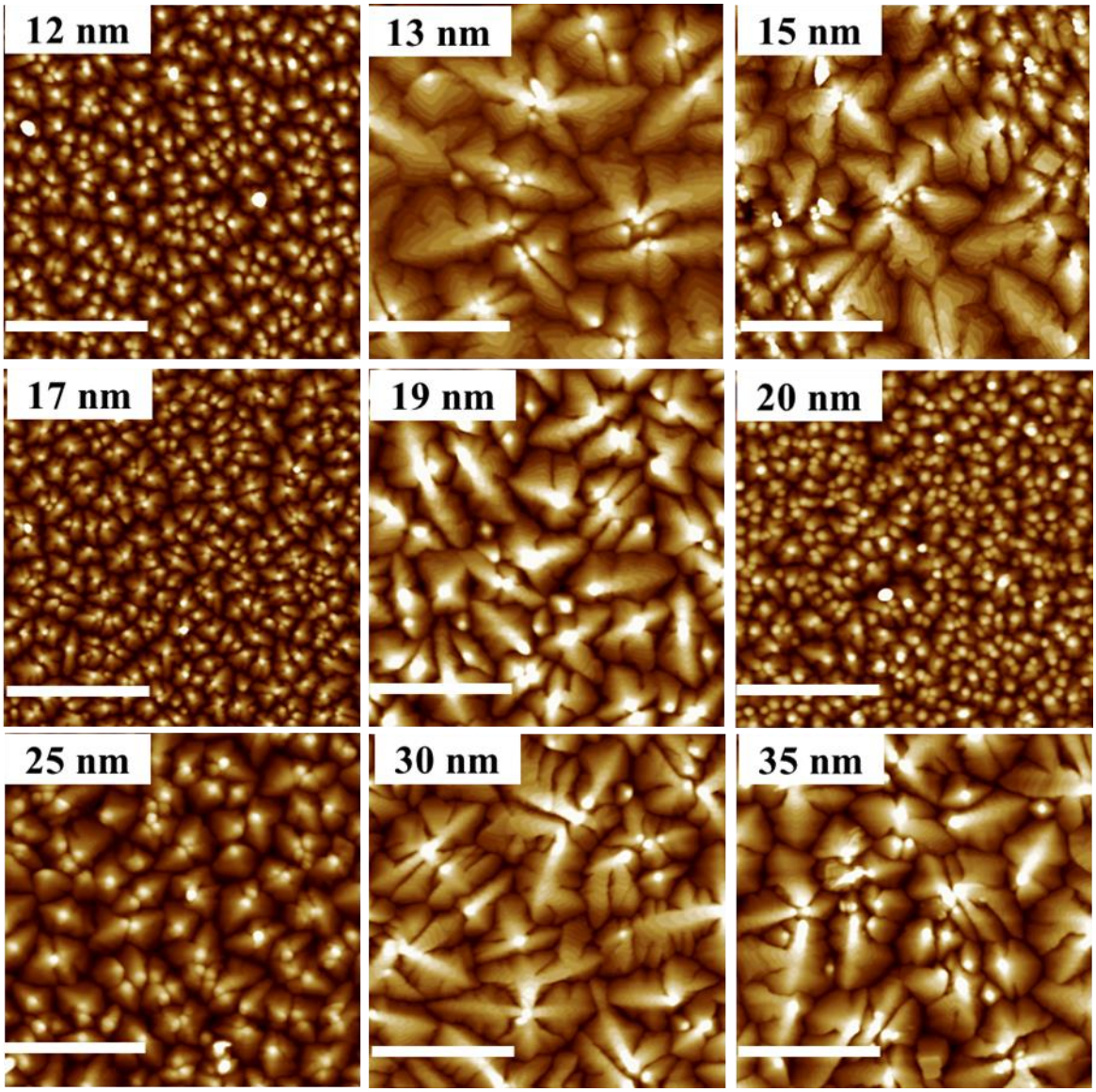

FIG. 3.1. Topographic images of pentacene films of different thickness grown on SiO_2 at 80°C. Rulers (white horizontal bar) are 2 μm long.

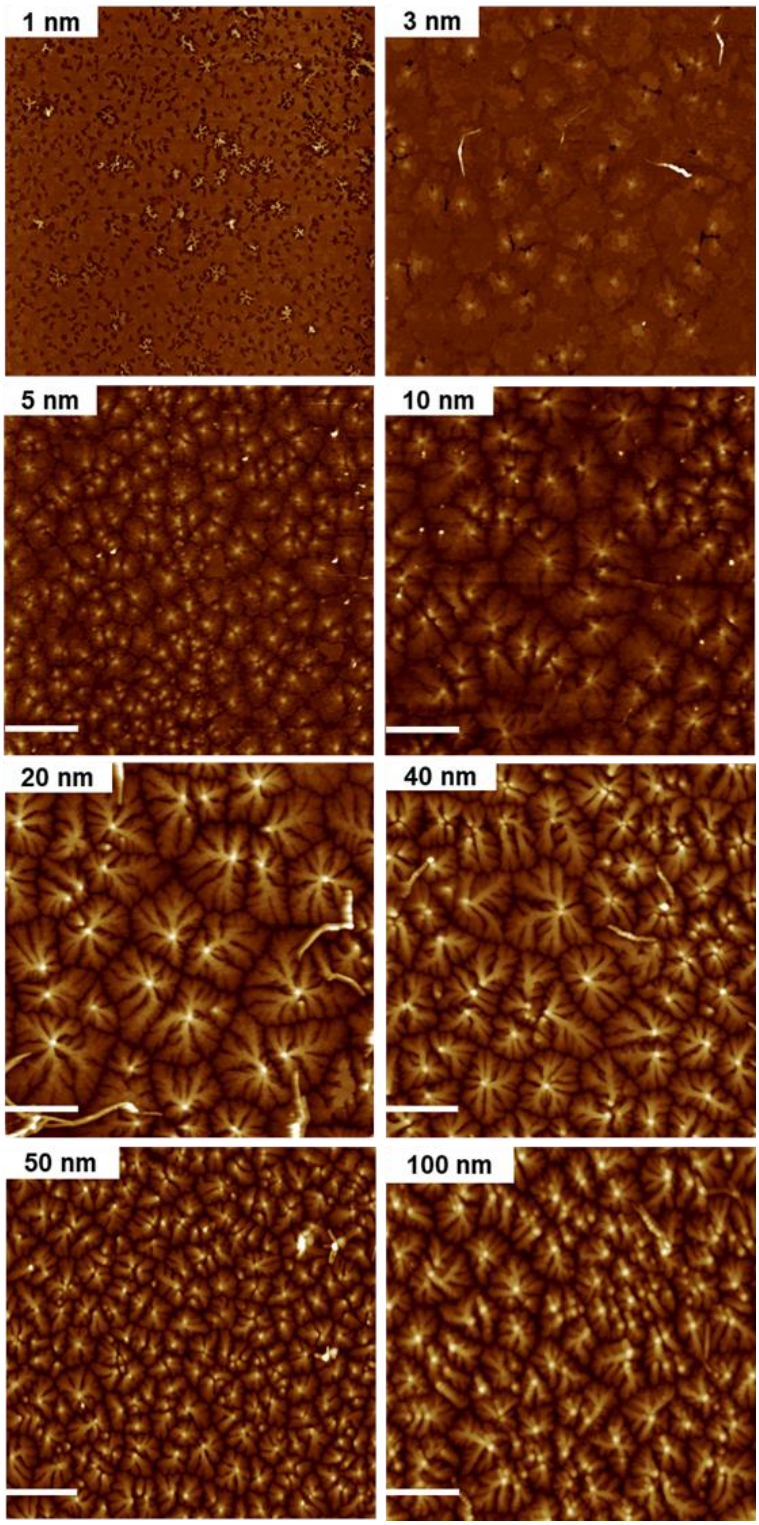

FIG. 3.2. Topographic images of pentacene films of different thickness grown on SiO_2 at room temperature. Rulers (white horizontal bar) are 2 μm long.

3.3 Result

Pentacene thin films grown on SiO_2 substrate at 80 °C (Fig. 3.1) are described in detail along with their height histograms in the figures 3.4-3.9 below. The morphology of pentacene thin films consists of terraced islands that nucleate and grow on the substrate (at small thickness/low coverage) or the otherwise molecularly smooth slab made of a few complete monolayers. The surface roughness increases with increasing thickness as the result of the stacking of progressively smaller terraces to form islands. The islands can be regarded, despite their intrinsic crystal order, as three-dimensional objects. The larger is the number of stacked monolayers the more three-D the islands are.

The emergence of terraced islands can be explained with simple surface science arguments in terms of a net uphill molecular flux from the bottom-most layers, that leads to roughening [5,8,20,21]. However, we point out that across the whole thickness range the noticeable feature is that the characteristic size of the terraced islands of the growing films alternates from large to small islands. This oscillation repeats itself vs increasing thickness several times in the thickness range explored.

We first discuss pentacene thin films grown on SiO_2 substrate at room temperature (Fig. 3.2) exhibits a relatively homogeneous morphology. Looking the topographic images, a small change from smaller to larger islands is observed in comparison with Fig. 3.1 in which the alternate morphologies with either large or small islands is evident. In Fig. 3.1 the bouncing morphology is repeated as the thickness of the pentacene thin films increases, leading us to recognize this as a new growth mode. On the other hand, the morphology of thin films grown at room temperature is more homogeneous, however the alternation of pentacene island size still exists but is less evident. Thus, we carried out the statistical analysis of the morphology in terms of correlation lengths ξ_1 and ξ_2 and roughness σ vs thickness h.

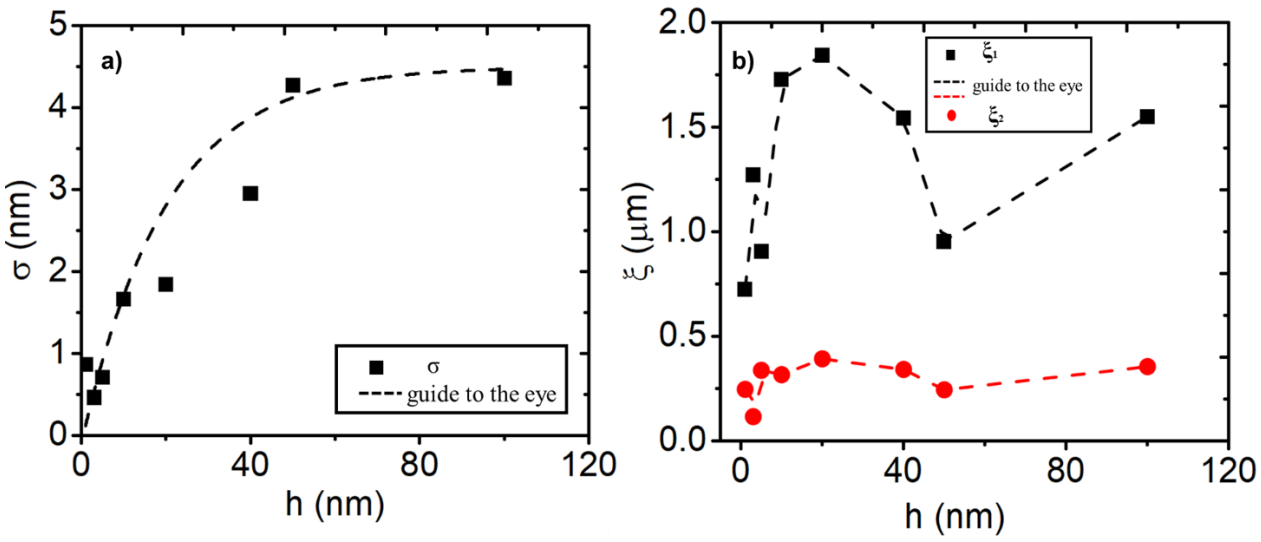

FIG. 3.3. *Evolution of roughness versus thickness for pentacene films grown at room temperature. The black dashed line serves as guide to the eye. Correlation lengths vs thickness: ξ_1 (black) and (b) ξ_2 (red). The dashed lines are data interpolation ξ_1 and ξ_2 and serves as guide to the eye.*

In Fig. 3.3a the behavior of the roughness vs thickness for pentacene thin films grown at room temperature is shown. At first monolayers the oscillations of the roughness of the films growing the layer-by-layer are not resolved. As the thickness increases the roughness increases until it attains a plateau. This behavior of the roughness is in line with studies which showed that at large thicknesses the roughness saturates. [4] In Fig. 3.3b the correlation lengths at the low thicknesses increases vs thickness which implies that during the growth of the first layers there is a low density of pentacene islands on the growing layers. [22]

We now go into detail into the discussion of the results from Fig. 3.1. We first comment the morphology of 3 nm (Fig. 3.4a) and 5 nm (Fig. 3.4b) pentacene thin films by means of AFM images with corresponding height histograms shown in Fig. 3.4c and Fig. 3.4d. At the smaller thickness 3 nm (Fig. 3.4a), a mixed growth is observed, where 2D islands coexist with multilayer 3D layers. The histogram in Fig. 3.4c reveals two peaked distributions and a large-height tail with some ripples. The first peak is ascribed to the substrate (dark color in Fig. 3.4a) which is a dominant component of the image. The second smaller peak is 1.5 nm above and indicates a single monolayer. The third peak is the dominant pentacene layer, whose thickness is two monolayers,

and is sized by the fourth peak corresponding to the third monolayer. The tail of the distribution accounts for monolayers above 3. Hence, the morphology results from the coexistence of mostly one- and three-layer islands. This evidence suggests that the 3 nm film in Fig. 3.4a dewetted causing the exposure of the substrate and piling up from one monolayer into three-layer islands. Although the film does not appear continuous, there are, however, connected percolation pathways across the channel since the corresponding transistor gives a current response as in the section 4.3.

At 5 nm (Fig. 3.4b), the first two monolayers have completed the coverage by closing, and large layered islands grow above the almost complete first bilayer. The substrate is barely visible, as a very few pixels may be ascribed to it, thus giving rise to the shoulder in Fig. 3.4b at the lower data. The large peak of the distribution reflects the large coverage of the first bilayer, and overall, the distribution is very narrow. Next to the large peak, at the right, we can observe the formation of the next monolayer as well as a small shoulder which corresponds to the upper layer and we can easily distinguish at the topography (Fig. 3.4b)

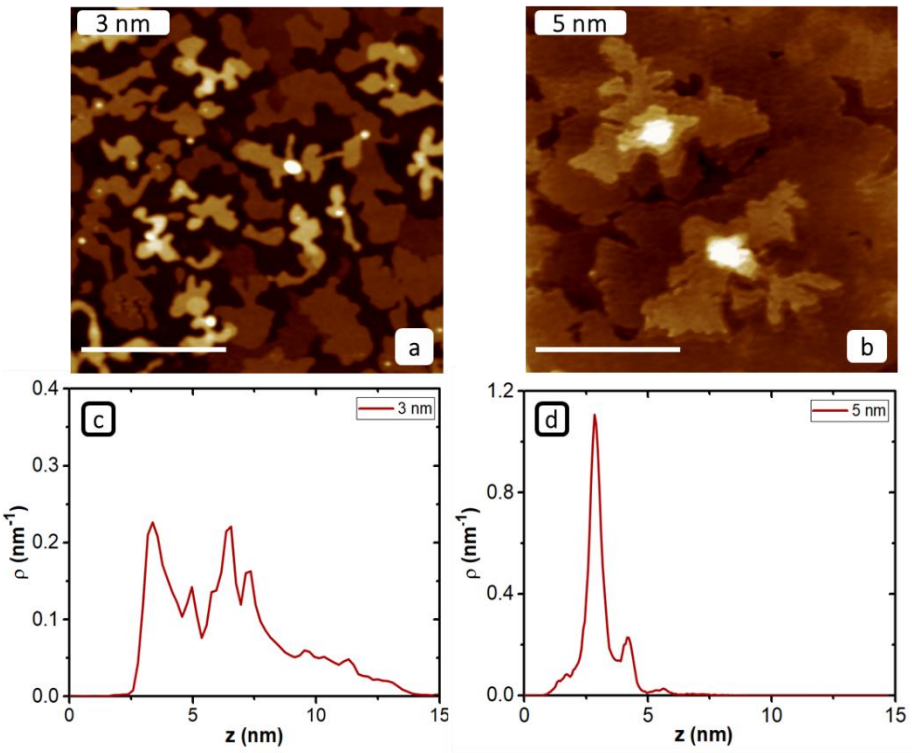

FIG. 3.4. 5 µm x 5 µm AFM topographic images of pentacene thin films with different thickness deposited on SiO_2/Si wafers at 80°C. Rulers (white horizontal bar) are 2 µm long. Topography ranges from 0 nm (black) to (a) 12.0; (b) 6.0 nm (white) (c) and (d) Histograms of topographic images showing the height distribution of pentacene thin films

In all images from 5 to 8 nm and beyond, the islands exhibit a terraced morphology, implying that the film grows by stacking layers. At 6.5 nm (Fig. 3.5a) the topmost layered islands are small, whereas at 8 nm (Fig. 3.5b) they grow larger. The height distributions in Figs. 3.5c and 3.5d reveal a "comb" structure superimposed to a "normal" distribution, typical of stacked monolayers. The height difference between the first two peaks is 2.8 nm, revealing the completion of the first bilayer. Other height differences are on the order of 1.5 nm, confirming that they are molecular monolayers. The films from 5 nm to 8 nm exhibit an oscillation back and forth of

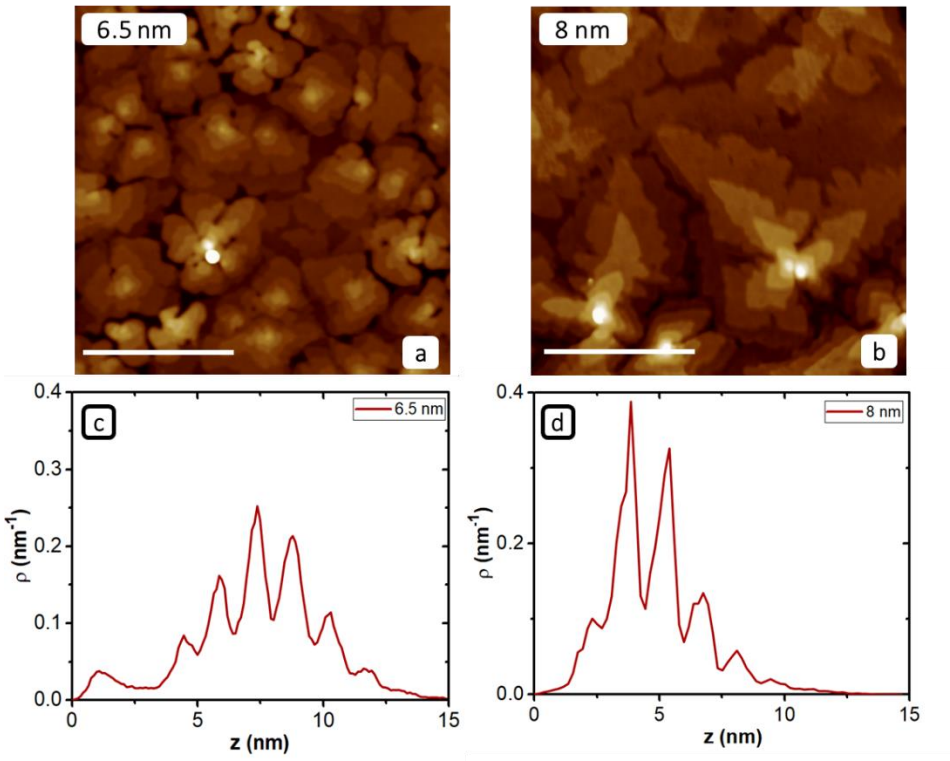

FIG. 3.5. 5 μm x 5 μm topographic images of pentacene thin films with different thickness deposited on SiO_2/Si wafers at 80°C. Rulers (white horizontal bar) are 2 μm long. Topography ranges from 0 nm (black) to (a) 20.0; (b) 20.0 nm; (white)(c) and (d) Histograms of topographic images showing the height distribution of pentacene thin films.

the mean height (center of the distribution). At 12 nm (Fig. 3.6a) the coverage of the substrate is complete. The islands formed are steeper than those at 8 nm (Fig. 3.6b) and closer between them. In other words, the terraces seem to fade away in the images. Their histogram (Fig. 3.6c) reveals a high density of small islands distributed on the surface. At Fig. 3.6b a different morphology could easily be observed. Looking at the topography, larger islands with big terraces have been formed and in agreement with the histogram in Fig. 3.6d which shows a distribution of larger islands through the surface, reveals a change in the type of growth.

This characteristic and unintuitive change of morphology is also evident by inspecting the morphology of the films whose thicknesses range from 12 nm (Fig. 3.6a) to 35 nm (Fig. 3.10a), and the corresponding histograms in Fig. 3.6c to 3.8d. There, from Fig. 3.6c to 3.9d, the multi peaked structure is less evident, albeit terraces can be appreciated by inspection in all the images from Fig. 3.4 to Fig. 3.9. In histograms above the envelope from Fig. 3.6c to Fig. 3.9d there is a gaussian distribution of the heights.

In Fig. 3.7a and 3.7b the same phenomenon can be observed. At 17 nm (Fig. 3.7a) smaller and steeper islands are formed with respect to 19 nm (Fig. 3.7b) in which larger and more distant islands we can see. Looking at their histograms in Fig. 3.7c and 3.7d the mean value on the destitutions has moved, firstly to the left for the 17 nm (Fig. 3.7a) thin film, mention that small density and small size islands are distributed throughout the surface and secondly to the right for 19 nm (Fig. 3.7b) implying that higher density and larger islands cover the surface.

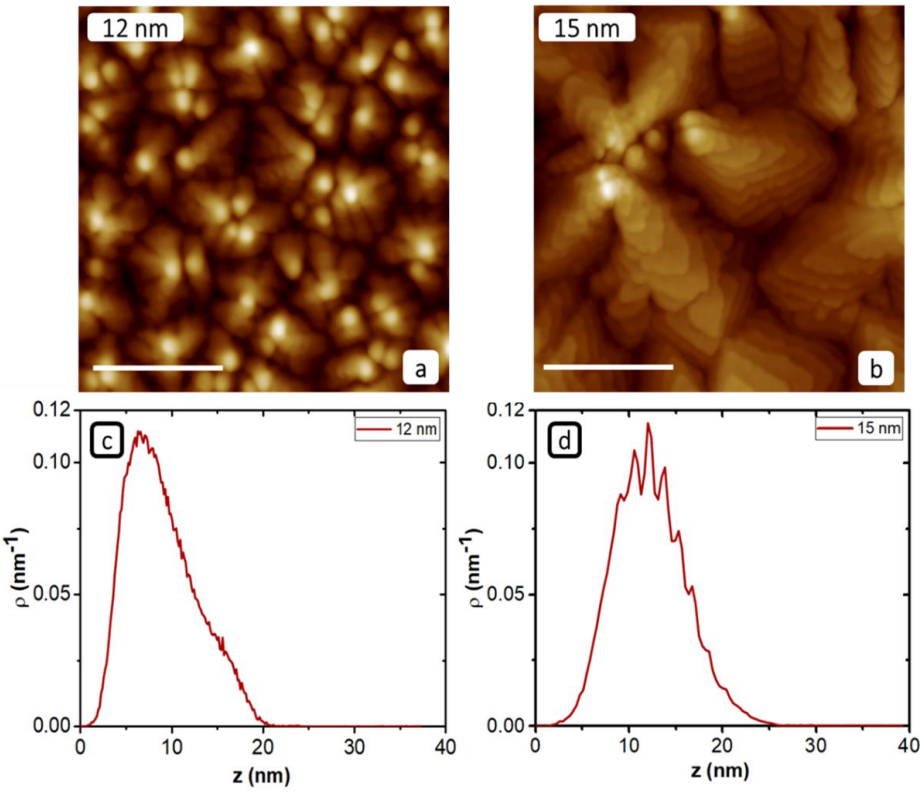

FIG. 3.6. 5 µm x 5 µm topographic images of pentacene thin films with different thickness deposited on SiO_2/Si wafers at 80°C. Rulers (white horizontal bar) are 2 µm long. Topography ranges from 0 nm (black) to (a) 21.6; (b) 23.3 nm (white)(c) and (d) histograms of topographic images showing the height distribution of pentacene thin films.

The last two figures (Fig. 3.8 and 3.9) show four different thicknesses of pentacene thin films. This alternation of the morphology can easily be distinguished. In Fig. 3.8a and Fig. 3.9a smaller islands are formed with respect to Fig. 3.8b and Fig. 3.9b. Due to the fact that the thickness is large enough to hide the possible changes in the morphology, the histograms shown in Fig. 3.8c and 3.8d and in Fig. 3.9c and 3.9d reveal this change on the morphology, whereas the mean value (weighted center) of the distribution undergoes damped back and forth oscillations.

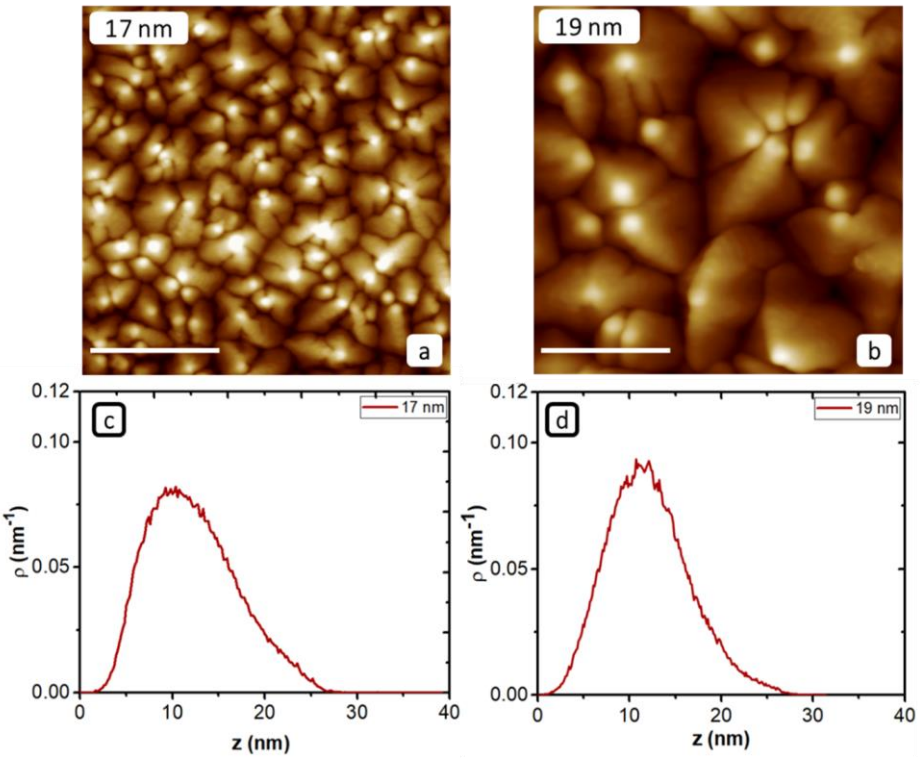

FIG. 3.7. 5 μm x 5 μm topographic images of pentacene thin films with different thickness deposited on SiO_2/Si wafers at 80°C. Rulers (white horizontal bar) are 2 μm long. Topography ranges from 0 nm (black) to (a) 30.0;(b) 38.0 nm; (white)(c) and (d) histograms of topographic images showing the height distribution of pentacene thin films.

In the last thickness that were studied a remarkable observation is that the change of the morphology is not dependent on the substrate. In all growth processes, the substrate has an important role for the definition of the morphology. The first monolayers are generated upon the action of a Van der Waals potential that is evolving with film thickness, and hence are extremely sensitive to the substrate. In the present case, we observe this swapping back and forth of the morphology at increasing thicknesses.

Another thing that we notice is that in all histograms we can distinguish some peaks, mostly found on the right side of the distributions. They exhibit smaller height differences, e.g., 0.8-1 nm, revealing either metastable or tilted phases at very low coverages of the layer. This is particularly evident for the 3 nm film, where most of the coverage is contributed to a bilayer with terraces of

1.5 nm height, while the second bilayer which contributes lesser coverage, consists 1 nm high terraces.

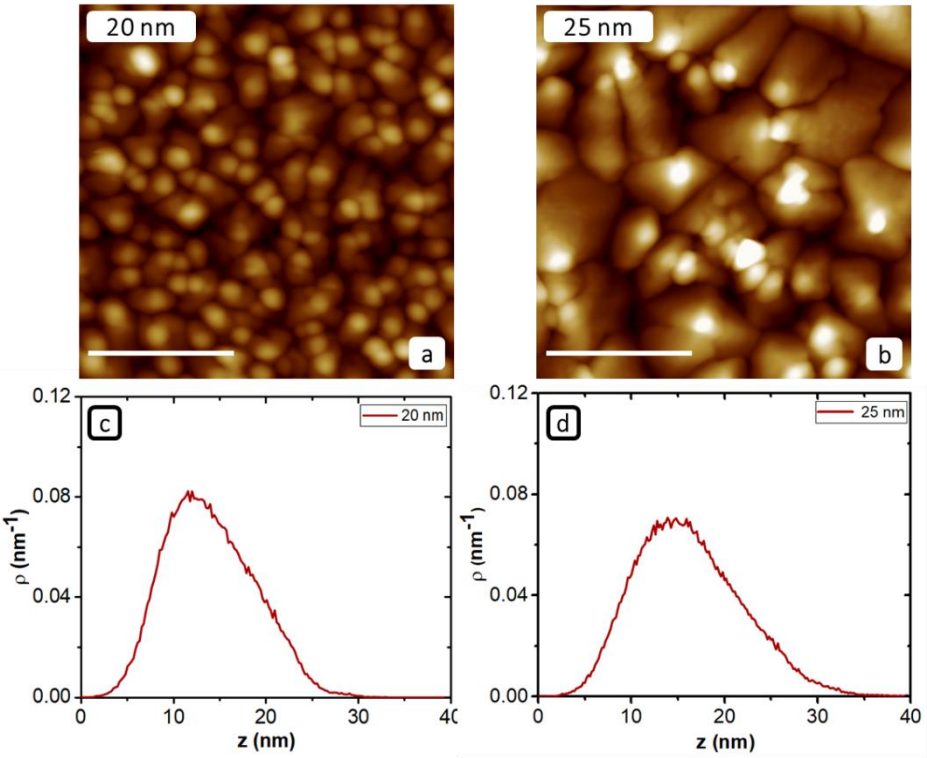

FIG. 3.8. 5 µm x 5 µm topographic images of pentacene thin films with different thickness deposited on SiO_2/Si wafers at 80°C. Rulers (white horizontal bar) are 2 µm long. Topography ranges from 0 nm (black) to (a)38.0;(b) 40.0 nm; (white)(c) and (d) histograms of topographic images showing the height distribution of pentacene thin films.

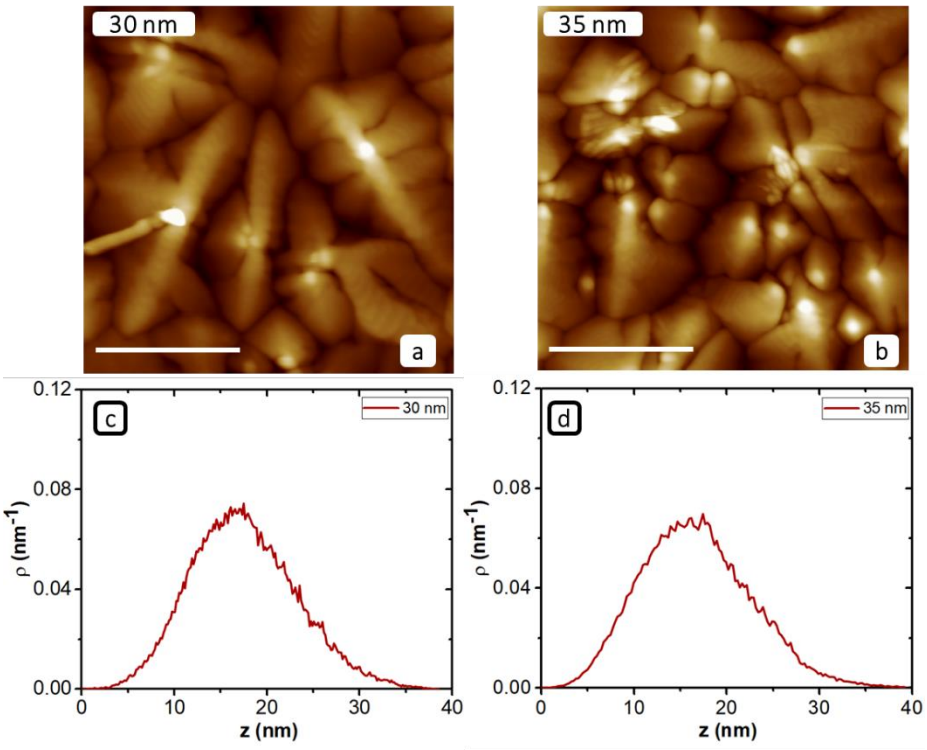

FIG. 3.9. 5 μm x 5 μm topographic images of pentacene thin films with different thickness deposited on SiO_2/Si wafers at 80°C. Rulers (white horizontal bar) are 2 μm long. Topography ranges from 0 nm (black) to (a)40.0;(b) 41.0 nm; c) (white)(c) and (d) histograms of topographic images showing the height distribution of pentacene thin films.

In order to understand more about this morphological change quantitative analysis was carried on. The morphological parameters such us the roughness (σ) and three correlation lengths (ξ_1, ξ_2, ξ_3) are measured by fitting of the experimental data as a function of the evolution of the thickness. In Fig. 3.10 we show the correlation lengths that are extracted from the linear power spectral density (PSD) vs wavevector $k=2\pi/x$ (x being the spatial length), as already illustrated in our previous works. [23] Correlation lengths ξ_1, ξ_2 and ξ_3 are termed the larger, medium, and smaller characteristic length scales that are associated to the island size, the branch in the islands, and the exposed terrace width, respectively. The correlation lengths ξ_1, ξ_2 and ξ_3 in Fig. 3.10a, 3.10b, 3.10c exhibit stretched oscillations vs thickness, as evidenced by the segment-and-marker guide-to-the-

eye. The maxima and minima of these oscillations are in-phase among the three characteristic lengthscales.

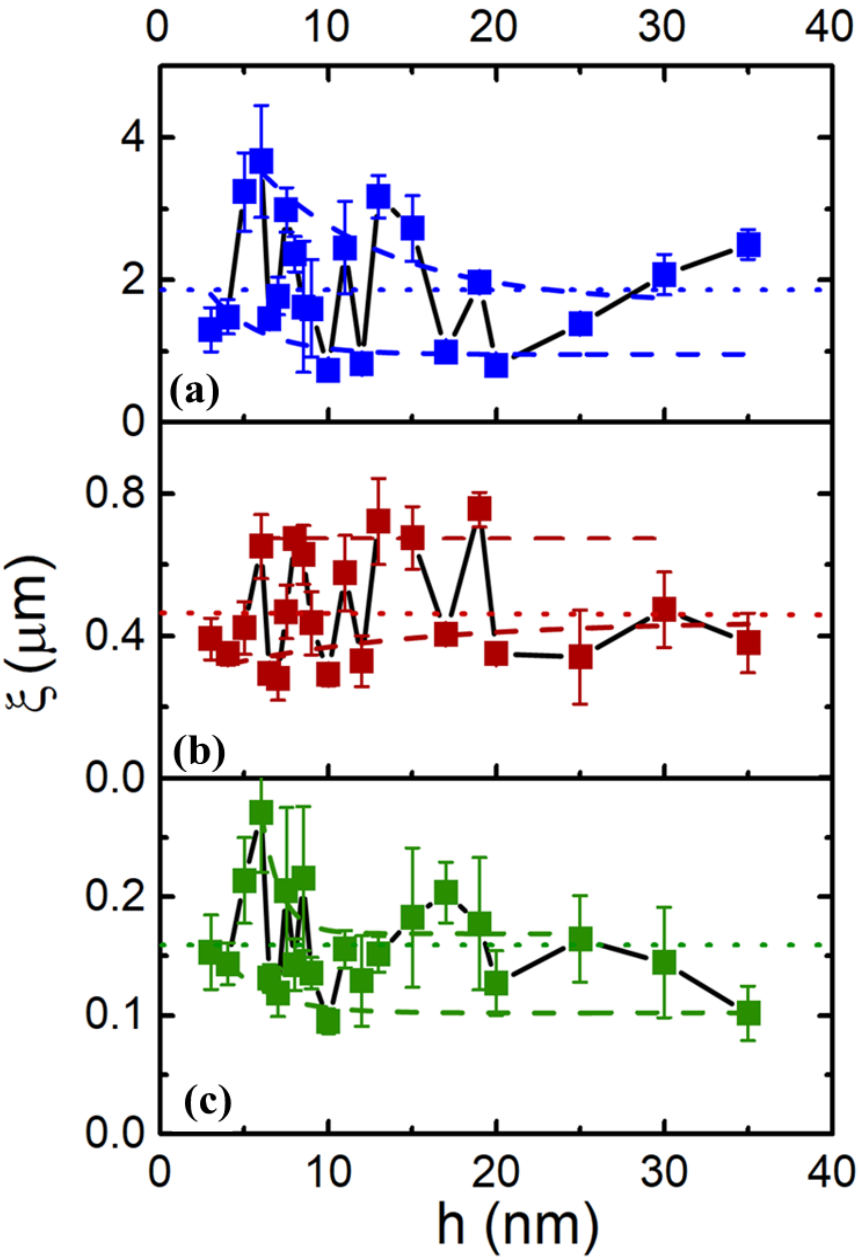

FIG. 3.10. (a-c) Correlation lengths vs thickness: (a) ξ_1 (blue), (b) ξ_2 (red) and (c) ξ_3 (green). The dotted lines correspond to the mean value of the correlation lengths. The dashed lines are the fitted envelopes of maxima and minima of ξ_1, ξ_2 and ξ_3.

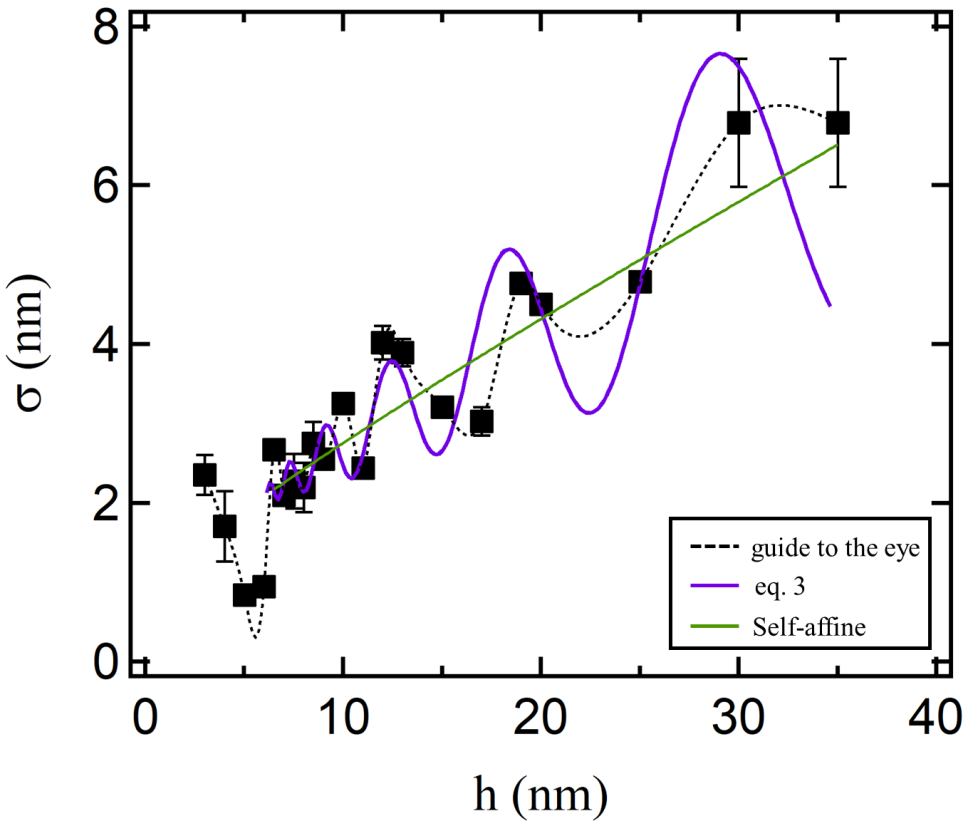

FIG. 3.11. Evolution of roughness versus thickness. The black dash line corresponds to the data interpolation and serves as guide to the eye; The continuous purple line is the fitting of the experimental data with eq. (3); the green line is the power law fitting eq. 2 to the data above the first oscillation (h>5.4 nm). The best fit parameters are a_0=1.87±0.02 nm, β=0.64 ±0.01, and we set σ_0=0 nm and h_0=5.4 nm.

The rms roughness σ exhibits an oscillatory behavior superimposed to a monotonically increasing trend. Fig. 3.11 shows the experimental data and their interpolation curve (dashed black line) estimated with cubic spline to evidence the oscillations. We notice that an anti-phase relation links ξ_1 with the roughness, since the minima of ξ_1 are observed in correspondence with the maxima of the roughness, and vice versa.

In the following, a series of increasingly more complex and physically sound models are described, in order to explain the oscillatory behavior of the roughness (and indirectly of the correlation lengths).

Self-affine growth.

In all previous reports of transitions from layer-by-layer to island growth, also termed rapid roughening in organic thin films, the roughness follows a power law vs thickness. [5,8,10,15] Power law is the fingerprint of self-affine growth with scale invariance in time (thickness is indeed time when the rate of deposition is kept constant as in our case). We describe the power law scaling as:

$$\sigma = \sigma_0 + a_0 \left(\frac{h}{h_0}\right)^{\beta} \qquad (2)$$

It is observed that the growth exponent β usually takes values between 0.5 and 1. [24,25] We clarify the slight different form of Eq. 2 with respect to the power laws in the literature. We introduce here the characteristic thickness h_0 to normalize the thickness to "monolayers" and produce parameters that have intuitive physical dimensions. According to eq. 1, in layer-by-layer growth the first minimum would occur at Θ =1 ML. We notice that the first minimum is at 5.4 nm, which is about four times the height of one molecular layer of standing pentacene molecules (1.4 nm for the bulk Campbell's phase and 1.5 nm in Holm's phase). Thus, we set h_0= 5.4 nm. Our unusually large value for h_0 is however in qualitative agreement with earlier observations by Ruiz and Malliaras which find the onset of self-affine growth in pentacene thin films at ≈6 MLs (1 ML corresponding to 1.5 nm in their work). [26]

In Fig. 3.11, the continuous green line is the power law fit of the experimental data above the first oscillation. Best fit parameters are shown in Table 3.3. The exponent value is rather robust with respect to the positioning of fitting range limits, for instance is 0.74 with the whole data set, and

0.67 for data with h>10 nm. These values are all in agreement with the earlier reports of rapid roughening in molecular thin films made of pentacene or other oligomers. [14,15]

Table 3.3. Parameters corresponding to the fitting in Fig. 3.11 described by eq. 2.

Parameters Self-affine growth	Best fit values	Estimated error	Fixed or Free
σ_0 *(nm)*	0.79	± 0.41	free
a_0 *(nm)*	1.17	± 0.36	free
h_0 *(nm)*	5.4	± 0	fixed
β	0.84	± 0.14	free

Failure of Distributed Growth Model

Remarkably, we observe the roughness oscillations do not vanish after one or two oscillations, as typical of the layer-by-layer to island growth. Indeed, the oscillations occur at all thicknesses in the range explored. Moreover, aside for the first oscillation, we observe no damping in their amplitude. This is already new with respect to earlier reports where the initial oscillations of the layer-by-layer mode are rapidly damped to a self-affine increase upon the sudden transition to island growth. [5] The layer-by-layer to island growth transition can be properly described by means of the distributed growth model (DGB) [27], where local energy barriers like Erlich-Schwoebel lead to the net molecular flux from the bottom layer towards the top. This causes the layer-by-layer to island growth transition at a critical thickness. Our case is at variance with the DGB model because the period of the oscillation keeps on increasing with the increasing thickness, whereas the amplitude is not damped (even if we subtract the power law trend from the data). We tried to fit our DBG model curve, however this converges to a power law without exhibiting any marked oscillation as shown in Fig. 3.12.

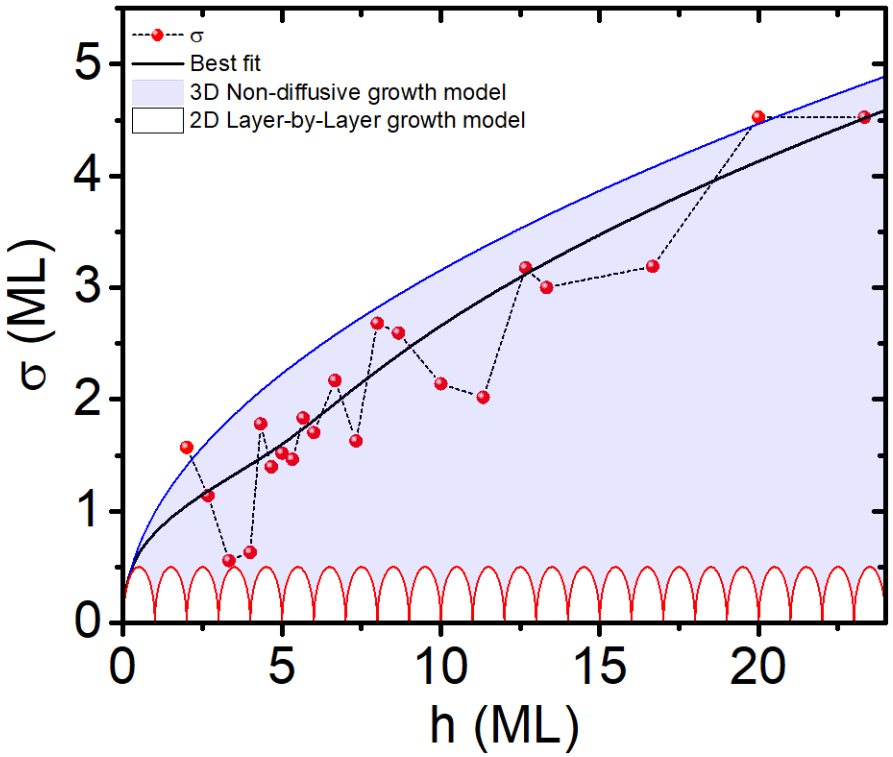

FIG. 3.12 Figure showing the result of the fit of roughness with the Cohen's Distributed Growth Model (DGM). The oscillating part described be red solid line corresponds to the behavior of RMS for perfect 2D (layer-by-layer) growth model. The blue shadow part corresponds to the 3D growth model (non-diffusive). Plot by courtesy of Dr. Francesco Borgatti (CNR-ISMN Bologna, Italy).

Model based on discrete scale invariance

To explain the observed oscillations of the roughness, we first tried to adapt the theory of renormalization formulated by Sornette et al. that describes the scale invariance of generic observables *O* with oscillatory behavior. [28] The theory uses discrete wave transforms where the oscillation undergoes a logarithmic periodic scaling, with the period proportional to the relevant scaling exponent (in our case β). Thus, we adapt their main equation 23 into the following equation:

$$\sigma = \sigma_0 + \left(\frac{h-h_0}{h_0}\right)^{\beta}\left[a_0 + a_1 \sin\left(2\pi\frac{\beta}{ln\mu}\ln\left(\frac{h-h_0}{h_0}\right) + \varphi_1\right) + a_2 \sin\left(2\pi\frac{\beta}{ln\mu}\ln\left(\frac{h-h_0}{h_0}\right) + \varphi_2\right)\right] \quad (3)$$

where in the wave transform one recognizes the zero-frequency component being our eq. 2, and the first two harmonics as from eq. 23 of reference [27] are made explicit. Here μ is the scaling factor: $O(\mu^{-\beta}x)= \mu O(x)$. In order to restrict the parameter space, we fix the parameters σ_0, α_0, h_0, β according to best fit values from eq. 2, and then we fit the experimental data with the first wave only using as fitting parameters a_1, μ, φ_1. In Fig. 3.11 the purple line is the best fit obtained with parameters reported in Table 3.4. Albeit the fit is not perfect, the function eq. 3 encompasses some distinctive features of the roughness oscillatory behavior: i) the period that is stretching with the thickness above a critical thickness, and ii) the amplitude that is not damped.

Table 3.4. Parameters corresponding to the fitting in Fig. 3.11 described by eq. 3.

Parameters	Best fit values	Estimated error	Fixed or Free
σ_0 *(nm)*	1.13	± 0.01	free
a_0 *(nm)*	1.87	± 0	fixed
h_0 *(nm)*	5.4	± 0	fixed
β	0.64	± 0	fixed
a_1 *(nm)*	0.55	± 0	fixed
φ_1	1.74	± 0.03	free
μ	1.75	± 0	fixed

However, we notice that the fit with eq. 3 does not superimpose properly to the maxima and minima of the oscillation (e.g., compare with the interpolation dashed line in Fig. 3.11), and the broadening of the waves increases too slowly with the thickness. By inspection, the problem may arise from the logarithmic dependence on *h* and the fact that the waves in eq. 3 are "centered" to the same critical height h_0. The trend of the experimental data hints to the possibility that also the center of the wave may shift monotonically with the thickness *h*, instead of remaining fixed. According to ref. [28] it would imply shifting the critical coverage, which indeed is consistent with our observation.

Our idea is then to endow the waves in eq. 3 not only with the stretching period but also with a shifting reference. We implement it by constructing a functional that resembles the features of local waves (also known as wavelets) [29,30] superimposed to the self-affine trend in eq. 2. We

therefore took eq. 3 and modified it in such a way that both the frequency and the center of the wave are functions of *h*. To represent the shift of period and wave center, we adopt a power law. The resulting function is:

$$\sigma = \sigma_0 + a_0\left(\frac{h}{h_0}\right)^{\beta} + a_1 \sin\left(2\pi \ln\left(\frac{h-d_0h^p}{g_0h^q}\right) + \varphi_1\right) + a_2 \sin\left(4\pi \ln\left(\frac{h-d_0h^p}{g_0h^q}\right) + \varphi_2\right) + \ldots \quad (4)$$

Here there are new fitting parameters in addition to the ones in eq. 3: d_0, g_0, p, q. The result of the fitting with eq. 4 is shown in Fig. 3.13, as red line.

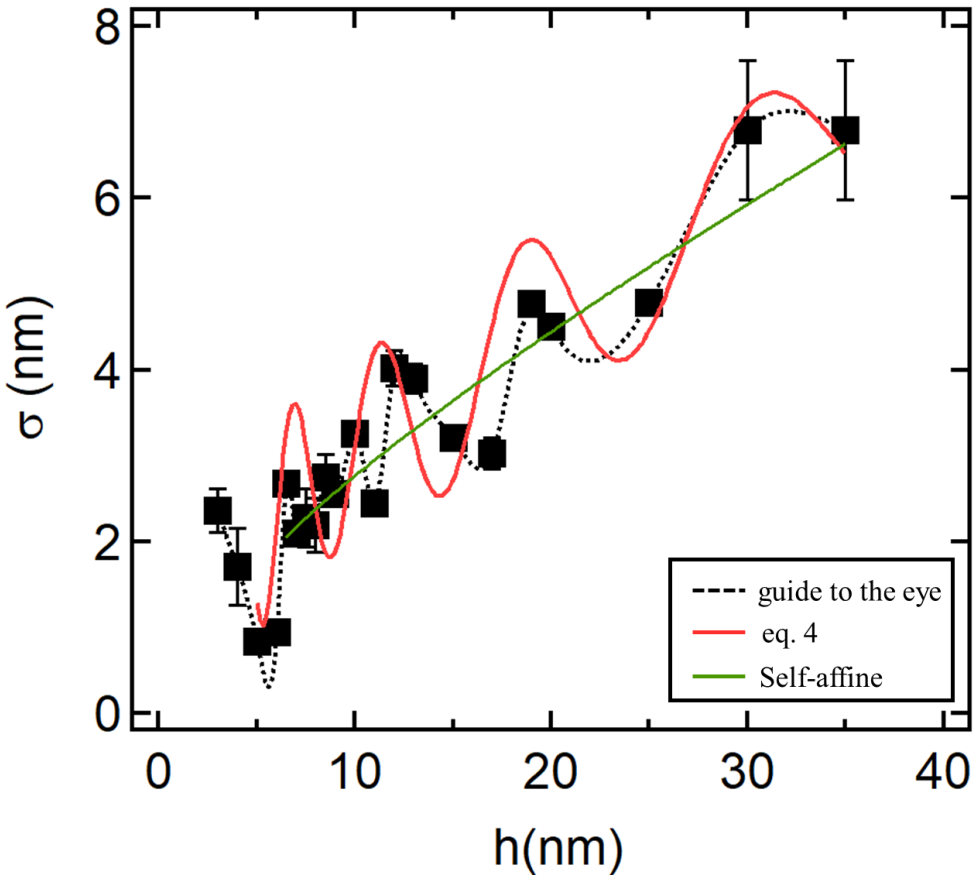

FIG. 3.14. Evolution of roughness versus thickness. The black dashed line corresponds to the data interpolation and serves as guide to the eye; The continuous red line is the fitting of the

experimental data with eq. (4); the green line is the power law fitting eq. 2 to the data above the first oscillation (h>5.4 nm).

The corresponding best fit parameters are reported in Table 3.5. The parameters from the function as in eq. 2 were kept fixed. We notice that the curve is now reproducing not only the essential features of the roughness oscillations, but also and quite nicely the maxima and minima of the oscillations. This agreement may be the result of the increased dimension of the variational parameter space, and to restrict the number of free parameters, we invoke some physical model based on the phenomenology observed. The process is described in the next section.

Table 3.5. Parameters corresponding to the fitting in Fig. 3.14 described by eq. 4.

Parameters	Best fit values	Estimated error	Fixed or Free
σ_0 *(nm)*	1.38	± 0.016	free
a_0 *(nm)*	1.17	±0	fixed
h_0 *(nm)*	5.4	± 0	fixed
β	0.84	±0	fixed
a_1 *(nm)*	0.4	± 0	fixed
φ_1	1.74	± 0.03	free
a_2 *(nm)*	0.55	± 0	fixed
φ_2	1.74	± 0.03	free
p		±	fixed
q	2	± 0	fixed
d_0 *(nm^(1-p))*	0.010	± 0	free
g_0 *(nm^(1-q))*	0.010	± 0	free

Continuous wetting/dewetting transitions

We propose an alternate explanation of the observed oscillations of the roughness. We start noticing that there is a resemblance between the oscillations of the roughness with some of the features of dewetting, in particular those that are associated to the phenomenon termed spinodal dewetting. [11,31,32] In spinodal dewetting the time evolution of the fluctuating topographic profile leads to the emergence of the characteristic wavelength as the distance between the peaks or the valleys of the film topography. In our case, this characteristic wavelength of dewetting λ would measure the distance between the islands which is ξ_1 in Fig. 3.10. The occurrence of dewetting, hence, the "rupture of the film", would correspond to the situation with minimum ξ_1, and, because of the anti-phase relation between them, maximum surface roughness. Vice versa, wetting corresponds to the maximum ξ_1 and the minimum surface roughness. Based on this, we infer that the thickness of the dewetting layer does not encompasses the whole thickness of the film, instead can be ascribed to the upper pentacene layers. We envision that these are the ones mostly contributing to the islands, and hence to roughness. The lower layers forming the smooth basal plane are not directly involved in the dewetting.

In continuous theories of dewetting, [32] the characteristic wavelength λ scales with the thickness as a power law:

$$\lambda = \lambda_0 \left(\frac{h}{h_c}\right)^2 \qquad (5)$$

The wetting/dewetting transition as in eq. 5 occurs for film thickness h lower than the critical thickness h_c. We associate the "smoothly varying period" of the oscillations observed in our experiment to the "critical thickness of dewetting h_c". [32]

To assess this hypothesis, we extract the periods λ of the oscillations of the roughness and plot them as a function of the film thickness. We estimate the periods λ as distances between adjacent peaks, e.g., from a maximum to the next, and from a minimum to the next. We refer the periods λ to the thickness of the peak or valley where the period starts.

In Fig. 3.15, we show the scaling of $\lambda_{max\ (min)}$ vs $h_{max\ (min)}$, where the values were extracted, respectively, from the distances between adjacent peaks (maxima) and valleys (minima) of the rms roughness. The data reveal a monotonic increasing trend but, interestingly, they align on a common line. We fit all data (except the roughness maximum at 3 nm) with a power law whose exponent equals 2 in apparent consistency with spinodal dewetting. The best fit line is shown as the continuous blue line.

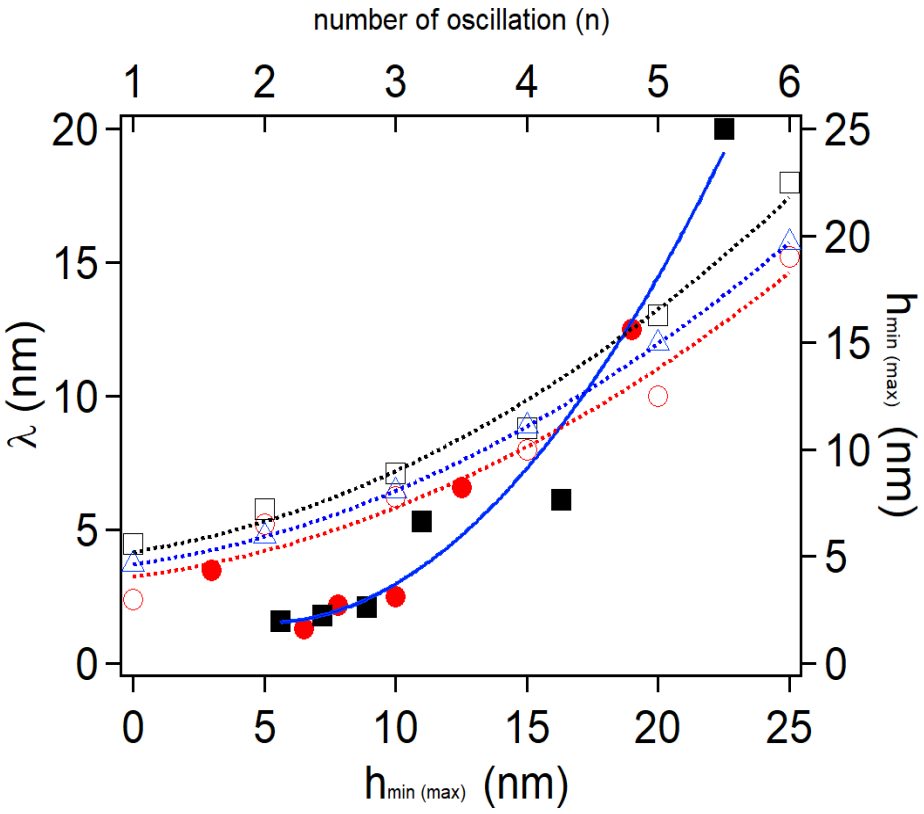

FIG. 3.15. Left and bottom axes: period λ between maxima (solid red circles) and minima (solid black squares) of the roughness σ versus the origin of the oscillation (expressed as the thickness of the maximum or minimum, respectively). Blue line is power law fit with exponent fixed to value 2. Right and top axes: the origin of the oscillations (as in the bottom axis) as maxima (empty red circles) and minima (empty black squares) vs the number n of oscillation. The dotted lines are power law fit scaling as proportional to n^2. The blue empty triangles are the mean between maxima and minima, and its blue dotted line is power law fit scaling as proportional to n^2.

In Fig. 3.15, we notice that if we take the mean value between adjacent minimum and maximum, then also these mean points obey the same scaling vs h. We take the mean values (blue empty triangles) of the maxima and minima in Fig. 3.15 and refer them as the centers h_c of the local wave, whose period is given by $\lambda(h_c)$ as from eq. 5. We construct a look-up table where the experimental data are classified according to their thicknesses h as belonging to a common center h_c and period $\lambda(h_c)$. In Fig. 3.16 we plot h_c vs h where the stepwise structure described above is evident. We then approximate the stepwise function by fitting it with a continuous function:

$$h_c(h) = A\left[1 - exp\left(-\left(\frac{h}{h_1}\right)\right)^{\beta}\right] + C \qquad (6)$$

The parameters that describe the dependence of the (discrete) centers of the local waves are reported in Table 3.6. h_1 is a characteristic thickness that appears here because of the limited amount of data. Albeit this function contains artifacts, describes smoothly our data set (is monotonic and can be inverted).

Table 3.6. Parameters corresponding to the fitting in Fig. 3.16 described by eq. 6.

Parameters	Best fit value	Errors	Fixed/Free
A	17.341	± 0	fixed
β	2	± 0	fixed
C	2.82	± 0	fixed
h_1	13.192	± 0	fixed

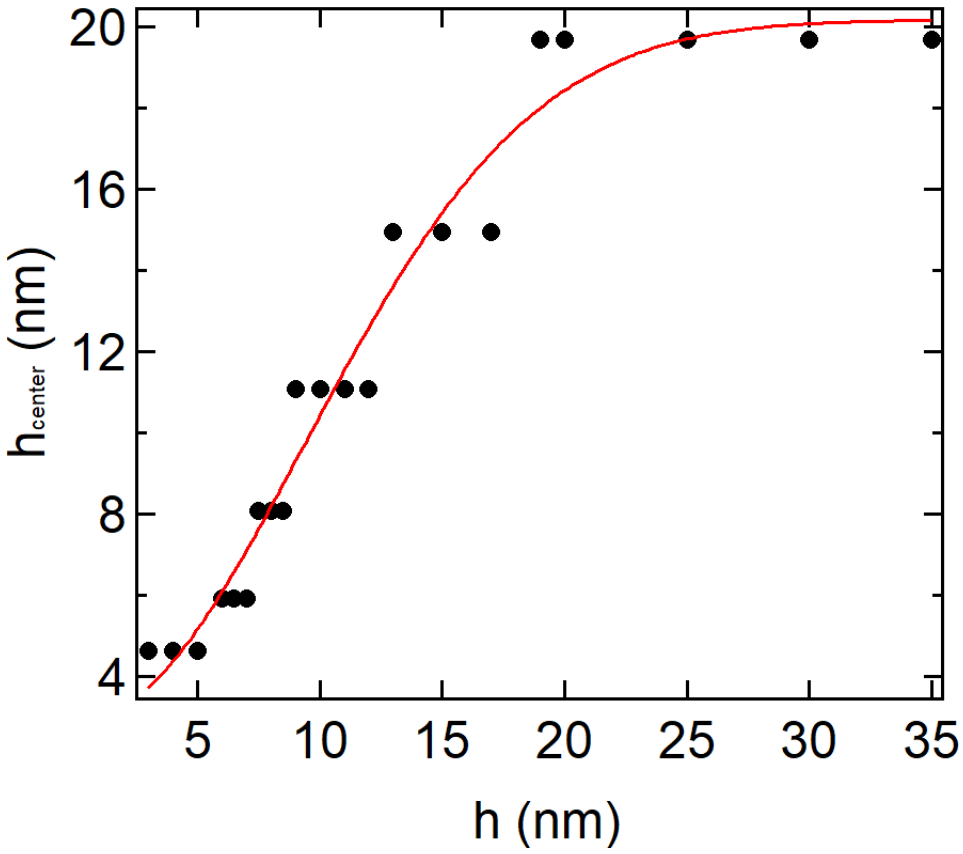

FIG. 3.16 Plot of the centers h_c of the oscillations vs thickness h. Continuous line is the fit according to eq. 6.

According to the wetting/dewetting picture, we express the period scaling vs thickness in Fig. 3.15 as:

$$\lambda(h) = f_0 + g_0[h - h_c(h)]^2 \quad \text{for} \quad \frac{h}{h_c} \ll 1 \tag{7}$$

Eq. 7 incorporates the features typical of wavelets: i) the center of the local wave, h_c shifts with the increasing film thickness; and ii) the period (wavelength) of the local wave (spread of the oscillation) increases with thickness.

Based on this, we provide a new heuristic equation that we use to fit the oscillations of rms roughness. The heuristic equation encompassing both self-affine correlated growth and the oscillatory features of spinodal dewetting. [6,15] reads:

$$\sigma(h) = \sigma_0 + a_0\left(\frac{h}{h_0}\right)^{\beta} + a_1 \sin\left(2\pi\left[\frac{h-h_c(h)}{\lambda(h)}\right] + \varphi_1\right) + a_2 \sin\left(4\pi\left[\frac{h-h_c(h)}{\lambda(h)}\right] + \varphi_2\right) \qquad (8)$$

In equation (8) two mechanisms describe this anomalous growth mode: self-affine growth and spinodal dewetting that induces the spontaneous formation of spatially correlated nanostructures. Eq. 8, despite of being phenomenological, bears a value as it is parametrized on observables independently extracted from the roughness experimental data. The agreement of our fit with eq. 8 and the experimental data shown in Fig. 3.17 is excellent. Best fit parameters are reported in Table 3.7.

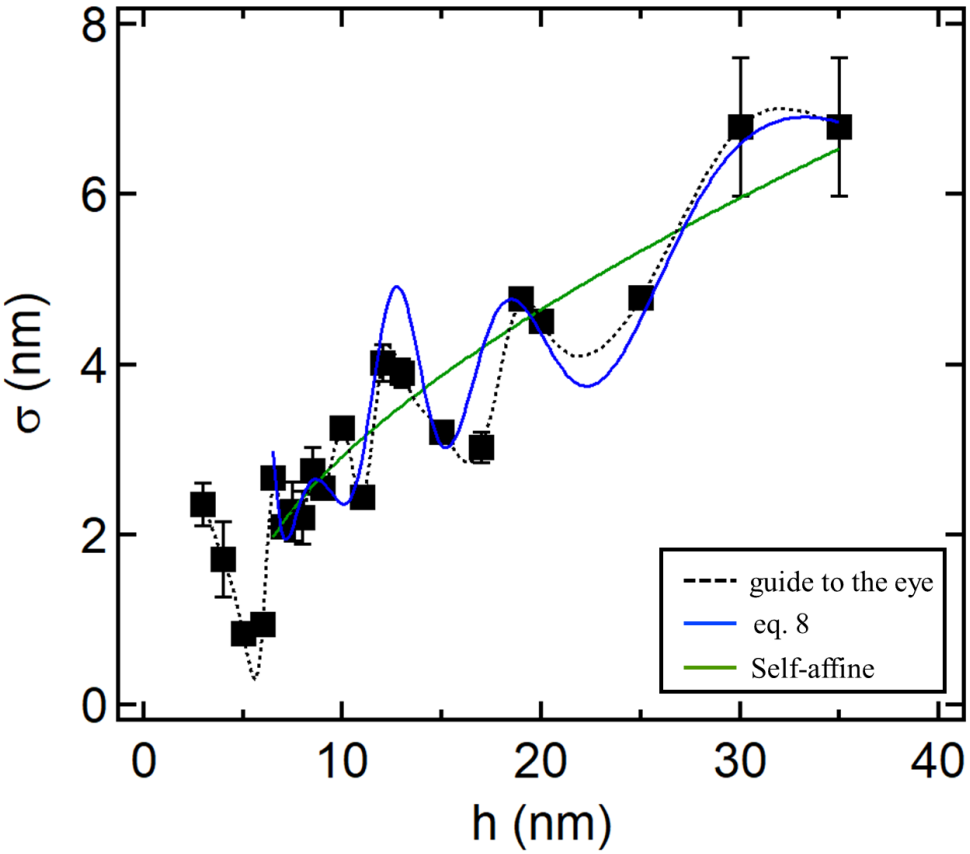

FIG. 3.17. Evolution of roughness versus thickness. The black dashed line corresponds to the data interpolation and serves as guide to the eye; The continuous blue line is the fitting of the experimental data with eq. (8); the green line is the power law fitting to the data above the first two oscillations.

Table 3.7. Parameters corresponding to the fitting in Fig. 3.17 described by eq. 8.

Equation 8:	values	error	
σ_0	1.20	± 0	fixed
α_0	1.41	± 0	fixed
h_0	5.4	± 0	fixed
β	0.64	± 0	fixed
α_1	0.17	± 0	fixed
A	8.89	± 0	fixed
h_1	5	± 0	fixed
f_0	1.5	± 0	fixed
g_0	0.057	± 0	fixed
q	2	± 0	fixed
C	-0.51	± 0	fixed
φ_0	16.87	± 0.07	free
α_2	0.9	± 0	fixed
φ_1	13.22	± 0.06	free

Our finding poses some relevant questions on the mechanism operating here, as our pentacene thin films cannot be assimilated to continuous films, instead they are solid but made of discrete molecular terrace stacks. Theories of dewetting are usually explained by equilibrium arguments, and the transition wetting/dewetting is explained as moving back to equilibrium from a metastable spreading state (according to Le Chatelier principle or pursuing the minimum chemical potential). Here, the driving force is not exclusively thermodynamics, as we observe iteration of wetting/dewetting transitions superimposed to a monotonic self-affine growth. Indeed, if the phenomenon were a genuine (spinodal) dewetting, over time it would lead to the emergence and consolidation of the characteristic wavelength that becomes the distance between islands. This

would happen once, and no more. The oscillations indicate iterations which must undergo kinetic control. On whether this is related to secondary, tertiary, and so on nucleation and growth phenomena we cannot state at this time, and further investigations are needed.

3.3 Discussion

In this Chapter, we observed a new growth mode of pentacene thin films and tried to explain the data that exhibit new and interesting features vs thickness. The oscillations of the roughness (σ) as the thickness increases were shown to be in anticorrelation with all the correlation lengths (ξ_1, ξ_2, ξ_3). We invoke the combination of two different phenomena which took place during the film growth. A kinetic phenomenon of roughening of the thin film together with a quasi-equilibrium phenomenon which resembles spinodal dewetting. We proposed two new heuristic equations (4) and (8) to fit the roughness oscillations embodying the distinctive features of self-affine growth and dewetting. [8,32]

3.4 References

[1] H. Sirringhaus, P. J. Brown, R. H. Friend, M. M. Nielsen, K. Bechgaard, B. M. W. Langeveld-Voss, A. J. H. Spiering, R. A. J. Janssen, E. W. Meijer, P. Herwig, and D. M. de Leeuw, Nature **401**, 685 (1999).

[2] S. R. Forrest, Nature **428**, 911 (2004).

[3] G. Witte and C. Wöll, J. Mater. Res. **19**, 1889 (2004).

[4] A. Brillante, I. Bilotti, R. G. Della Valle, E. Venuti, A. Girlando, M. Masino, F. Liscio, S. Milita, C. Albonetti, P. D'angelo, A. Shehu, and F. Biscarini, Phys. Rev. B **85**, 195308 (2012).

[5] S. Chiodini, A. Straub, S. Donati, C. Albonetti, F. Borgatti, P. Stoliar, M. Murgia, and F. Biscarini, J. Phys. Chem. C **124**, 14030 (2020).

[6] F. Biscarini, P. Samorí, O. Greco, and R. Zamboni, Phys. Rev. Lett. **78**, 2389 (1997).

[7] H. L. Cheng, Y. S. Mai, W. Y. Chou, and X. W. Liang, Adv. Funct. Mater. **17**, 3639 (2007).

[8] F. Dinelli, M. Murgia, P. Levy, M. Cavallini, F. Biscarini, and D. M. de Leeuw, Phys. Rev. Lett. **92**, 116802 (2004).

[9] A. Chanhom and J. Nukeaw, in *2007 7th IEEE Conf. Nanotechnol. (IEEE NANO)* (IEEE, 2007), pp. 349–352.

[10] F. Schreiber, Phys. Status Solidi **201**, 1037 (2004).

[11] P.-G. de Gennes, F. Brochard-Wyart, and D. Quéré, *Capillarity and Wetting Phenomena* (Springer New York, New York, NY, 2004).

[12] S. Herminghaus, K. Jacobs, K. Mecke, J. Bischof, A. Fery, M. Ibn-Elhaj, and S. Schlagowski, Science (80-.). **282**, 916 (1998).

[13] D. Gentili, G. Foschi, F. Valle, M. Cavallini, and F. Biscarini, Chem. Soc. Rev. **41**, 4430 (2012).

[14] X. N. Zhang, E. Barrena, D. G. de Oteyza, and H. Dosch, Surf. Sci. **601**, 2420 (2007).

[15] A. C. Dürr, F. Schreiber, K. A. Ritley, V. Kruppa, J. Krug, H. Dosch, and B. Struth, Phys. Rev. Lett. **90**, 4 (2003).

[16] D. Holmes, S. Kumaraswamy, A. J. Matzger, and K. P. C. Vollhardt, Chem. - A Eur. J. **5**, 3399 (1999).

[17] R. B. Campbell, J. M. Robertson, and J. Trotter, Acta Crystallogr. **14**, 705 (1961).

[18] J. F. Moulin, F. Dinelli, M. Massi, C. Albonetti, R. Kshirsagar, and F. Biscarini, Nucl. Instruments Methods Phys. Res. Sect. B Beam Interact. with Mater. Atoms **246**, 122 (2006).

[19] S. D. Quiroga, A. Shehu, C. Albonetti, M. Murgia, P. Stoliar, F. Borgatti, and F. Biscarini, Rev. Sci. Instrum. **82**, 025110 (2011).

[20] S. Verlaak, C. Rolin, and P. Heremans, 139 (2007).

[21] R. Ruiz, B. Nickel, N. Koch, L. C. Feldman, R. F. Haglund, and A. Kahn, 1 (2003).

[22] I. Tonazzini, E. Bystrenova, B. Chelli, P. Greco, P. Stoliar, A. Calò, A. N. Lazar, F. Borgatti, P. D'Angelo, C. Martini, and F. Biscarini, Biophys. J. **98**, 2804 (2010).

[23] A. Calò, P. Stoliar, E. Bystrenova, F. Valle, and F. Biscarini, J. Phys. Chem. B **113**, 4987 (2009).

[24] J. Krim and J. O. Indekeu, Phys. Rev. E **48**, 1576 (1993).

[25] A.-L. Barabási and H. E. Stanley, in *Fractal Concepts Surf. Growth* (Cambridge University Press, 1995), pp. 1–18.

[26] R. Ruiz, A. Papadimitratos, A. C. Mayer, and G. Malliaras, Adv. Mater. **17**, 1795 (2005).

[27] P. I. Cohen, G. S. Petrich, P. R. Pukite, G. J. Whaley, and A. S. Arrott, Surf. Sci. **216**, 222 (1989).

[28] D. Sornette, Phys. Rep. **297**, 239 (1998).

[29] W. Grzesik and S. Brol, J. Mater. Process. Technol. **209**, 2522 (2009).

[30] H. Zahouani and M. EL Mansori, Wear **376**–**377**, 178 (2017).

[31] G. Witte, K. Hänel, S. Söhnchen, and C. Wöll, Appl. Phys. A **82**, 447 (2006).

[32] F. B. Wyart and J. Daillant, Can. J. Phys. **68**, 1084 (1990).

Chapter 4

OFETs and EGOFETs response vs thin film thickness

"This chapter discusses the behavior of transistor parameters vs film thickness. The oscillatory behavior in phase with the morphological parameters is observed. In particular, the correlation of transconductance and roughness/correlation lengths oscillations is demonstrated."

4.1 Introduction

Organic thin films are the active layers in Organic Field Effect Transistors (OFETs) as well as in Electrolyte-Gated Organic Field Effect Transistors (EGOFETs). Therefore, the search for organic materials having excellent charge transport properties in thin films is an important topic. In last decades, organic semiconductors π-conjugated polymers and small molecules were studied extensively. [1,2] Charge transport in thin films is governed by hopping across disorder-induced localized states close to the Fermi level of the organic semiconductor. Previous studies have shown that the density of localized states (DOS) can be described as a Gaussian or an exponential distribution in the energy close to the Fermi level. [3,4] In OFETs charge transport occurs in the first few nm of the active layer closer to the gate dielectric surface. [5] In a molecularly ordered thin films, charge transport occurs only in the first one to three monolayers. [6] This charge transport is mostly two dimensional in character. [5,6] The upper monolayers, albeit may be populated with charge carriers, do not significantly contribute to the overall current, because of either greater resistance at domain boundaries that occur with higher density, else because of discontinuity of the percolation pathways. In Electrolyte-Gated Organic Field Effect Transistors, devices that are operated without an explicit dielectric layer and are gated through the electrolyte which form an electrical double layer (EDL). [7–9] Here, although the simplest models depict the gating as a surface capacitive coupling, there are hints about the penetration of ions (anions for *p-type* EGOFETs, cations for *n-type* EGOFETs) in the semiconductor layer, thus involving not only the geometrical surface but also (at least part of) the volume. [10–12] Ions, both cations and anions, possess small enough size, when undressed of their solvation shell, of penetrating even compact molecular layers as the one formed by the stacked pentacene monolayers, for instance by intercalating on the molecular sides along the long axis of standing pentacene molecules. The ion-p-interaction between them may indeed strongly deform the energy landscape where carriers move, thus leading to a modulation of the channel conductivity. It is also clear that morphological and structural defects will effectively contribute to create an electroactive surface area much larger than the basal plane, and therefore a correlation between morphology and device response may be envisioned.

In this chapter 4 we investigate the influence of the thickness on the response of OFETs in solid state operations and EGOFET in an electrolytic environment. The devices with pentacene thin films of different thicknesses as from Chapter 3 were characterized. Transfer curves of the transistor were plotted *versus* thickness and discussed below. Electrical parameters were extracted and their evolution with the morphology was analyzed.

4.2 Experimental part

For this study standard test patterns having a common gate as described in Section 2.1.3 were used. The test patterns were cleaned according to the following procedure. At first the devices were rinsed with acetone, followed by washing in hot piranha solution for 15 min and hydrogen fluoride water solution (2%). Then, the oxide surface was functionalized with hexamethylsilazane (HMDS) by thermal evaporation onto the cleaned surface. Twenty-one different thicknesses of pentacene thin film were evaporated at a rate of 0.1 Å/s. For the electrical characterization of the devices was used an Agilent B2912A Source-Measure-Unit (SMU), for more details see chapter 2 (Section 2.8).

Firstly, we performed electrical characterization of the device in solid state operation with OFETs shown schematically in Fig. 4.1. Transfer characteristics (I_{DS} vs V_{GS}) were acquired by sweeping the gate potential from V_{GS} 0 V to -40V and with a drain potential as V_{DS} = -20 V. Devices with different thicknesses were measured and electrical parameters were extracted and correlated with the thickness.

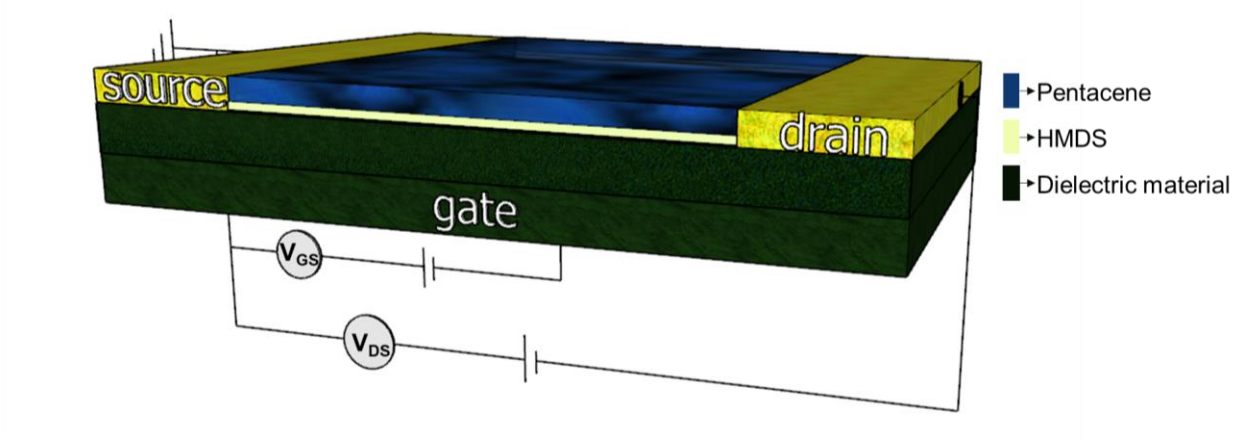

Fig. 4.1. A schematic diagram of Organic Effect Transistor (OFET).

Operations of the EGOFET were carried with an electrolyte top gate as schematically shown in Fig. 4.2. The gate electrode was a Pt wire (Ø = 800 μm). The cleaning procedure for the gate wire was sonication in ethanol and DI water 1:1 for 15 mins then drying with nitrogen flow. For the electrolyte, we used 50 mM KCl solution in deionized water. The volume of the droplet during the measurement was kept at 30 μl.

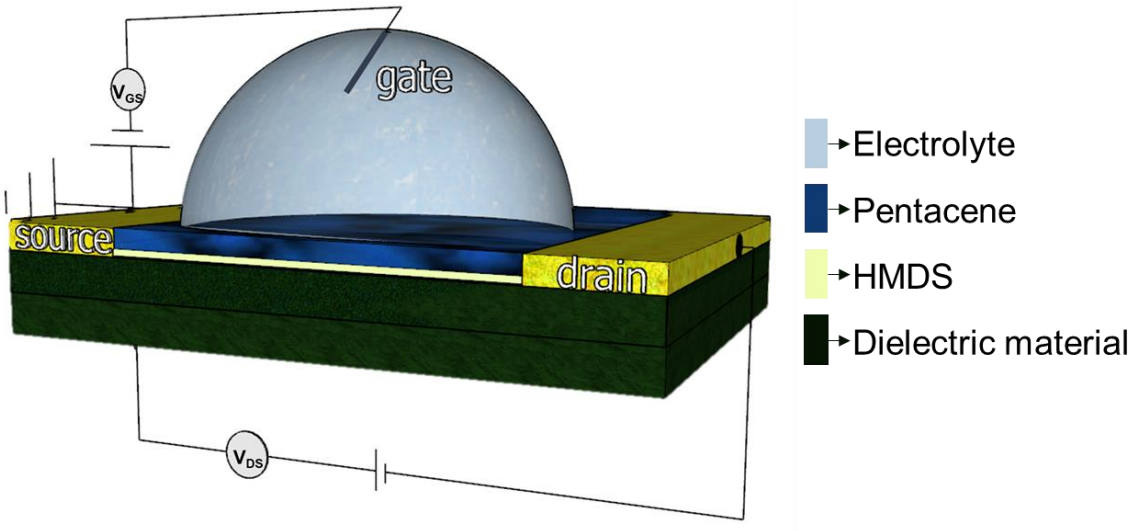

Fig. 4.2. A schematic diagram of Electrolyte-Gated Organic Field Effect Transistor (EGOFET).

I-V characterization was performed with gate potential sweep from V_{GS} 0.1 V to -0.5 V and a drain potential as V_{DS} = -0.2 V. The measurements were performed with a range voltage limited to 0.8 V to avoid the electrolysis of the water which occurs at 1.2 V. All the devices were measured in top gate operation, electrical parameters such as threshold voltage (V_{th}) and transconductance (g_m) were extracted and correlated with the different thicknesses of pentacene thin films.

4.3 Results

After the morphological characterization, the electrical measurements were performed. First the devices were measured in bottom gate operation. Fig. 4.3 shows the transfer characteristics of OFET as function of pentacene different thickness *h* expressed in nm. To convert it to coverage θ, that is the nominal fractional area, one needs to divide the value of *h* by 1.5 nm. Looking at the transfer characteristics, there is barely variation of the transfer curves with the increasing thickness of the thin film below 5 nm. This hints to an incomplete percolation channel in agreement with the dewetted morphologies in Chapter 3 Fig. 3.1. When the film thickness ranges from 5 nm to 8.5 nm, the current starts to increase. However, the trend is not monotonical and current fluctuations are observed within this range of thicknesses.

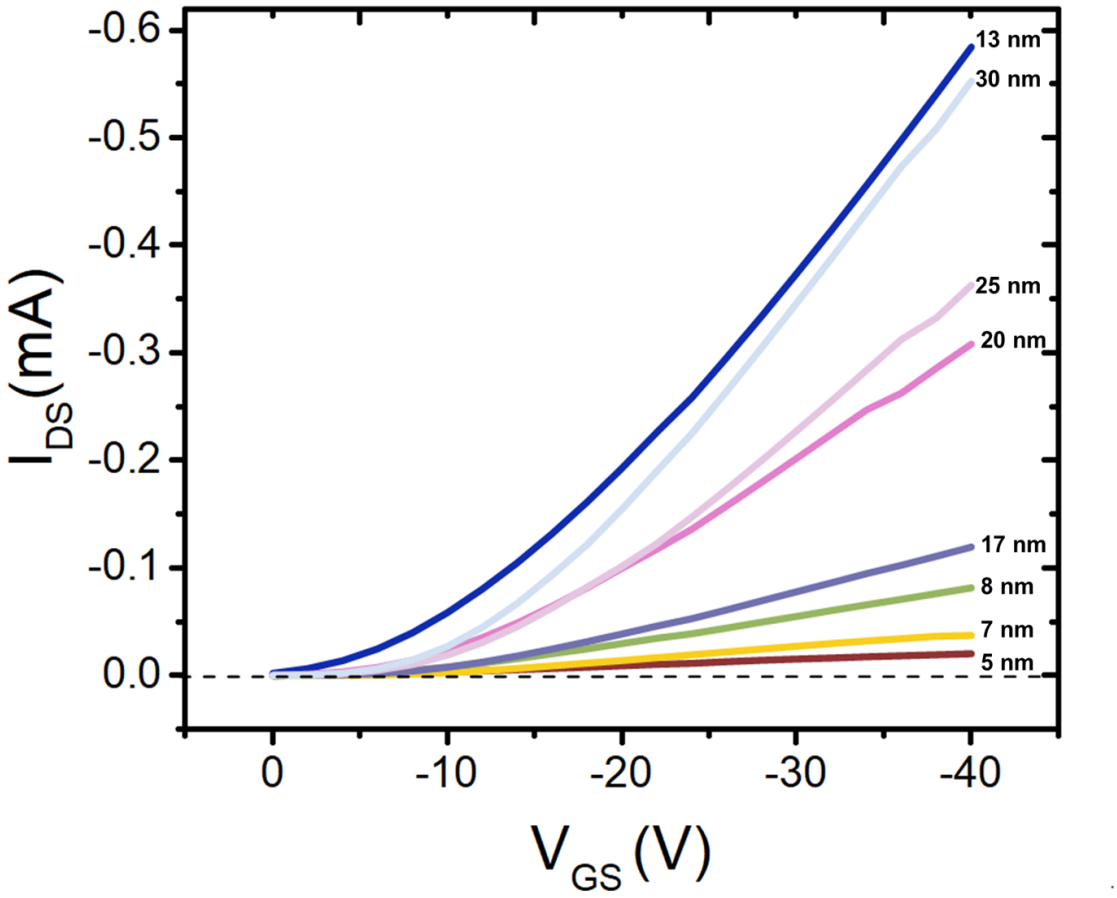

FIG. 4.3. Transfer characteristics pentacene thin films at different thicknesses in solid state operation with a drain potential V_{DS} = -20 V.

The devices with the highest currents correspond to devices with film thicknesses between 13 nm and 30 nm. These are the films where the first layers are completed and continuous, and where dewetting has not yet disrupted the large and continuous islands, thus leading to favor transport of the carriers across the channel where a few domain boundaries exist. On the other hand, at thicker films the current curves seem to decrease with respect to the 13 nm films, thus confirming the commonly observed "saturation of the response vs film thickness". This is consistent with the scenario where charge transport takes place only in the first few monolayers, and with the observation of dewetting of the upper layers that prevents the continuity of charge transport across the channel.

To understand better the behavior of the electrical response of the transistor, we extracted the transistor parameters. The trend of the threshold voltage is shown in Fig. 4.4.

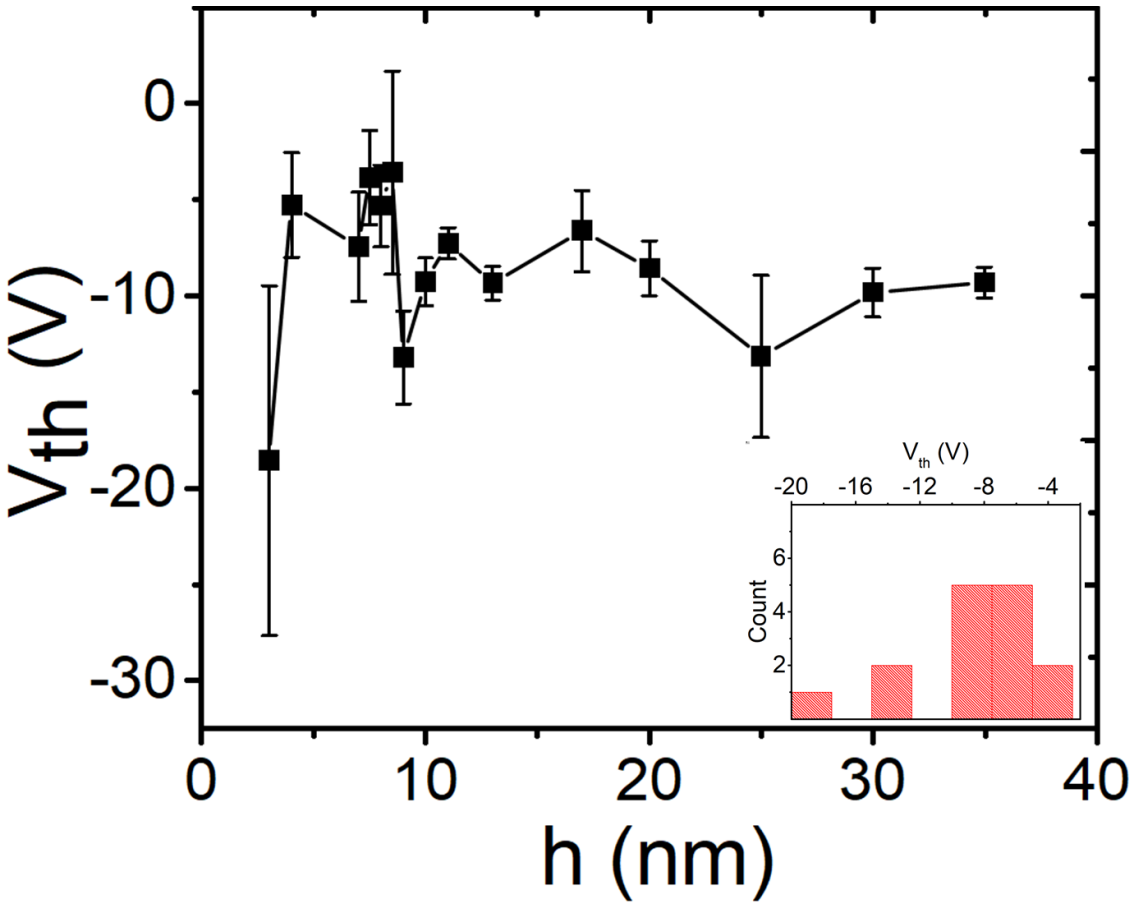

FIG. 4.4. Threshold voltage (V_{th}) vs thickness in solid state operation. Inset: histogram of the threshold voltage.

At the onset of percolation, a jump of the threshold voltage from close to -20 V to a few (negative) volts is observed. These large values for V_{th} explain the difficulty to generate current-carrying states in the channel and move the carriers across the channel. The coverage leading to continuous percolation pathways is not reached, and a low density of mobile carriers are accumulated. The increase of the thickness above 5 nm does not change substantially the values of V_{th} that fluctuates around -8 V with damped oscillations. The histogram also shows the more frequent occurrence

around -8 V. The oscillations of V_{th} seem to correlate with those of correlation length and roughness in Chapter 3 Fig. 3.10 and Fig.3.11 respectively, although there is not a very distinctive correlation between them.

We then extract the transconductance (g_m) whose evolution vs thickness is plotted in Fig. 4.5. The jump of the transconductance at the onset of percolation confirms the origin of the trend in terms of charge carrier percolation.

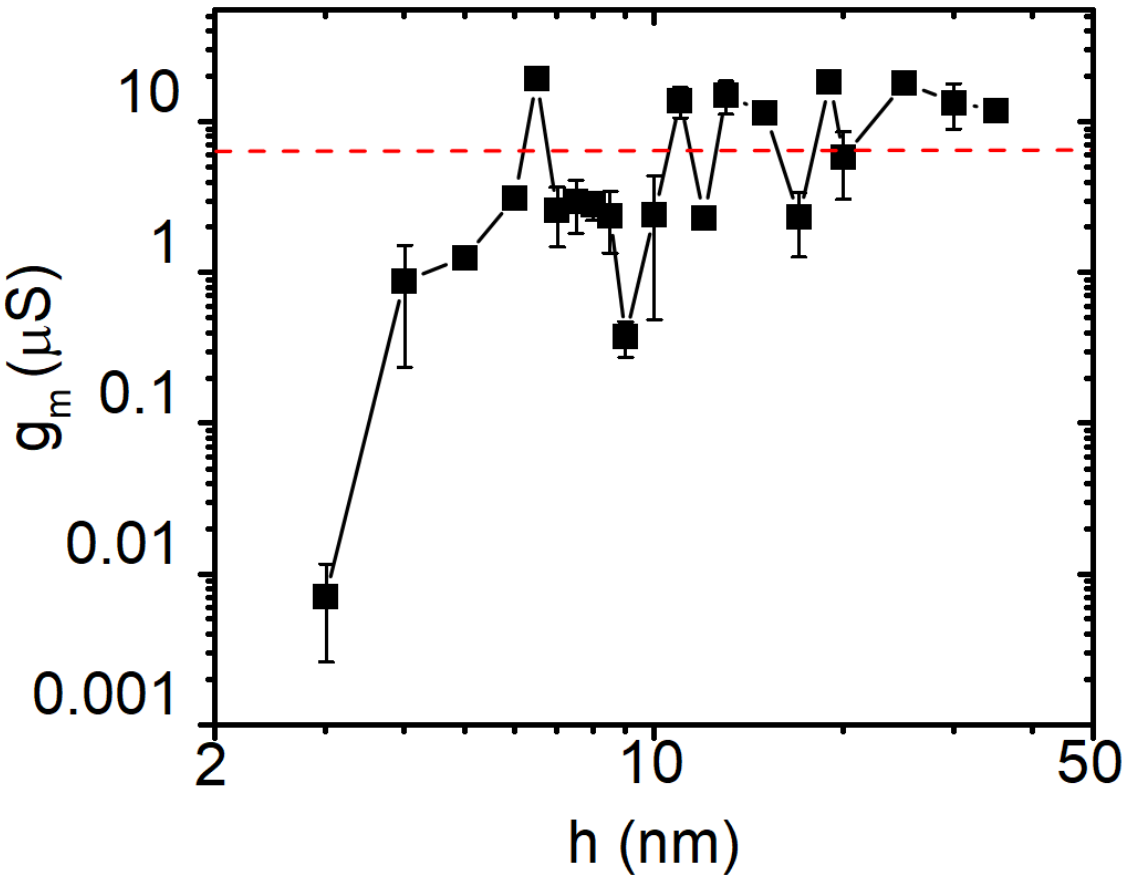

FIG. 4.5 Transconductance (g_m) vs thickness of OFET. The dashed red line corresponds to the mean value of the transconductance.

In this case, it is noticeable that the initial g_m increase is two orders of magnitude then the fluctuations exhibited range on one order of magnitude. If we consider a thickness invariant capacitance, then the main contribution to these variations of the transconductance are the charge carrier mobility fluctuations. Charge mobility of pentacene is high [13,14], when the path becomes complete at 6 nm. The oscillations of the transconductance at thickness > 6 nm are even more marked than the ones of the threshold voltage. These oscillations seem correlated to the ones of the correlation length/roughness in Chapter 3, with the "wetted/smooth" thin films exhibiting the higher transconductance. The fact that transconductance remains oscillating around a mean value of 8 mS indicates that the wetting/dewetting smoothing/roughening transitions reported in Chapter 3 involve partially the charge transport layer "buried" at the bottom of the channel. A hypothesis is that only the upper charge transport monolayer (out of the three monolayers involved) is affected by the increased density of domain boundaries when the film dewets/roughen, and by polarization effects to be ascribed to the small islands growing on top.

The next step after the bottom gate operation, was to measure the devices in an electrolytic environment. In EGOFET a different mechanism is taking place. As we can see here, the 3 nm thin film pentacene device does not appear in the graph, because in the electrolyte-gated the upper layer contributes to the charge transfer, so when the film is ultrathin, there is not a percolation channel for the carriers.

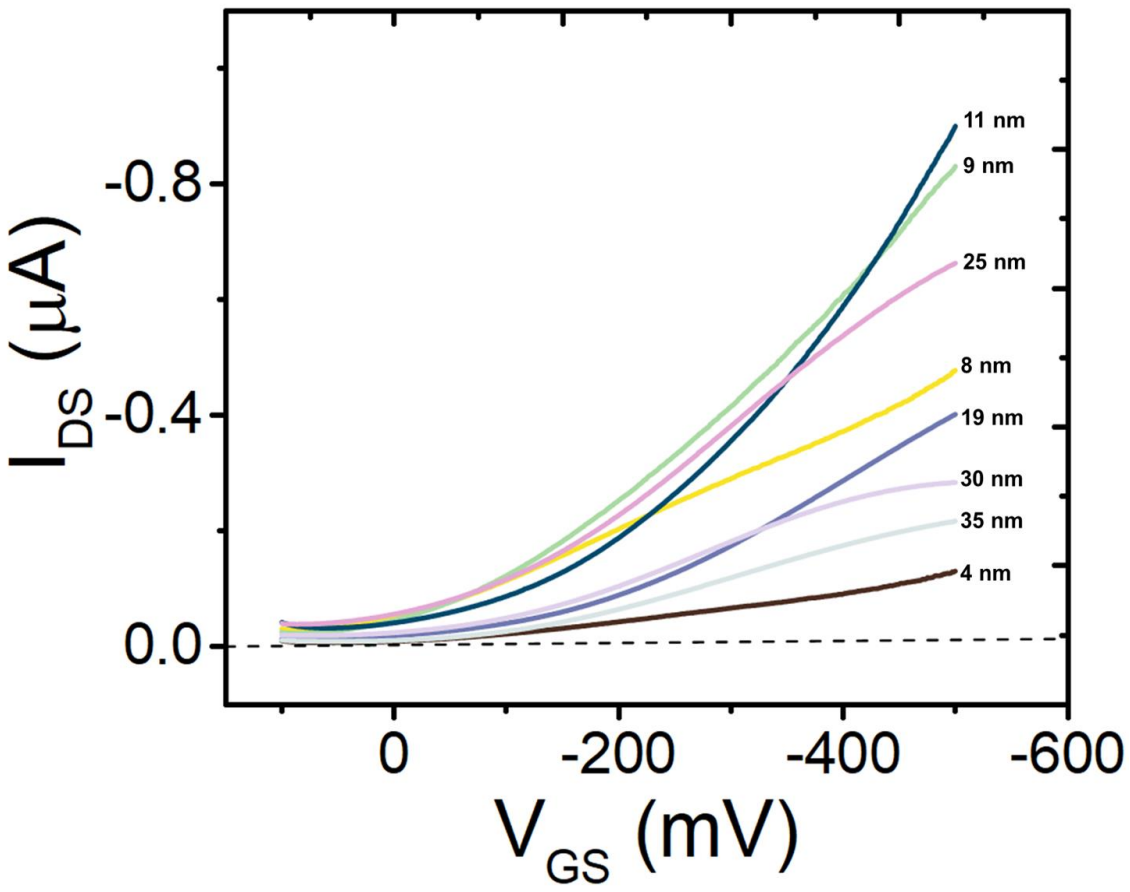

FIG. 4.6. Transfer characteristics of pentacene thin films at different thicknesses operating in [KCl]= 50 mM solution.

When the thickness is from 8 nm to 11 nm the device conducts and the maximum current increases. Of course, as we highlighted for the bottom gate operation, between this range of thicknesses that we measured there is not a monotonic correlation of the electrical response with the increase of the thickness. In EGOFETs where the upper layers are among the main contributors to the charge transport through the substantial ion exchange, the thicker films act like insulators, because these upper layers are nonetheless highly discontinuous. As we can observe from the transfer the maximum current is much lower in respect to thinner films, revealing the difficulty of the carriers to cross the conduction channel.

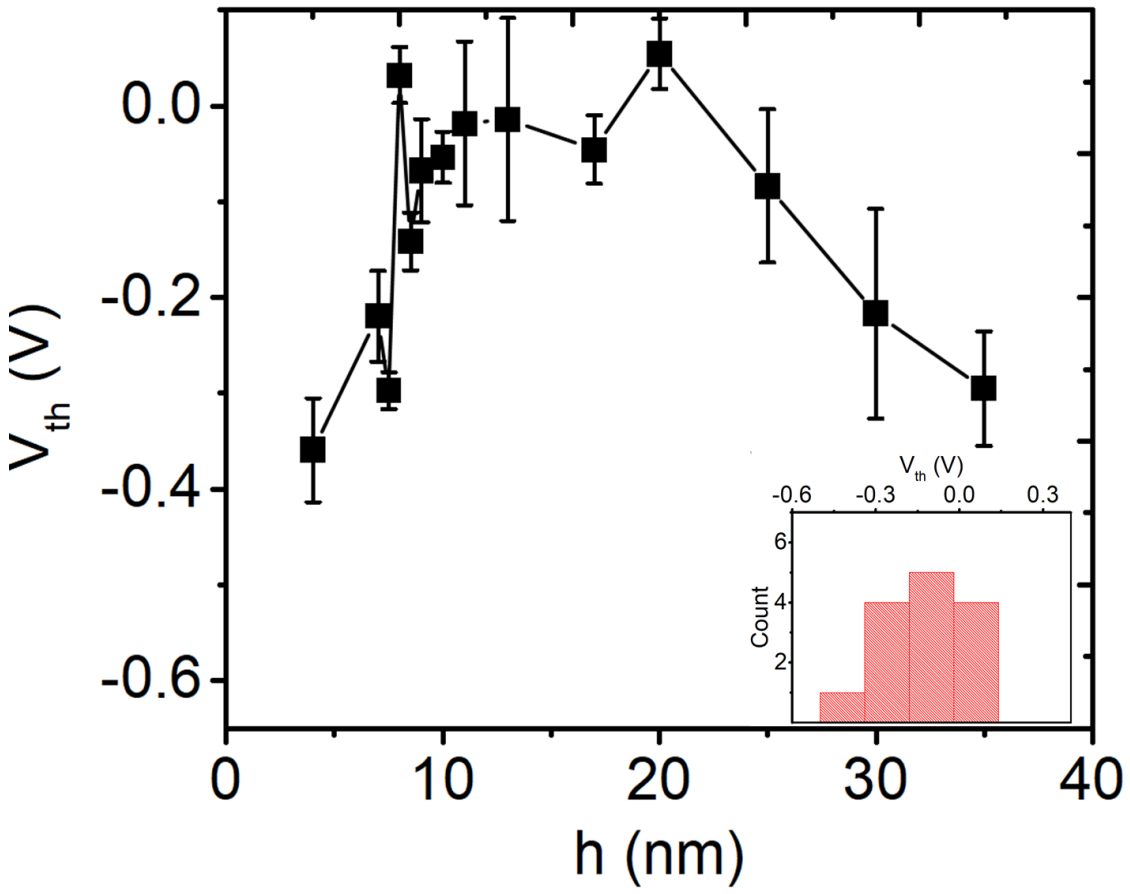

FIG. 4.7. Shows the threshold voltage vs thickness operating in electrolytic environment. Inset: histogram of the threshold voltage.

More electrical parameters were analyzed also in EGOFETs in order to understand better how the thickness of the film influences the electrical response. As we can see in Fig. 4.7, the $V_{th,}$ spreads according to a narrow mono-modal distribution vs thickness between -0.4 and 0.2 V and the peak around 0 V. When the thickness reaches 20 nm, the V_{th} seems to reach the maximum value. Taking into consideration this fact, there is a range of thicknesses in which the percolation channel is sufficient for the carriers to cross it.

As last parameter, we discuss the transconductance evolution vs thickness in Fig. 4.8. The g_m undergoes oscillations. This evidences the fact that electrolyte operations, that involve upper

pentacene monolayers that expose the largest area to the electrolyte, the surface morphology plays an important role.

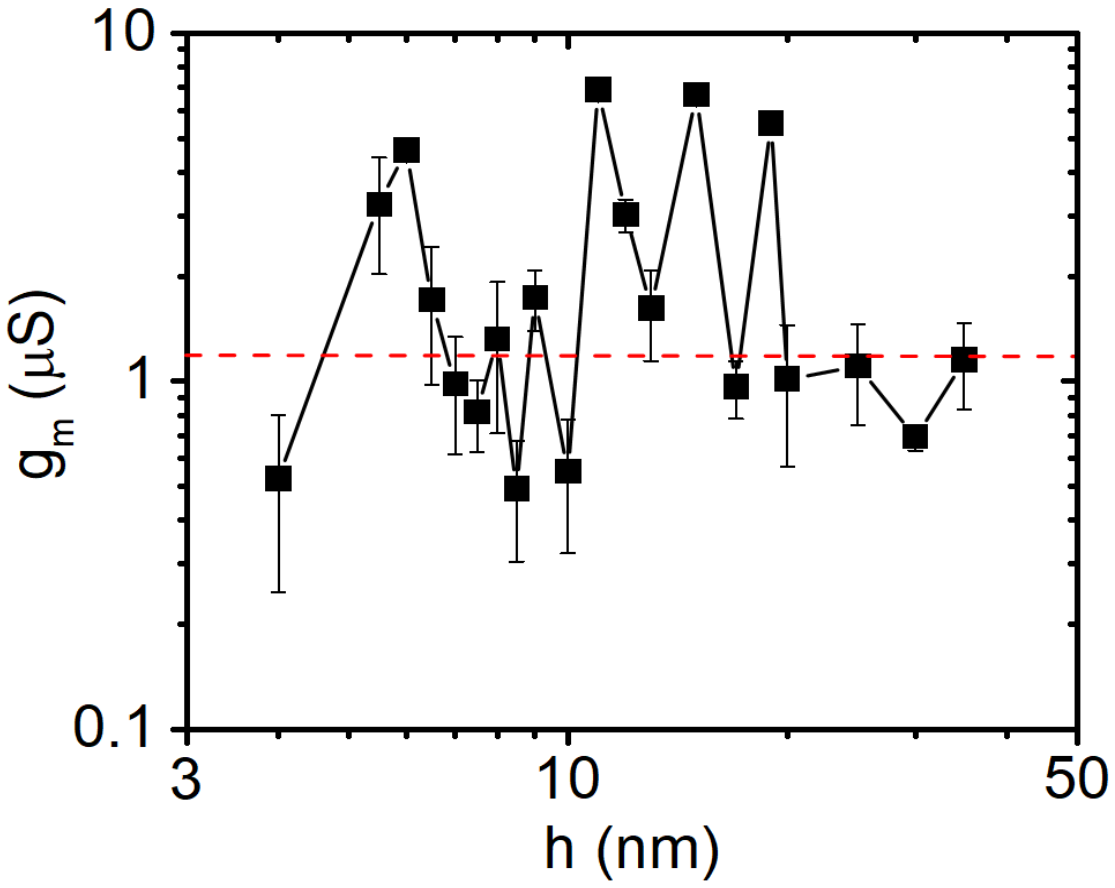

FIG. 4.8. Corresponds to the transconductance vs thickness of EGOFET. The dashed red line corresponds to the mean value of the transconductance.

In previous discussions we explained that the transconductance is based on the mobility of the material. The oscillations due to wetting/dewetting phenomenon observed by AFM and discussed in Chapter 3 clearly influence the transconductance of the EGOFET. More specifically, the devices with the highest transconductance, which correspond to the devices with the 6 nm, 11 nm, 15 nm, and 19 nm pentacene thin films, correspond to the morphology with large islands and small roughness. This suggests that the upper monolayers form in-plane percolative pathways that are effectively adding up and maximize the transconductance. At thicknesses where the roughness

reaches the maximum value, the carriers face a difficulty to cross the channel across continuous pathways and the transconductance tends to decrease.

The oscillations in Fig. 4.8 show very convincingly that the morphology affects the transconductance by modulating it up to one order of magnitude. This points to the fact that the control on film thickness and morphology must be the finest, as the periodicity of these oscillations are on the few nm scale. On the other hand, it is telling a new and to some extent unexpected outcome: by finely tuning the thickness, the transconductance can be enhanced up to one order of magnitude, thus making the EGOFET a potentially 10 times more sensitive device.

4.4 Discussion

With this work we studied the influence of the morphology, through the systematic variation of the thickness, on the electrical properties of pentacene thin film transistors. Electrical measurements were performed both in air and in electrolytic environment. The electrical properties of these devices show that the first pentacene monolayers are sufficient for the formation of the percolation channel. As the thickness increases, the probability of the charge to be transported in the channel becomes smaller. In aqueous medium, the transconductance becomes stable very soon at small thicknesses, which is possibly related to the fact that the percolation channel for the carriers is located at the surface of the organic semiconductor, meaning the interface with the electrolyte. The oscillations of the transconductance around the thickness independent mean value are up to one order of magnitude and are only modestly damped. Thus, when thickness is between a few up to 20 nm, the charge transport appears strongly correlated with the interfacial area. Importantly, we notice that the maxima occur for the smoother films with larger islands on top (wetting films) while is minimum on the rougher films with small islands. This means that the surface morphology modulates the charge transport all the way down to a charge transport layer which, however, remains stable and insensitive to thickness. We can envision this surface-sensitive layer to coincide with the thickness of the surface roughness. Beneath this fluctuating interface, a charge transport layer persists that remains stable and insensitive to thickness.

This observation in EGOFETs also hints to the fact that, albeit the sensitivity to morphology is mainly localized to the fluctuating interface, the whole film thickness is involved in the charge carrier modulation by the ions. The exception may be the films thicker than 20 nm, where perhaps the ion penetration is incomplete, or more likely the number of interconnected pathways is saturating. This supports the view of EGOFET and OECT as very much similar in the mechanism of "ion doping" across their volume and not only at the geometrical surface.

4.5 References

[1] S. Inal, J. Rivnay, A. O. Suiu, G. Malliaras, and I. McCulloch, Acc. Chem. Res. **51**, 1368 (2018).

[2] K. Hanya, Y. Onaru, and K. Harafuji, Solid. State. Electron. **156**, 62 (2019).

[3] H. Bässler, Phys. Status Solidi **175**, 15 (1993).

[4] M. C. J. M. Vissenberg and M. Matters, Phys. Rev. B **57**, 12964 (1998).

[5] H. Sirringhaus, P. J. Brown, R. H. Friend, M. M. Nielsen, K. Bechgaard, B. M. W. Langeveld-Voss, A. J. H. Spiering, R. A. J. Janssen, E. W. Meijer, P. Herwig, and D. M. de Leeuw, Nature **401**, 685 (1999).

[6] F. Dinelli, M. Murgia, P. Levy, M. Cavallini, F. Biscarini, and D. M. de Leeuw, Phys. Rev. Lett. **92**, 116802 (2004).

[7] T. Cramer, A. Campana, F. Leonardi, S. Casalini, A. Kyndiah, M. Murgia, and F. Biscarini, J. Mater. Chem. B **1**, 3728 (2013).

[8] J. T. Mabeck and G. Malliaras, 343 (2006).

[9] M. Berggren and A. Richter-Dahlfors, Adv. Mater. **19**, 3201 (2007).

[10] R. Giridharagopal, L. Q. Flagg, J. S. Harrison, M. E. Ziffer, J. Onorato, C. K. Luscombe, and D. S. Ginger, Nat. Mater. **16**, 737 (2017).

[11] M. Bianchi, S. Carli, M. Di Lauro, M. Prato, M. Murgia, L. Fadiga, and F. Biscarini, J. Mater. Chem. C **8**, 11252 (2020).

[12] A. Giovannitti, D.-T. Sbircea, S. Inal, C. B. Nielsen, E. Bandiello, D. A. Hanifi, M. Sessolo, G. Malliaras, I. McCulloch, and J. Rivnay, Proc. Natl. Acad. Sci. **113**, 12017 (2016).

[13] H. Klauk, M. Halik, U. Zschieschang, G. Schmid, W. Radlik, and W. Weber, J. Appl. Phys. **92**, 5259 (2002).

[14] A. A. Günther, J. Widmer, D. Kasemann, and K. Leo, Appl. Phys. Lett. **106**, 233301 (2015).

Chapter 5

Studying the mechanical properties of conductive and semi-conducting organic materials

"This chapter describes the application of Bimodal AFM on semiconductive and conductive organic materials. Pentacene thin films were analyzed, and the theory of bottom effect was applied. In addition, the local viscoelastic properties of PEDOT :PSS was measured under the application of voltage."

5.1 Introduction

Organic semi-conductive and conductive conjugate thin films have attracted tremendous attention because of their wide range of bioelectronic applications. [1–6] Atomic Force Microscopy (AFM) has known an extremely huge development in nanosciences and nanotechnologies over the past three decades. [7] More specifically, in polymer science the use of AFM is considered as key factor in the understanding and the characterization of the mechanical properties at nanoscale level. [8–11] Previous studies have shown that using bimodal AFM provides a precise and quantitative way for the characterization of organic self-assembling monolayers. [12] Moreover, it was shown that the substrate plays an important role in the study of the mechanical properties. When a thin, soft layer is deposited on a rigid substrate the force measured by the tip are influenced by the substrate itself. This phenomenon is called bottom effect artifact and different models have been developed trying to determine the unaffected Young's modulus, by removing the influence of the solid support. [12–15]

This work aims to study the mechanical properties of two different organic semiconductors on different substrates using bimodal AFM. More specifically, pentacene thin films on SiO_2 wafers deposited, as described before in section 2.3, as well as PEDOT:PSS electrodeposited electrodes on Quartz (more details about the technique in section 2.5). This chapter will explain the influence of the substrate on the Young's modulus on pentacene thin films. A bottom effect theory was applied to recover the unaffected Young's modulus. Moreover, we studied the voltage-dependent behavior of the mechanical properties of PEDOT:PSS films in an electrolyte solution. Results show that there is a change of the elastic properties due to the ion penetration in PEDOT:PSS films when the voltage is applied. All these experiments were carried out at the Instituto de Ciencia de Materiales de Madrid (ICMM) in Spain during my secondment at Prof. Ricardo Garcia's Forcetool group in collaboration with Simone Benaglia.

5.2 Experimental data

For the first set of experiments, as test pattern was used SiO_2 wafer which was cleaned using the standard protocol discussed in section 2.1.3. Pentacene is thermally sublimed in high vacuum (base pressure 2 x 10^{-6} mbar) onto the test pattern, with sublimation rate 0.1 Å/s. The thickness of the thin film was measured with a quartz crystal microbalance (QCM) and it was h = 1.5 nm. After the thin film deposition, the characterization with bimodal atomic force microscopy was carried out. The technique is explained in detail in section 2.6.2. The bimodal AFM measurements were performed using a Cypher S (Asylum Research Inc.) at room temperature ($T_{room} \approx 25$ °C) and in a N_2 atmosphere. Cantilevers PPP-NCHAuD (Nanosensors) with f_{01}= 303.451 kHz, k_1 = 43.97 N m^{-1}, Q_1 = 590.6, f_{02} = 1900 kHz, k_2 = 2354 N m^{-1} were used in this experiment.

For the second set of experiments, quartz crystal substrates were used. The substrates were dipped in pure acetone over a hot plate at 50°C for 15 min. After that, PEDOT:PSS was deposited on the top of the gold electrode through electrodeposition as described before (section 2.5). The thickness of the electrode was measured with AFM and it was around h = 160 nm. AFM operated in the amplitude modulated-frequency modulated configuration (AM-FM AFM) using a Cypher S (Asylum Research Inc.), was used to probe the mechanical properties of the film. For this measurement, as electrolyte an aqueous solution (0.05 M) of potassium chloride (KCl) with pH = 7.2 was used. The cantilever used for this experiment was PPP-NCHAuD (Nanosensors) with f_{01} = 646.595 kHz, k_1 = 46 N m^{-1}, Q_1 = 616.1, f_{02} = 2135 kHz, k_2 = 2376 N m^{-1}. Moreover, a study of the influence of the applied voltage on PEDOT:PSS films was occurred. Two biases (0 mV and 800 mV) were chosen and applied to the Pt electrode respect to the gold substrate in order to study the mechanical response of the conducting film.

5.3 Results

5.3.1 Young's Modulus of pentacene thin films: the role of the substrate

Bimodal AFM were first applied to 15 nm pentacene thin films. Image analysis were performed using Gwyddion free software and RStudio 1.1.423. [16] From the calibration method previously described in Section 2.6.2 the spring constant of the first and the second eigenmodes were extracted. In Fig. 5.1a the topography of pentacene thin film grown on SiO_2 is shown. Fig. 5.1b and c shows the second mode frequency shift and Young's modulus obtained through the bimodal characterization. In bimodal AM-FM the second mode frequency shift is directly proportional to the elastic response of the sample, thus Fig. 1a and b are very similar. It is possible to notice a smooth distribution of the frequency shift and the corresponding elastic modulus through the pentacene terraces. In literature previous studies have shown that the Young's modulus of pentacene thin films is around 15 GPa. [17]

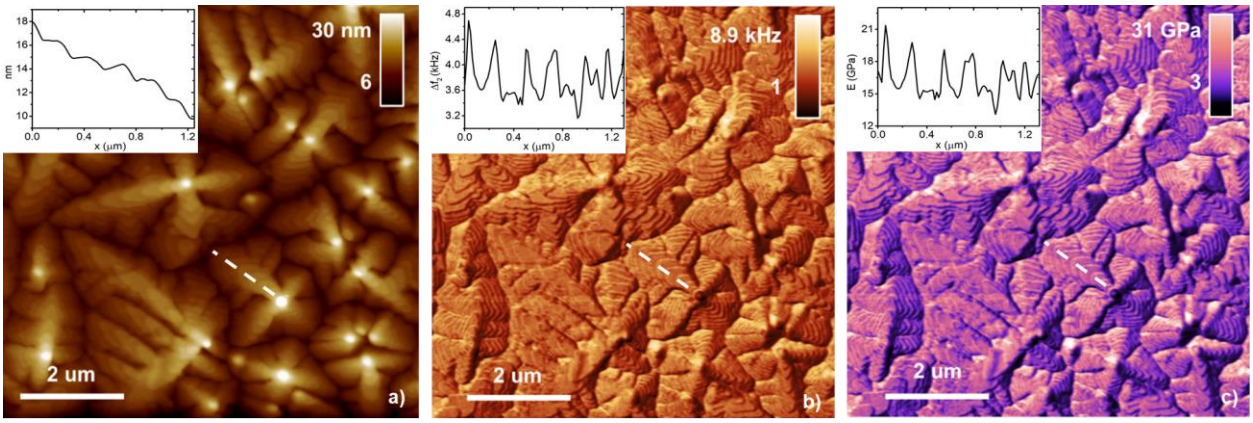

FIG. 5.1 Bimodal AFM maps on pentacene thin films. ***a)*** *Topography of 15 nm pentacene thin film deposited on* SiO_2. ***b)*** *Frequency* Δf_2 *that corresponds to the elastic response of the film* ***c)*** *Young's modulus map of pentacene thin film deposited on* SiO_2. *Insets correspond to the distribution of the height, the frequency shift, and the Young's modulus, respectively.*

For the calculation of the Young's modulus from the experimental results eq. 1 is considered. Equation 1 derives E^*, which is the effective Young's modulus of the pentacene, as a function of the Young's moduli and Poisson's ratios of pentacene thin films (E_{pen}, v_{pen}) and the substrate (E_{sub}, v_{sub}). The calculation of the Young's modulus which corresponds to the map (Fig. 1c) shows a homogeneous material characterized by E = 14.8 GPa, which agrees with literature values.

In the second case, a thinner pentacene thin film is grown on the SiO_2 and the influence of the substrate can be observed when the mechanical properties are probed. The nominal thickness of the pentacene thin film is h = 1.5 nm. In this case, we tried to apply to our data a simple bottom effect theory that previous studies applied for self-assembled monolayers [12]. The application of the bottom effect was used here, due to the low ratio between the thickness (few nanometers) and the indentation (around 1 nm). In order to be able to recover the actual viscoelastic parameters of thin films without having the influence of the rigid substrate, it necessary to control the ratio between the contact radius and the thickness of the film. [18].

The elasticity of the SiO_2 substrate, E_{sub}, was determined from the experimentally extracted value of E^*. The analytical expression for the reduced modulus is written to the following equation:

$$\frac{1}{E^*} = \frac{1}{2}\left[1 - v_{sub} + \left(v_{sub} - v_{pen}\right)\right] I_1 \times \left[\frac{2(1+v_{sub})}{E_{sub}} \times (1 - I_0) + \frac{2(1+v_{pen})}{E_{pen}} I_0\right] \quad (1)$$

Where I_0 and I_1 are weighting functions that corresponds to the shear modulus mismatch and to the Poisson's ratio effects, respectively. For the calculation the Poisson's ratio of the substrate, v_{sub} equals to 0.27, and for the pentacene film, v_{pen} equals to 0.35, according to literature values. [17,19]

For the weighting functions I_0 and I_1, eq. 2 and eq. 3 are written according to previous literature studies. [20]

$$I_1(\xi) = \frac{2}{\pi}\arctan\xi + \frac{\xi}{\pi}\ln\frac{1+\xi^2}{\xi^2} \quad (2)$$

$$I_0(\xi) = \frac{2}{\pi}\arctan\xi + \frac{1}{2\pi(1-v_{sub})} \times \left[(1-2v_{sub})\xi \ln\frac{1+\xi^2}{\xi^2} - \frac{\xi}{1+\xi^2}\right] \quad (3)$$

where ξ is the ratio between the thickness and the radius and v_{sub} is the Poisson's ratio of the substrate.

These calculations correspond to the case of a flat punch indenter. In our experiments a paraboloid-shaped cantilever is used. In order to able to extract the right values a correction factor was applied according to the literature. [12]

Bimodal AFM maps of the pentacene thin films is shown in Fig. 5.2. Both Fig. 5.2b and Fig. 5.2c represent the topography and the (normalized) elastic maps of the sample with and without the substrate effect correction, with cross sections along different layers.

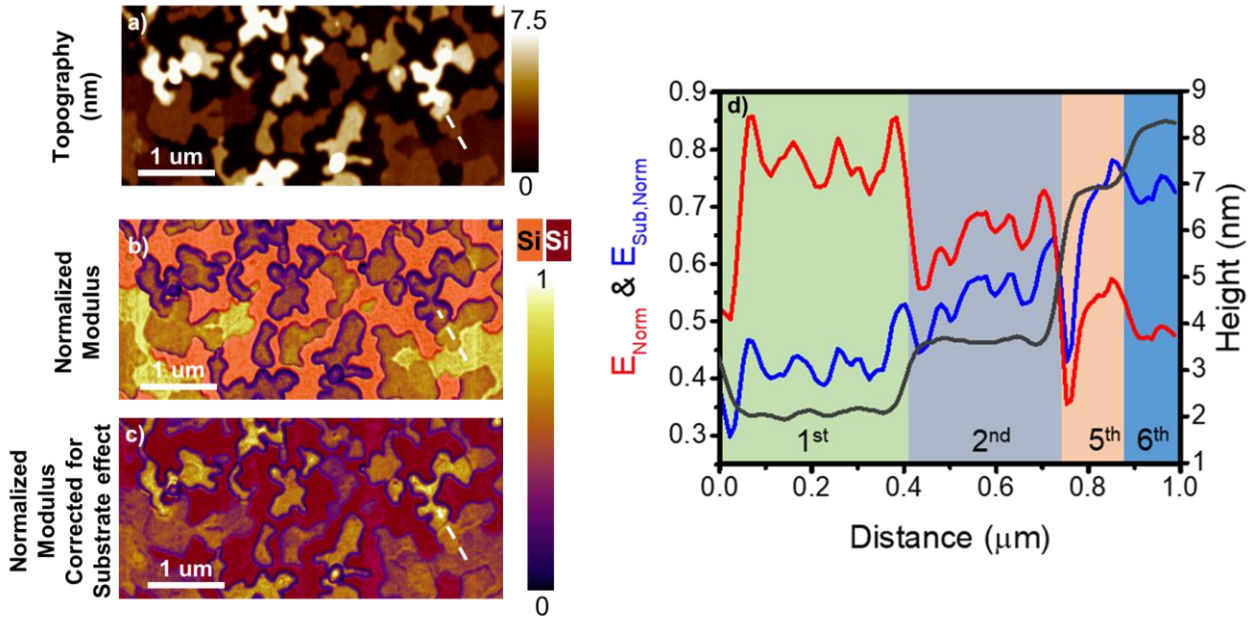

FIG. 5.2 ***a)*** *Topography of 1.5 nm pentacene thin film deposited on* SiO_2. ***b)*** *Normalized Young's modulus* ***c)*** *Normalized Young's modulus corrected by the substrate effect.* ***d)*** *Representation of heights and the elastic moduli. Black corresponds to the height of the topography. Red corresponds to the normalized modulus and blue to modulus corrected by the substrate effect.*

Fig. 5.2d shows the overlap of the cross sections for the three maps. The corrected Young's modulus map shows an inverted trend respect to the not corrected one. It is clearly shown that the elastic modulus without the application of the substrate effect (red line) tends to lower the higher is the layer. This is a typical effect of the substrate that diminishes the thicker is the sample (considering a more or less constant indentation). Thus, the stiffness of the substrate is relevant in these measurements, respect to the ones done at higher thickness (i.e., Fig. 5.1). When the theory is applied the elastic modulus changes and the data corresponds to the normal behavior (blue line). Thus, the first layers correspond to a Young's modulus lower respect to higher layers and it is attributed to a softening of the material near the free surface.

5.3.2 Ion penetration in PEDOT:PSS electrodes

Here, bimodal AM-FM was used for mapping the mechanical properties of PEDOT:PSS. The preparation of the polymer was done through electropolymerization and deposited on the top of the gold electrode as it is described in section 2.5. In order to estimate the swelling of the PEDOT:PSS, cross section profiles of the bare and covered electrode (in dry and wet conditions) were measured as shown in Fig. 5.3.

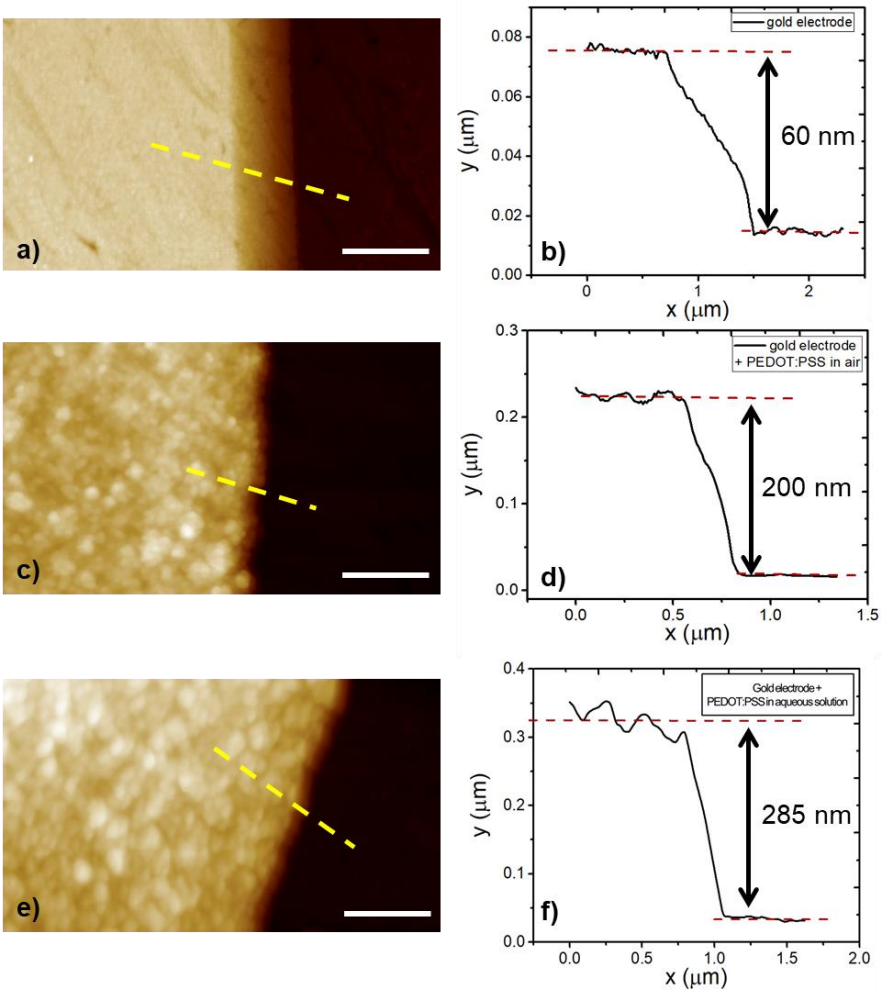

FIG. 5.3 Topography images of gold electrode and PEDOT: PSS. Scale bars, 1 μm; ***a)*** *Cross section of the gold electrode* ***b)*** *Profile of the gold electrode* ***c)*** *cross section of gold electrode covered by PEDOT: PSS measured in air* ***d)*** *Profile of the gold electrode covered by PEDOT:PSS* ***e)*** *cross section of gold electrode covered by PEDOT:PSS measured in aqueous solution* ***d)*** *Profile of the gold electrode covered by PEDOT: PSS measured in aqueous solution.*

First, the topography (Fig. 5.3a) shows the bare gold electrode over the quartz substrate which, as it is calculated, corresponds to a height equal to 60 nm (Fig. 5.3b). After the deposition of the PEDOT: PSS film (Fig. 5.3c) the height of the film was around 200 nm (Fig. 5.3d). The topography of the film was taken in dry environment (N_2 atmosphere). As last step, a droplet of 30 μl of solution was added at the top of the PEDOT: PSS and left it for around 1h in order to ensure the

wetting of the film. The topographic image (Fig. 5.3e) with the corresponding profile (Fig. 5.3f) show that after 1 h in aqueous solution an increase on the thickness is observed which corresponds to the 60% from the initial value.

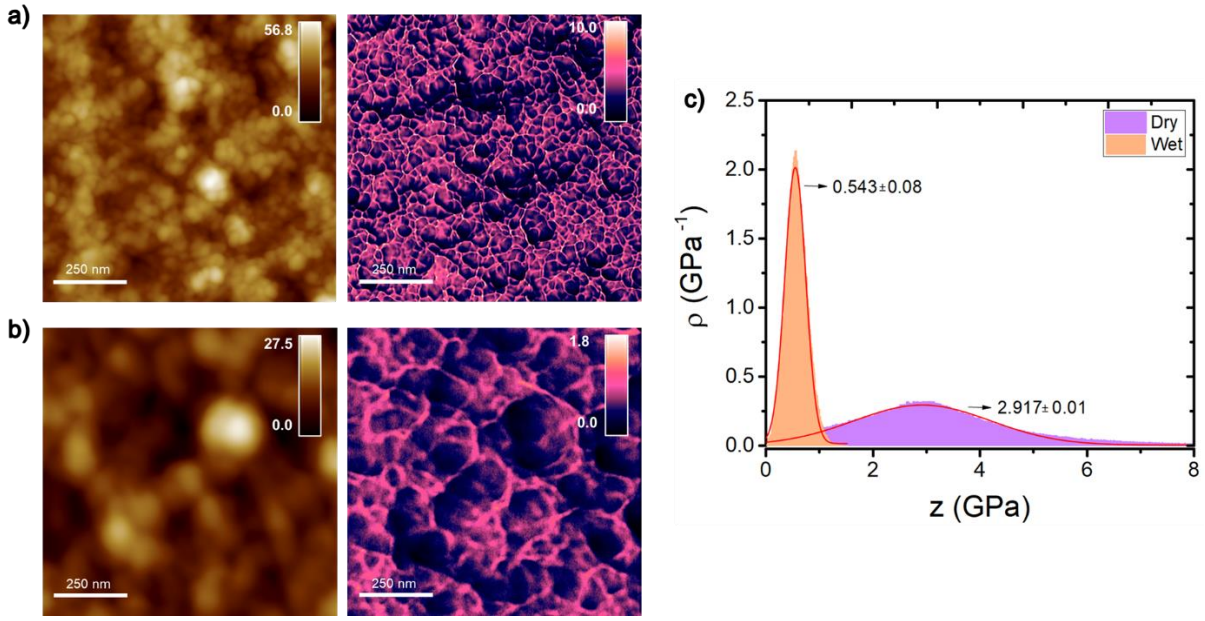

FIG. 5.4 ***a)*** *Topography images of PEDOT: PSS in dry condition with the corresponding map of the Young's modulus* ***b)*** *topographic map of PEDOT: PSS taken after 1h in aqueous solution with the corresponding Young's modulus* ***c)*** *Histogram of the Young's modulus obtained from PEDOT: PSS in dry and in water environment.*

After the swelling of the polymer, the study of the mechanical properties was performed. Bimodal AFM was applied on PEDOT: PSS in air and in electrolytic environment. Starting with the measurements in dry conditions, in Fig. 5.4a is shown the topography as well as the Young's modulus of PEDOT: PSS. Local changes in the elastic modulus can be observed especially in the regions between the grains. On the other hand, measurements in liquid shows different results. The film was left in electrolyte solution about 1 hour in order to be hydrated. Nanomechanical maps were extracted as shown in Fig. 5.4b and then, were compared with the dry conditions. In Fig. 5.4c the histograms from the two Young's modulus are represented. It is clearly shown that there is a

big change of the Young's modulus before and after the hydration of the film. The value of the elastic modulus of the dry and the wet film corresponds to 2.91 ± 0.01 GPa and 0.54 ± 0.08 GPa, respectively. This decrease of the Young's modulus corresponds to 18% for the initial value. In aqueous solutions a parameter that can contribute to the extensive swelling and explain our results is the osmosis effect [21].

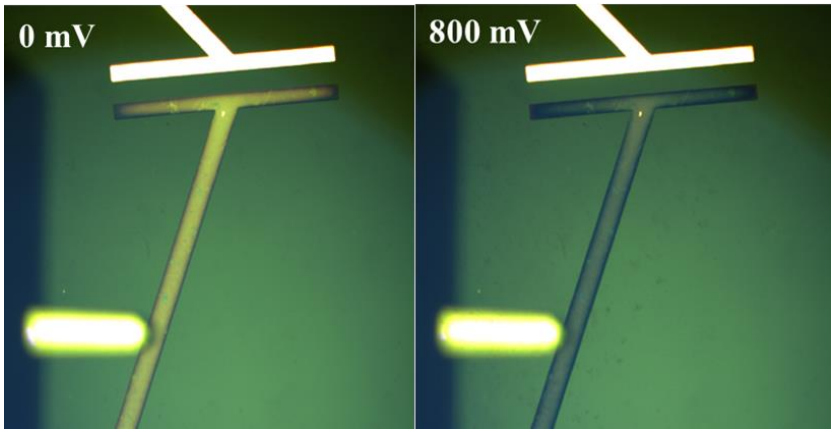

FIG. 5.5 Microscope images from electrochemical switching of PEDOT: PSS applying different bias on the electrode coved by PEDOT: PSS (black electrode), 0 mV and 800 mV.

Another study which took place was to study the influence of the electrolyte solution on such a porous polymer like PEDOT:PSS, while a voltage was applied during the measurement. A Pt electrode and the conductive film were connected directly to a Keithley 4200 and the voltage was applied to the Pt electrode while the Bimodal measurements were occurred. In Fig. 5.5 an experimental test was done in order to verify the connections. When the applied voltage is changed, an electrochemical switching is observed to the PEDOT:PSS due to the reduction of the film, which can be appreciate from the color change of the film. [22] Fig. 5.6 shows the maps of the Young's modulus and the phase shift acquired simultaneously with the topography. The Young's modulus (Fig. 5.6b) reveals a homogenous distribution of the elastic properties across the polymer.

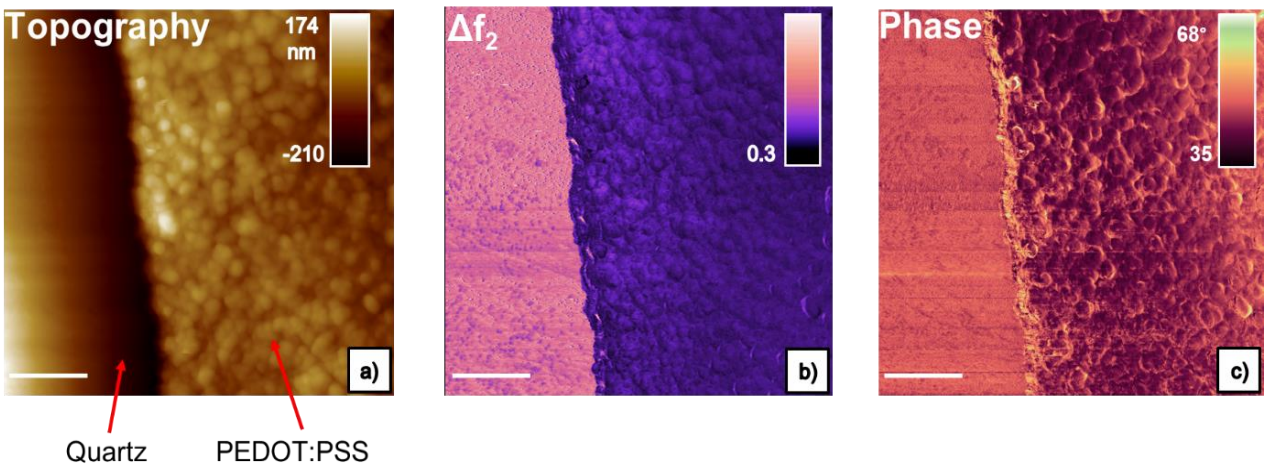

FIG. 5.6 Bimodal AFM maps on PEDOT:PSS film in liquid environment; ***a)*** *Topographic images of PEDOT:PSS;* ***b)*** *Frequency shift Δf_2 that corresponds to the elastic response of the film* ***c)*** *Phase channel; Frequency shift and phase are used for the Young's modulus calculation; Scale bars, 1 μm.*

After testing the contact, the study of the behavior of the ions when are injected inside the channel, was performed. Starting from 0 mV, we applied a continuous changing of the voltage from 0 mV to 800 mV. The experiments with the voltage change were occurred after that the polymer was left for 1 h to be hydrated. The variation of the voltage was occurred every two minutes in order to leave to the polymer time to respond. PEDOT:PSS is a heavily doped p-type polymeric semiconductor that, when used as the active channel, gives rise to a "normally on" transistor-like behavior. As the transistor works in depletion mode, reduction of the transistor current occurs when setting the electrolyte to positive potential with respect to the PEDOT:PSS channel. In this way, mobile positive carriers in the p-type semiconducting polymer PEDOT are reduced and cations from solutions migrate into the film to compensate sulfonate anions on the PSS chain, which play the role of acceptors. Only a fraction of sulfonate anions is compensated by holes due to the fact that PSS is added in excess. Hence, these anions contribute to the ion injection. According to previous studies, the time that the ions need to enter in the semiconductor is scales in the order of seconds. [23] In Fig. 5.7 is shown the first two representative nanomechanical maps

of PEDOT: PSS under the voltage application. A small change is observed (yellow box) when 800 mV is applied due to the reduction of the elastic modulus of the film.

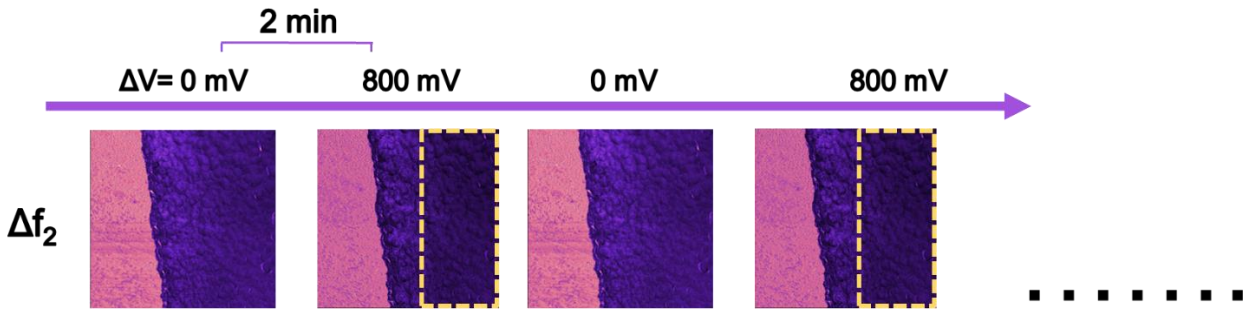

FIG. 5.7 represents the frequency shift map of PEDOT: PSS during the alternation of the applying voltage from 0 mV to 800 mV, respectively.

A correlation of the normalized modulus and the thickness with the alternation of the voltage are shown in Fig. 5.8. For this reason, the data that are presented corresponds to normalized values (normalized respect to the maximum value of the measurement). This allows us to underline the variation of the Young's modulus when the voltage is applied. In the first plot (Fig. 5.8a), a decrease of the elastic modulus is observed around a value equal to 70% of the initial value with the change of the voltage. At the same time, we record an increase of the thickness of the polymer film.

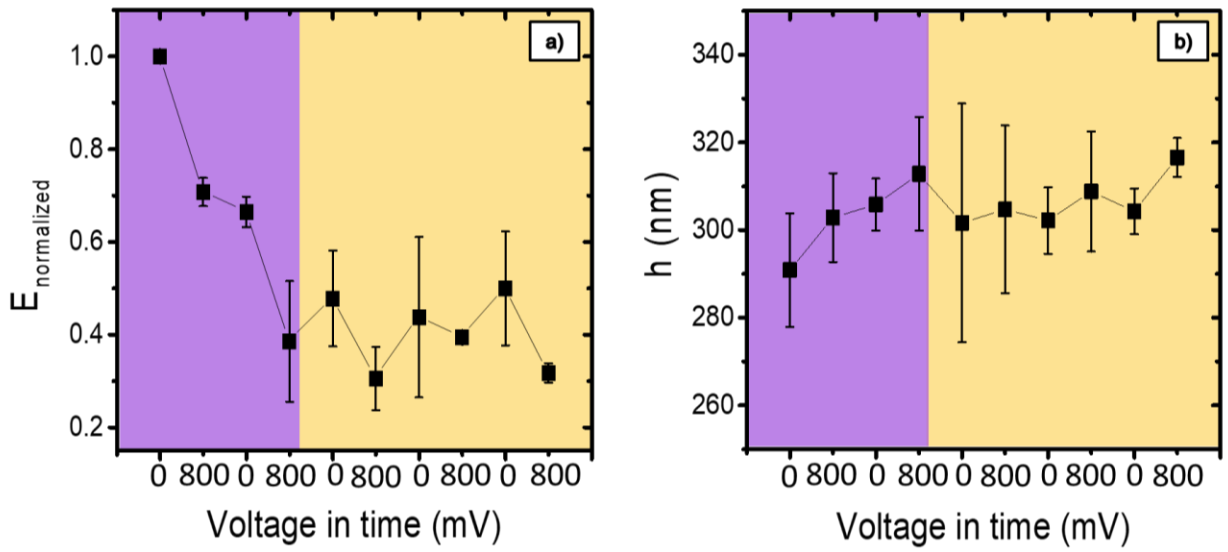

FIG. 5.8 ***a)*** *shows the evolution of the normalized Young's modulus versus the alternation of the voltage* ***b)*** *represents the change at the thickness while a voltage is applying.*

This decrease of the Young's modulus and swelling of the film could be explained by the ion penetration into the conductive film. Previous results have shown the ion penetration into polymeric films rules the electrical properties of the conductive film [24,25]. When the first bias is applied the injected cations compensate the sulfonate acceptors and lead to hole depletion, eventually forming the percolation channel. After the first cycle, when 0 mV is applied, we expect that the system would try to return to the previous situation and restore the Young's modulus value. But the Young's modulus (Fig. 8a) does not seem to change, though it lowers. This happens in the second cycle of measurement (purple region), until it stabilizes (yellow region) and higher modulus values alternates (0 mV) to lower modulus values (800 mV). It is important to underline that the Young's modulus value has lowered down to 30% - 40% of its initial value. A similar trend can be found for the thickness behavior (Fig. 8b).

Comparing these two graphs, it can be observed that when a bias is applied, and the ions start to enter in the conductive film the channel opens and lets the ions crossing the film. This is shown also from the decrease of the elastic modulus as well as the increase of the thickness. The formation of the percolation channel permanently modifies the elastic properties of the sample. Even when the bias drives the ions out of the polymer, a complete recover of its mechanical properties is not

recorded. Also, the osmosis effect contributes to this extensive swelling. Thus, when the channel is open the ions can go in and out and only a small change of the elastic modulus and the thickness is seen. This phenomenon can be considered as the real ion penetration effect to the mechanical properties of the open polymer film (this is the condition at which a PEDOT:PSS film is usually used for organic electronic in electrolyte solution). The aqueous environment can influence the elastic behavior of the film. The water drift in and out of the film influence the device performance.

Changes in film morphology, for example, are expected upon injection of ions and this certainly affects material properties. Trying to understand the mechanical properties of the PEDOT:PSS especially the local changes will help to understand better the charge transport across the conductive and semiconductive films.

5.4 Discussion

In this chapter, it was tried to study the mechanical properties of different kinds of organic electronic materials through Bimodal AFM. Firstly, the study was focused of pentacene thin films. As it was observed, the extraction of the nanomechanical maps was influenced by the substrate. The bottom effect is a phenomenon which can influence the data and it was previously introduced to analyze biological samples and self-assembly of organic materials. In this study a very thin film was characterized, and a simple theory was applied to the extracted data. In order to verify the data, nanomechanical mapping of a thicker pentacene film were performed. The maps shown a homogeneity on the mechanical properties of the film, fact that confirms the influence of the substrate to the thin films. Further studies on the application of more advanced substrate effect theories will enable us to better analyze this effect. We foresee its application on organic thin films which will help to acquire more reliable data.

Secondly, bimodal AFM was applied to PEDOT:PSS in an electrolytic environment while a voltage was applied. Measurements both in air and in liquid environment were performed in order to measure the swelling of the polymer. From these measurements apart from the swelling of the film, Young's modulus change was shown corresponding to a value equal to 18% of its dry value. When the voltage was applied, it was observed the decrease of the elastic modulus and after that

its stabilization. This fact could be described in the following way: first the carriers try to form a percolation channel when the first bias is applied; this channel remains open for the next carriers (even when no voltage is applied) and at this point the mechanical properties are not restored to the initial values.

Bimodal AFM could be a powerful tool in organic electronics. More specifically, it provides the potential to study in real time the local nanomechanical properties of semiconductive polymers. Thus, understand the nanomechanical conformation of the semiconductive films when ions penetrate inside the film. Apart from the hydrophobic materials such as pentacene, this technique could be applied to hydrophilic materials or other derivatives helping in this way to understand the charge transport in organic thin films.

5.5 References

[1] S. Wang, J. Xu, W. Wang, G. J. N. Wang, R. Rastak, F. Molina-Lopez, J. W. Chung, S. Niu, V. R. Feig, J. Lopez, T. Lei, S. K. Kwon, Y. Kim, A. M. Foudeh, A. Ehrlich, A. Gasperini, Y. Yun, B. Murmann, J. B. H. Tok, and Z. Bao, Nature **555**, 83 (2018).

[2] D. Khodagholy, J. N. Gelinas, T. Thesen, W. Doyle, O. Devinsky, G. Malliaras, and G. Buzsáki, Nat. Neurosci. **18**, 310 (2015).

[3] M. Giordani, M. Di Lauro, M. Berto, C. A. Bortolotti, D. Vuillaume, H. L. Gomes, M. Zoli, and F. Biscarini, Org. Sensors Bioelectron. IX **9944**, 99440P (2016).

[4] M. Berto, C. Diacci, L. Theuer, M. Di Lauro, D. T. Simon, M. Berggren, F. Biscarini, V. Beni, and C. A. Bortolotti, Flex. Print. Electron. **3**, 024001 (2018).

[5] Z. Bao, MRS Bull. **41**, 897 (2016).

[6] S. C. B. Mannsfeld, B. C. K. Tee, R. M. Stoltenberg, C. V. H.-H. Chen, S. Barman, B. V. O. Muir, A. N. Sokolov, C. Reese, and Z. Bao, Nat. Mater. **9**, 859 (2010).

[7] G. Binnig, C. F. Quate, and C. Gerber, Phys. Rev. Lett. **56**, 930 (1986).

[8] H. K. Nguyen, M. Ito, and K. Nakajima, Jpn. J. Appl. Phys. **55**, (2016).

[9] R. Proksch, M. Kocun, D. Hurley, M. Viani, A. Labuda, W. Meinhold, J. Bemis, R. Proksch, M. Kocun, D. Hurley, M. Viani, A. Labuda, W. Meinhold, and J. Bemis, **134901**, (2016).

[10] R. García, R. Magerle, and R. Perez, Nat. Mater. **6**, 405 (2007).

[11] D. Wang and T. P. Russell, (2018).

[12] E.-N. Athanasopoulou, N. Nianias, Q. K. Ong, and F. Stellacci, Nanoscale **10**, 23027 (2018).

[13] P. D. Garcia and R. Garcia, Biophys. J. **114**, 2923 (2018).

[14] E. K. Dimitriadis, F. Horkay, J. Maresca, B. Kachar, and R. S. Chadwick, Biophys. J. **82**, 2798 (2002).

[15] B. L. Doss, K. Rahmani Eliato, K. Lin, and R. Ros, Soft Matter **15**, 1776 (2019).

[16] D. Nečas and P. Klapetek, Open Phys. **10**, (2012).

[17] D. Tahk, H. H. Lee, and D.-Y. Khang, Macromolecules **42**, 7079 (2009).

[18] P. D. Garcia and R. Garcia, Nanoscale **10**, 19799 (2018).

[19] J. Kim, D. Cho, and R. S. Muller, in *Transducers '01 Eurosensors XV* (Springer Berlin Heidelberg, Berlin, Heidelberg, 2001), pp. 662–665.

[20] H. Xu and G. M. Pharr, Scr. Mater. **55**, 315 (2006).

[21] A. Savva, C. Cendra, A. Giugni, B. Torre, J. Surgailis, D. Ohayon, A. Giovannitti, I. Mcculloch, E. Di Fabrizio, A. Salleo, J. Rivnay, S. Inal, A. Savva, C. Cendra, A. Giugni, B. Torre, J. Surgailis, and D. Ohayon, (2019).

[22] J. GUSTAFSSON, B. LIEDBERG, and O. INGANAS, Solid State Ionics **69**, 145 (1994).

[23] E. Stavrinidou, P. Leleux, H. Rajaona, D. Khodagholy, J. Rivnay, M. Lindau, S. Sanaur, and G. G. Malliaras, Adv. Mater. **25**, 4488 (2013).

[24] L. Q. Flagg, R. Giridharagopal, J. Guo, and D. S. Ginger, Chem. Mater. **30**, 5380 (2018).

[25] R. Giridharagopal, L. Q. Flagg, J. S. Harrison, M. E. Ziffer, J. Onorato, C. K. Luscombe, and D. S. Ginger, Nat. Mater. **16**, 1 (2017).

Chapter 6

Conclusions and Outlook

Conclusions

The main goal of this thesis was to understand the influence of the morphology on the transport of the charge carriers. Morphology is an important parameter for the performance of Organic Field Effect Transistor in solid state operation and in electrolyte. Understanding the growth mode of organic semiconductive materials but also how this growth influences the electrical properties of the organic transistors is very important. Scanning Probe Microscopies have given rise to investigate a lot of different properties of the organic materials such as electrical, mechanical, and chemical. For this work Atomic Force Microscopy was used for the analysis of the morphology of the semiconductor. The second part of this thesis was based in bimodal application on semiconductive and conductive organic materials in order to study the viscoelastic properties.

The first chapter served as an introduction to organic semiconductors but also to their growth modes. Moreover, the mechanisms of charge transport were also discussed and analyzed as well as the working principle of the organic transistors. Additional definitions of the of wetting/dewetting phenomena was introduced in order to be comprehensible the scientific achievements of this thesis.

The second chapter was based on the materials and methods that was used in this thesis. A descriptive report about test patterns and data analysis as well as the extraction and the definition of all the parameters that referred was presented. A very important mention was the explanation of the Atomic Force Microscopy technique as well as of the bimodal AFM which was part of the main training during this thesis.

In the chapter three, a study of different thicknesses of pentacene thin films was studied. Atomic force microscopy was used for the topographical analysis of the surface. After the statical analysis that was carried out a new study was came to the light. The evolution of the roughness as the thickness increases exhibits an oscillatory behavior. This behavior which seems to be repeated for the fact that the measurements was carried out also to a second batch of the same thickness. These observed oscillations are distinctively different from the commonly observed growth transition from layer-by-layer to self-affine island growth occurring at a critical thickness of a few monolayers in most of molecular organic semiconductor thin films Apart from the roughness the

correlation lengths exhibit the same oscillatory behavior. The correlation lengths were in antiphase with the roughness, hence, where there were the maxima of the roughness, the correlation lengths reached the minimum values. An analytical heuristic equation was presented, trying to depict these oscillations of the roughness. This phenomenon appears as a novel mechanism of wetting/dewetting transition occurring in a dynamic system. this kind of growth retains a memory of dewetting at the first monolayers which is repeated at larger thicknesses.

The correlation of the morphology of the pentacene thin films with the electrical properties of the organic field effect transistors operating in solid state and in electrolytic environment was carried out. In solid state operation the percolation channel is formed from the first monolayers. The "saturation of the response vs film thickness" is confirmed here, since the charge transport is located at the first monolayers but also, that the dewetting of the upper layers, which prevents the charge transport across the channel. In electrolytic environment, the transconductance becomes stable very soon at small thicknesses, which is possibly related to the fact that the percolation channel for the carriers is located at the surface of the organic semiconductor, meaning the interface with the electrolyte. At high thickness, the charge transport appears strongly correlated with the interfacial area. Another important thing is that the maxima of the oscillations occur for films which correspond to larger islands on top (wetting films) while the minima on the rougher films with smaller islands (dewetting films). An important hint is that the charge accumulation and ion doping always involve the deeper monolayers which are in contact with the substrate and that the dewetted portion of the film is electrostatically coupled to this deep charge carrier accumulation layer. This present work evidences the possibility of multiple critical transitions during the thin film growth, fact that may change this simpler scenario and may impact in technology and optimization of device properties.

The fifth chapter is devoted to bimodal application for studying the viscoelastic properties of semiconductive and conductive. Topographic images of two pentacene -a thick and a thin- films were studied. The analytical topography and Young's modulus maps were characterized. At thicker pentacene film a homogeneous distribution of the viscoelastic properties reveals the homogeneous distribution of the elastic modulus through the surface. On the other hand, the same experiment was carried out on a thin pentacene film in which the influence of the substrate was

observed. Bottom effect theory was applied, and the resulting data corresponded to the normal behavior. Hence, the rigid substrate is relevant to the extraction of the mechanical properties of thin films which grown on them. Another application of bimodal AFM was to study the viscoelastic properties of conductive film under biasing. The Young's modulus was calculated before and after the swelling of the polymer. Measurements during voltage application were carried out and the behavior of the elastic modulus started to decrease explaining the ion penetration into the polymeric film. After the continuous alternation of the voltage the changes on the mechanical properties of the film are less evident. This means that the percolation channel is formed and remains open until the next carriers even when no voltage is applied, there is not a complete recover of the elastic properties. Bimodal AFM is a dynamic tool for studying in real time the mechanical properties of conductive and semiconductive materials and could be applied to other materials in order to understand the fundamental processes of charge transport in organic thin films.

In conclusion, scanning probe microscopies provide the possibility to understand and correlate different kinds of phenomena. For this thesis, Atomic Force Microscopy has played an important role for the study of thin film growth. The advantage of looking at the nanoscale, brought into light a new phenomenon of thin film growth. This oscillatory behavior of the roughness and the correlation length with the increase of the thickness influences electronic properties of the active layer in OFET devices (i.e., threshold voltage and transconductance). We think that new opportunities arise for the optimization of electrical characteristics of organic field effect transistors operated in air and liquid environment.

Publications

- Michele Di Lauro, Carlo A. Bortolotti, Valerio Beni, Vitaliy Parkula, **Sofia Drakopoulou**, Martina Giordani, Marcello Berto, Francesco Milano, Tobias Cramer, Mauro Murgia, Angela Agostiano, Gianluca M. Farinola, Massimo Trotta, Fabio Biscarini, A Bacterial Photosynthetic Enzymatic Unit Modulating Organic Transistors with Light. *Adv. Electron. Mater.* 2020, 6, 1900888.

- **Sofia Drakopoulou**, Simone Benaglia, Mauro Murgia, Cristiano Albonetti, Francesco Borgatti, Michele Di Lauro, Michele Bianchi, David Papo, Ricardo Garcia, Andrea Alessandrini, Fabio Biscarini, Oscillating Wetting/Dewetting Transitions in Organic Semiconductor Thin Films, *in preparation.*

Acknowledgments

This thesis would not have been possible without the help and the support of different people that helping me to arrive successfully at the end of this journey.

A special thanks to my supervisor Prof. Biscarini that gave the opportunity to start my PhD in his laboratory, for his supervision and all the guidance and the knowledge that he transmitted to me. To Prof. Riccardo Garcia that I had the chance to collaborate with him during my secondment in Madrid and learn new techniques in these five months.

All these experiences could not be able without this European project that supported my research. I am thankful being a Marie Curie Sklodowska Fellow and especially being part of SPM 2.0 training network that gave me the chance to work on different places, collaborate with other researchers and providing all this training during these years.

I would like to thank all my colleagues Martina, Marcello, Matteo, Kateryna, Pamela and Michele in LEO lab UNIMORE for the insightful comments and the scientific discussions that we had in the lab as well as all the help that they gave to me.

To Simone for all his help and support as a friend but also as a brilliant researcher and also the great time that we had together both in Madrid and Italy.

To CNR- Bologna and particularly to ISMN that hosted me for my experiments as well as Mauro for his training to the vacuum systems.

To Italian Institute of Technology (IIT) in Ferrara for allowing using their laboratory.

I would like also to thank Nadja and Chiara for all their help in the administrative stuff.

To my whole family my mom, my dad, my brother, and my uncle for their support from Greece. A particular thanks to my friends Maria and George for the constant help and for all the time that we were speaking and for the unforgettable moments through skype calls.

To Vassia, Stavrina and Joanna for being with me all these three years hearing all my complains but also be grateful for all these happy moments that we spent together in Italy by exploring new places and finally to my friend Polina that we spent together one wonderful month in Madrid.

Activities during the PhD Thesis

Throughout these three years writing and doing research for my PhD, I realized that I gained a lot of experience as well as knowledge that makes me able to carry out research with large independence and increased confidence on my initiative and performance. During the PhD, several of my goals were accomplished. My main goal was to study the fundamental principles regarding generation and transport of charge carriers. I worked on the deposition, the patterning, the morphological and the electrical characterization of the organic transistors based on pentacene thin films. The organic semiconductor was sublimed in the channel using organic molecular beam deposition (OMBD). I learnt how to operate this sophisticated Ultra-High Vacuum deposition technique independently now. I also learnt characterization techniques such as Atomic Force Microscopy (AFM) as well as electrical measurements of transistors in air and in electrolytes. My main goal was to understand the influence of thickness, a parameter known to be central in determining the thin film morphology, of pentacene channels on the electrical properties, like transconductance and threshold voltage, in field effect transistors operated in air and electrolytes. The main result of my work is the discovery of a novel growth mode characterized by continuous wetting/dewetting which is superimposed to the conventional self-affine growth. This is subject of a paper in preparation for PRL. Moreover, a collaboration of my group with university of Bari led to a new publication with my contribution to the AFM characterization.

New collaborations through the Scanning Probe Microscopies 2.0 (SPM 2.0) network started thanks to my involvement. During my secondment in ICMM institute I had the opportunity to learn advanced AFM techniques as well as apply them to my project. Moreover, I received training and got involved in dissemination and communication activities, including written and oral ones, and very importantly on how to plan and workout a scientific manuscript. I learnt the importance of communicating the results of my work through the research community. Management, leadership, and communication skills are some of the qualifications that I gained through the Marie Curie Research Training Network (RTN), which will be critical to my success as a principal investigator.

General training in a range of areas including communication skills, information technology and career development were obtained by attending courses and seminars offered by the University of

Modena and Reggio Emilia as well as by the Marie Curie Training Network (RTN). In addition, collaboration with other institutions in the network were done, acquiring like newer ideas as well as learning how to expand the research network and combine the different techniques. Finally, a big advantage of learning the Italian and Spanish language, optimize the English language through the secondments provided by the RTN.

The network brings together experts from across Europe, who share a common interest in understanding and improving Scanning Probe Microscopies techniques. The research network is multidisciplinary. Chemistry, physics, biochemistry, material science, engineering and companies are combined in order to give to the researchers the equipment to fulfil their goals. The mobility of researchers between centers was inevitably led to better knowledge transfer, training, and integration of the network. This led to rapid dissemination and exploitation of new concepts and new skills.

Trainings

Workshops-Conferences

- SPM 2.0 Training Workshop 22nd – 25th January 2018, Linz Austria
- SPM 2.0 Winter School in Biophotonics and Bioelectronics, Hirschegg, Austria, 18-24 February 2018
- SPM 2.0 Training Workshop 26th– 29th June 2018, Modena ,Italy
- SPM 2.0 Training Workshop 28th– 31st January 2019, Linz, Austria
- "Cypher AFM Workshop", 7th February 2019, CNR Bologna
- 1st Workshop on Neuromorphic Organic Devices, Ferrara Italy 12th -14th June 2019 – **Poster presentation**
- SPM 2.0 Training Workshop 26th – 29th June 2019 Teddington, UK
- 16th International Conference on Nanosciences and Nanotechnologies" 2nd – 3rd July, Thessaloniki, Greece – **Poster presentation**

- SPM 2.0 Training Workshop 28th– 31st January 2020, Linz, Austria
- SPM 2.0 Workshop on Advanced Scanning Probe Microscopies (Online), 10-11 December 2020
- "8th Multifrequency AFM Conference", Madrid, Spain, 27th-30th October 2020 - **Poster presentation**

Seminars

- "Teaching students to think like scientists", Carl E. Wieman, Facultad de Ciencias UAM, 19 October 2018 , Madrid
- "Tracking a cell's mass in real time: a new indicator of cell physiology", David Martínez-Martín, Instituto di Ciencia de Materiales de Madrid (ICMM), 20 November 2018, Madrid
- "Charge delocalization and transport in doped and intrinsic conjugated polymers", Prof. Alberto Salleo, 11th June 2019, Modena.
- "NanoScientific Forum Europe NSFE 2019" 11th-13th September 2019, UniBO, Bologna, Italy
- From Stimuli Responsive and Shape Memory Materials to Algorithmic Materials that Mimic Behaviorists´ Classical Conditioning, May 22, 2020, 11:30 am, Prof. Olli Ikkala (Virtual Seminar)
- Supramolecular Broad-Spectrum Antivirals, May 29, 2020, 11:30 am, Prof. Francesco Stellacci (Virtual Seminar)
- Understanding Gene Transcription and Genome Organization using Electron Microscopy, June 5, 2020, 11:30 am, Prof., Alessandro Vannini (Virtual Seminar)

Courses UNIMORE (PhD Program)

- "Physics of the single electron in the transmission electron microscope", Prof. Giulio Pozzi (Alma Mater Unibo)

- “English for Research”, Adrian Wallwork
- “An Introduction to Quantum Science”, Prof. M. Paris (Univ. Milano), Dr. P. Bordone, Dr. F. Troiani (CNR-Nano)

Secondments

- *5 months, Instituto de Ciencia de Materiales de Madrid (CSIC)*